Measurement of differential cross-section of the tZq process with the ATLAS Detector

Nilima Akolkar
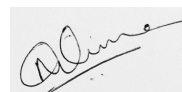
I hereby declare that this thesis was formulated by myself and that no sources or tools other than those cited were used.

Bonn, . . 17.11.2020 . . . .
          Date   Signature

1. Gutachter: Prof. Dr. Ian C. Brock
2. Gutachter: Priv. -Doz. Dr. Philip Bechtle

Contents

Introduction

> *Ask the right questions and nature will open the doors to her secrets.*
>
> C.V. Raman

Physics is about understanding nature the way it is. The question is: How close one has to look? The quest began from defining atom to be an indivisible entity of matter and eventually, our horizons of knowledge expanded. Many years of developing theories and building experiments to test these theories, led to the development of the Standard Model of Particle Physics. This remarkable theory confines our current understanding of the basic building blocks of matter.

Collider experiments are undertaken to explore different aspects of the SM. It probes particles at large energies. In this way, one can investigate various interactions occurring between them. Analysis of the data generated out of colliders, have led to major accomplishments in Particle Physics. A mystery of why W and Z bosons are massive while the other bosons are massless, was solved after the prediction of the Higgs boson. In the discovery of Higgs, the top-quark played an important role. The top-quark is the heaviest fundamental particle discovered so far. Owing to its large mass, it has a significant role in understanding the functioning of the SM. Moreover, it also provides hints to physics beyond the SM. The topic of this thesis is related to top-quark physics.

Out of the numerous interactions taking place at the LHC, one of the rare processes is the associated production of a single top-quark and a Z-boson. It is an interesting process to study, because it can probe coupling of a boson with a fermion and another boson at the same time. Initial studies were undertaken by the ATLAS collaboration [1] and the results were found to be consistent with the SM. A differential analysis has the potential to provide deeper insights about the process. New physics may affect kinematic properties of particles which can be reflected in the differential measurements.

This analysis explores the technique of unfolding. Data recorded by a detector is smeared due to its limited efficiency. Unfolding is a mathematical way to obtain original data without the detector effects. This allows for an accurate measurement to be performed, leading to reliable results.

This thesis is structured as follows: A theoretical overview of concepts used in Particle physics is given in Chapter 2. A detailed working of the ATLAS experiment is described in Chapter 3. Chapter 4 focuses on the tZq process. Specific signatures of the signal and background processes are discussed and in addition, the strategy to extract signal is also presented. The unfolding technique has been introduced in Chapter 5. The profile likelihood unfolding method, implemented in this thesis

is explained in detail. Validation tests and the unfolded differential cross-sections are presented in Chapter 6. At the end, a brief summary and future prospects are provided in Chapter 7.

Theoretical concepts

The first part of this chapter presents an overview of the theoretical and the experimental aspects of particle physics. Section 2.1 explains the widely successful Standard Model of Particle Physics while Section 2.3 deals with concepts of colliders used in modern particle physics experiments. The second part of this chapter focuses on the top-quark including its discovery, production, decay and other properties. The final part sheds light on rare processes involving the top-quark, such as associated production with weak bosons.

2.1 The Standard Model and its properties

Our current understanding of the fundamental structure of matter is confined in a theory called the Standard Model of Particle Physics (SM). This theory explains elementary particles of matter and interactions between them. The fundamental particles are broadly classified into fermions and bosons based on their spin configuration. Fermions are spin half particles and are divided into quarks and leptons depending on whether or not they are sensitive to strong interaction. Quarks are particles carrying fractional electric charge and they can only exist in bound states formed by two or three quarks called as hadrons e.g protons and neutrons. The negatively charged electron (e^-), muon (μ^-), tau (τ^-) and the corresponding electrically neutral neutrinos are called the leptons. According to the Standard Model neutrinos are massless. For each elementary particle there exists an anti-particle which has the same mass but opposite physical charge. Fermions can also be categorized into three generations each having an up-type quark, a down-type quark, a lepton and a neutrino. The first generation is composed of up-quark(u), down-quark(d), electron(e^-), and electron-neutrino(ν_e). These particles constitute most of the matter around us, for instance proton is made up of two up quarks and one down quark (uud). The second generation consists of charm-quark(c), strange-quark(s), muon(μ^-), and muon-neutrino (ν_μ) while the top-quark(t), botton-quark(b), tau(τ^-) and tau-neutrino(ν_τ) build up the third and the final generation. Masses of particles increase from first generation to the third, rest all properties remain same. An overview of the particles in the SM is shown in Figure 2.1.

The quarks and leptons interact with each other through spin-1 particles called the gauge bosons. Since these bosons carry force of interaction, they are called *force-carrier* particles. There are four fundamental forces existing in nature: gravitational, electromagnetic (EM), strong and weak. Except gravitation the other three are included in the SM. The Quantum Field Theory (QFT) supplies the underlying mathematical description for the EM, strong and weak processes. Fermions which

Standard Model of Elementary Particles
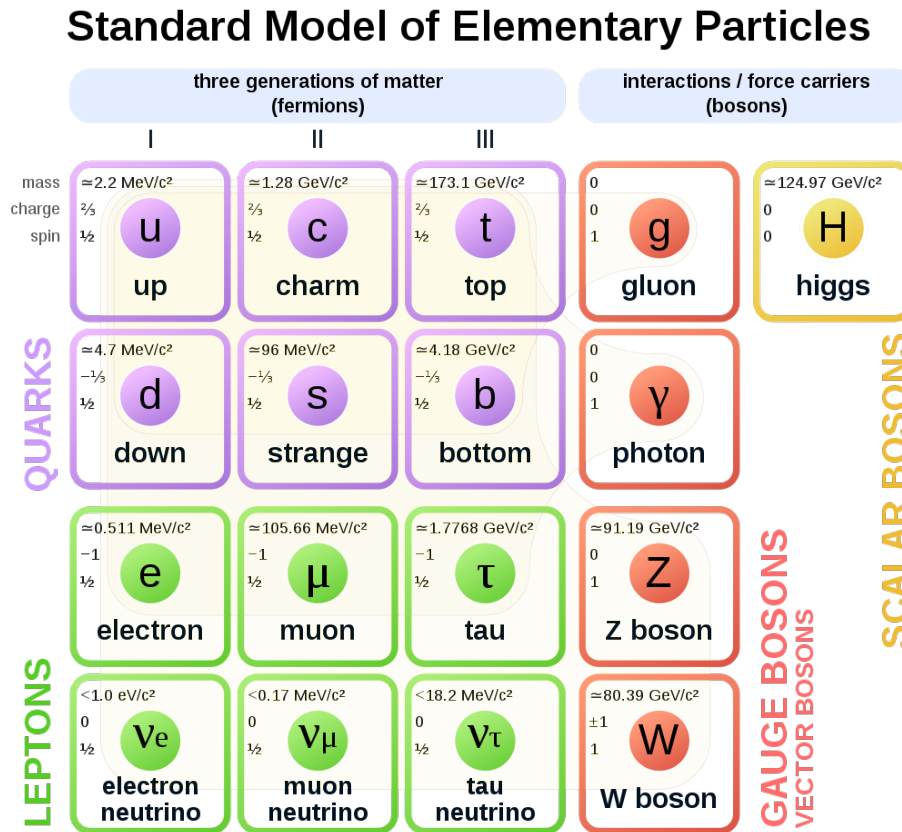
Figure 2.1: Overview of the particles in the Standard Model along with their properties including mass, spin and charge are shown. Particles shown in lavender and green are fermions while the ones shown in red are gauge bosons. Anti-particles are not shown[2].

possess a non-zero electric charge can participate in electromagnetic interaction mediated by the massless photon (γ). Photon, being electrically neutral, can not interact with other photons. Quantum Electrodynamics (QED) is the following QFT for EM interaction. It explains attraction and repulsion between charged particles. It is interesting to know how the proton, despite having two positive quarks, remains stable amidst the repulsion. This is because the strong force exists between the quarks and overcomes the repulsion.

The strong force is propagated by gluons and it is responsible for holding the quarks together inside a hadron. Particles are required to possess a *colour* charge to undergo strong interaction. Out of the SM particles, only quarks have the colour charge. There exist three different quark fields, namely green,blue and red. Moreover, there are eight gluon fields, each with a different combination of colours. Unlike photons, gluons can interact with other gluons since they carry colour charge themselves. The QFT explaining the strong interaction is called Quantum Chromodynamics (QCD). This theory forbids quarks from existing freely in nature and therefore quarks exist in colour-neutral bound states along with other quarks or anti-quarks. In QED, the antiparticles have opposite electric charges whereas in QCD the anti-particles are defined as particles having opposite colour charges.

QED and QCD are similar in most aspects. Both theories describe interactions mediated by massless spin-1 bosons. Theory explaining the third SM interaction, the weak interaction, differs from both these theories in many ways.

The weak force is mediated by massive gauge bosons including charged W^+, W^- and neutral Z boson. It manifests itself in phenomenon like nuclear decay and nuclear fusion. All fermions, even neutrinos, can interact weakly because they all possess the weak isospin that is charge of the weak interaction. It is the only interaction in the SM that permits change of flavour of final state particles and transition between different generations. Quarks can couple weakly and shift from one generation to another. For instance d-quark can change into c-quark by exchanging W^+ or W^-. This unique feature is exhibited because the mass eighenstates of quarks and their weak eighenstates (states that participate in an interaction) are not same. The weak states are a mixture of the three mass eighenstates. In principle, if a d-quark interacts with a W-boson, the W-boson will *see* the incoming flavour as a mixture of d, s and b quarks. This mixing or superposition is described in the SM by the CKM matrix. The Cabibbo-Kobayashi-Maskawa (CKM) matrix is a unitary 3×3 unitary matrix which connects the weak eighenstates to the mass eighenstates,

$$\begin{pmatrix} d' \\ s' \\ b' \end{pmatrix} = V_{\text{CKM}} \begin{pmatrix} d \\ s \\ b \end{pmatrix}. \tag{2.1}$$

The recent values in the CKM matrix are: [3]

$$V_{\text{CKM}} = \begin{pmatrix} V_{ud} & V_{us} & V_{ub} \\ V_{cd} & V_{cs} & V_{cb} \\ V_{td} & V_{ts} & V_{tb} \end{pmatrix} = \begin{pmatrix} 0.97401 \pm 0.00011 & 0.22650 \pm 0.00048 & 0.00361^{+0.00011}_{-0.00009} \\ 0.22636 \pm 0.00048 & 0.97320 \pm 0.00011 & 0.04053^{+0.00083}_{-0.00061} \\ 0.00854^{+0.00023}_{-0.00016} & 0.03978^{+0.00082}_{-0.00060} & 0.999172^{+0.000024}_{-0.000035} \end{pmatrix}. \tag{2.2}$$

Non-zero components of the CKM matrix play a role in the weak interaction between quarks. The interaction strength is proportional to square of the relevant component of the matrix, $|V_{ij}|^2$. The CKM matrix can also be described in terms of three rotation angles and a complex phase. It can be seen form the matrix that the off-diagonal components have relatively smaller values than the diagonal components, due to which the interactions between quarks of different generations are suppressed compared to those of the same generations. The weak theory divides the fermion fields into left-handed and right-handed fields. However only the left-handed fermions and right-handed anti-fermions carry the weak isospin.

A significant property of each theory in the SM is that it is invariant under the transformation by a specific Lie group. This unique group is called its symmetry group. The groups $SU(2)_L$, $U(1)_{EM}$ and $SU(3)_C$ are the symmetry groups for weak theory, QED and QCD, respectively. The subscript L depicts left-handed fermions and C stands for colour. The electromagnetic and weak interactions can be unified in a single theory called the electroweak theory. The unification gives a single unified symmetry group $SU(2)_L \times U(1)_Y$. Here, Y is the weak hypercharge operator and it is related to Q, which is the generator of $U(1)_{EM}$, and weak isospin T_3 by:

$$Y = 2(Q - T_3). \tag{2.3}$$

The internal symmetry of the Standard Model is given by:

$$SU(3)_C \times SU(2)_L \times U(1)_Y. \tag{2.4}$$

At low energies, the symmetry $SU(2)_L \times U(1)_Y$ is broken due to Higgs mechanism. It is referred to as spontaneous symmetry breaking and is responsible for the non-zero masses of the weak bosons. Fermions acquire mass through Yukawa interactions with this newly generated scalar field called the Higgs field. The mass of the fermion depends on the interaction strength. Photon doesn't interact with Higgs hence it is massless. The Yukawa coupling of the top quark is strongest among the other fermions and consequently it has the largest mass.

Out of the fundamental particles, this thesis focuses on the top quark and the Z boson.

2.2 Feynman diagrams

A pictorial representation of the interactions between fundamental particles can be shown by Feynman diagrams. It makes use of straight lines with arrows to show particles and anti-particles participating in the interaction and curly lines to show the boson exchanged between them. The Feynman diagrams are symbolic and have no physical meaning. As shown in Figure 2.2(a), two electrons represented by two external lines enter, a photon is mediated between them and then they exit. Here the time runs along the x-axis. This process is called Møller scattering. The intersection of the particle-lines and the boson-line in the diagram is called a vertex where the interaction takes place. It is important to keep in mind that neither the lines represent the trajectories of the particles nor the physical separation between them.

In Figure 2.2(b), one of the incoming particles is going backward in time, this is to show an anti-particle. The diagram represents an electron and positron annihilating into a photon and with time the photon turns into an electron-positron pair. This interaction is called the Bhabha scattering. Every Feynman diagram contains at least two vertices, diagrams with only one vertex violate the conservation of energy and hence are not allowed. Diagrams with more than two vertices are called higher-order diagrams.

The diagrams for a certain process can be analyzed for cross-section calculation using a set of rules called the Feynman rules. To analyze the process, contributions from all the possible diagrams are taken into account. For QED processes, each vertex in a diagram contributes a factor $\alpha = 1/137$ to the calculation. Since this factor is very small, diagrams with more vertices contribute less.

2.3 Concepts of collider physics

The proton-proton collisions produce a variety of processes that can be studied to understand the SM from an experimental point of view. If the two incoming protons stay intact after colliding, it implies an elastic collision has occurred. At high energies, the possibility of elastic collisions decrease. The incoming protons see each other as a bunch of partons instead of a single proton. The proton is composed of two u- and one d- quark called valence quarks. At high energies, these quarks can exchange gluons and in turn produce more gluons and quarks. In a way, the proton looks like a *sea* of gluons and quarks that altogether are called *partons*. Here the net flavour of a proton is the same as that of valence quarks. These partons interact and give rise to different SM processes.
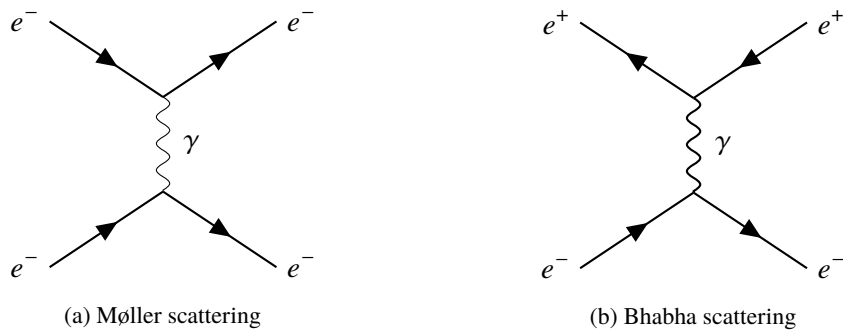
(a) Møller scattering   (b) Bhabha scattering

Figure 2.2: Feynman diagrams describing electron-electron scattering (left) and electron-positron scattering (right)

Cross-section

The probability of interaction to take place when two particles collide is measured in terms of the cross-section (σ). It is an effective area where the interaction occurred. The unit of cross-section is barn (b), where 1 b = 10^{-28} m^2. For a certain process, one can draw Feynman diagrams and calculate the corresponding cross-section using Feynman rules. Moreover, these values can be compared to the measured cross-section obtained from the data generated out of hadron colliders. When the measurement covers all the scattering angles, it is called total (or inclusive) cross-section. However, if the measurement is done as a function of a certain variable (X) of the final state particles such as momentum or energy, then it is called *differential*(or exclusive) cross-section ($d\sigma/dX$).

2.3.1 Inelastic scattering and Parton Distribution Functions (PDFs)

The binding forces between the constituents of accelerated protons act in the transverse direction. In the case of elastic collisions, these binding forces keep the protons intact after the collision even though the path is slightly deflected compared to the incoming direction. With the increase in the proton energy, the binding forces can no longer hold the proton together and as a result, the proton disintegrates into its partonic components long before the collision. Consequently, the rate of inelastic scattering increases and is measured as inelastic cross-section [4].

An important property of the strong force is that it depends on the energies of the interacting particles. The coupling constant for QCD α_s, which determines the strength of interaction, is not a constant. The value of α_s at low energies is very large, which is responsible for confinement of quarks inside a hadron. Large α_s implies a large contribution from higher-order diagrams unlike QED. In this case perturbation theory becomes unreliable. But experiments discovered that α_s becomes sufficiently small at high energies relevant to modern collider experiments. The reason behind this is the anti-screening of colour charges due to gluon self-interactions. The *running* of α_s allows theoretical predictions to be made using perturbation theory. This QCD feature is called *asymptotic freedom*.

In a proton, each quark of flavour i carries a specific fraction x of the total momentum of the proton. It is expressed in terms of Parton Distribution Function (PDF) $f_i(x_i, Q^2)$. Here, Q is the energy scale of the interaction. The determination of PDFs is necessary for cross-section predictions at hadron colliders [5]. The cross-section to produce a final state X in a proton-proton collision can be expressed

as

$$\sigma_{p_1 p_2 \to X} = \Sigma_{i,j=partons} \int dx_i dx_j \cdot f_1(x_i, \mu^2) f_2(x_j, \mu^2) \sigma_{ij \to X}(s, \mu^2). \tag{2.5}$$

Here i,j stand for the partons in two protons p_1 and p_2; f_1 and f_2 are PDFs of the protons; s is the center of mass energy squared and $\sigma_{ij \to X}$ is the cross-section for i and j to make final state X.

Center-of-mass energy

In a collision between two particles the total center-of-mass energy is expressed as

$$\sqrt{s} = \sqrt{(\Sigma_{i=1}^2 E_i)^2 - (\Sigma_{i=1}^2 p_i)^2}, \tag{2.6}$$

where E and p are energy and momentum of the two initial state particles. If two colliding beams of the same particle type have the same energy, then the center-of-mass energy is $\sqrt{s} = 2E_{beam}$, neglecting the masses of particles.

Luminosity

An important parameter of an accelerator is its luminosity $\mathcal{L}$ that determines the number of events of a particular process during collisions. In an accelerator, the instantaneous luminosity is measured by grouping the particles into bunches and colliding them at one or more interaction points, by using

$$\mathcal{L} = f \frac{n_1 n_2}{4\pi \sigma_x \sigma_y}, \tag{2.7}$$

where n_1, n_2 and f are the number of particles in the colliding bunches and the frequency of collision, respectively; σ_x and σ_y are root-mean-squared horizontal and vertical beam sizes, respectively.

For a process, the observed number of events is given by the product of the luminosity integrated over the lifetime of operation of the accelerator and the cross-section of the process,

$$N = \sigma \int \mathcal{L} dt. \tag{2.8}$$

Decay rate and branching ratio

An elementary particle often decays into smaller particles through the possible decay modes or channels, depending on the conservation laws for quantum numbers and strength of the decay process. The probability per unit time of a particle decaying is called its decay rate (Γ). For N identical particles the change in the number after time dt is given by

$$dN = -\Gamma N dt. \tag{2.9}$$

The lifetime of the particle is the time after which the sample becomes $\frac{1}{e}$ of its original size,

$$\tau = \frac{1}{\Gamma}. \tag{2.10}$$

When multiple decay modes are possible, the total decay rate of the particle is the sum of individual decay rates. In order to learn the dominance of a certain decay mode, we calculate its branching ratio (BR). The branching ratio of a decay mode i is defined as

$$BR = \frac{\Gamma_i}{\Gamma_{\text{total}}}. \tag{2.11}$$

2.3.2 Kinematics

Transverse momentum

The axis along which the colliding particles are boosted is referred to as the beam axis or longitudinal axis. The sum of momentum components along the transverse axis (perpendicular to the beam axis), is called transverse momentum,

$$p^T = \sqrt{p_x^2 + p_y^2}. \tag{2.12}$$

where beam is along the z-axis.

For a boost along the beam axis, there is no initial transverse momentum of particles and as per the conservation of momentum, the final transverse momentum should also be zero. This is used to detect invisible particles like neutrinos. Momenta of all the particles are reconstructed and subtracted from zero to get the momentum of invisible particles, this is called missing transverse momentum.

Rapidity

Out of the total boosted particles in collider experiments, only a fraction interacts and produce final state particles. One can determine the kinematics of the total boosted particles but the energy and momentum of the particles that actually interact are unknown. There is a need for a quantity that is invariant under boosts along the beam direction. Such quantity is the rapidity y defined as

$$y = \frac{1}{2} \ln \left(\frac{E + p_z}{E - p_z} \right). \tag{2.13}$$

Here E is the energy and p_z is the momentum component along the z-axis.

Pseudorapidity

In cases where $|\vec{p}| \simeq E$, the rapidity is not very reliable. Instead, a quantity called pseudorapidity (η) is convenient to use. It is dependent on the polar angle θ,

$$\eta = -\ln \tan \left(\frac{\theta}{2} \right). \tag{2.14}$$

For two particles let $\Delta\eta$ and $\Delta\phi$ be the differences of their pseudorapidies and azimuths, respectively. The angular separation between them can be defined as

$$\Delta R = \sqrt{(\Delta\eta)^2 + (\Delta\phi)^2}. \tag{2.15}$$

Pile-up

Pile-up is referred as the signal coming from collisions other than the collision of interest. There are two sources of pile-up, namely in-time and out-of-time. In-time pile up is due to collisions occurring in the same bunch-crossing and out-of-time pile-up is contributed by the collisions from previous or later bunches. The accurate detection of objects under study becomes difficult due to pile-up events. Modeling of these background events is a crucial part of an analysis [6].

2.4 Top-quark physics

2.4.1 Discovery

The electroweak theory states that the left-handed particles forming weak isospin doublets can interact weakly. In 1977 the bottom quark was discovered and it led to the prediction of its weak isospin partner, the top quark t. This prediction was made to keep the electroweak theory internally consistent. After puzzling the scientists for around two decades, the top quark was finally discovered in 1995 at the Fermilab Tevatron by the CDF and D0 experiments.

2.4.2 Top-quark properties

The top-quark is the up type quark belonging to the third generation of the SM. It is the heaviest known elementary particle with a mass of (172.76 ± 0.30) GeV [3]. The t-quark is extremely short lived for about 5×10^{-25} seconds which is much smaller compared to the time required to form hadronic states. Consequently, it decays before it can hadronise; due to this fact, the t-quark is often viewed as a quasi-free quark. Unlike other quarks the t-quark gives an opportunity to study properties of a *bare* quark. The large decay width of the top falls in the non-perturbative regime of QCD and hence the properties can be predicted using perturbation theory.

Since its discovery, top-quark has been an interesting topic of research owing to its large mass compared to other SM particles. It is of the same order as the scale where the electroweak symmetry breaking (EWSB) occurs. By precisely measuring the mass, one can get a deeper understanding of EWSB. The strong Yukawa coupling to Higgs field, which results in its large mass, was considered an important parameter in constraining the Higgs boson mass during its discovery [7]. It is crucial to precisely measure the top quark properties not only to test the consistency of the SM but also to test the possibility of new physics. Some models of new physics beyond the SM hypothesize new particles decaying into top-quarks.

Top-quark decays almost entirely into a W-boson and a b-quark. The decay process takes place weakly and it is a consequence of the large $|V_{tb}|$ value of the CKM matrix.

$$t \rightarrow Wb$$

2.4.3 Top-quark production

Top-quark pair production

Top-quark was discovered at the Tevatron but after its shutdown in 2011, the LHC became the only place where top-quarks are produced in abundance. LHC is therefore referred to as the *top-factory*.

Top-quarks are produced dominantly as top-anti-top pairs via the strong interaction. In proton-proton collisions, top-quark pairs ($t\bar{t}$) are produced either by gluon-gluon fusion or $q\bar{q}$ annihilation. The dominance of either productions depends on the PDFs, center-of-mass energy at which particles are probed and the type of colliding particles. Feynman diagrams for these processes at leading order (LO) in QCD are shown in the Figure 2.3. Theoretically, cross-section of the $t\bar{t}$ production is available at the next-to-next-to-leading order (NNLO) in QCD. Measurements have been performed at the LHC and they agree with the predictions. For instance, the ATLAS Measurement of $\sigma_{t\bar{t}}$ is [8]

$$\sigma_{t\bar{t}} = 830 \pm 0.4(\text{stat}) \pm 36(\text{syst.}) \pm 14(\text{lumi}) \text{ pb.} \tag{2.16}$$

The $t\bar{t}$ process is an important background in many searches for physics beyond the SM.
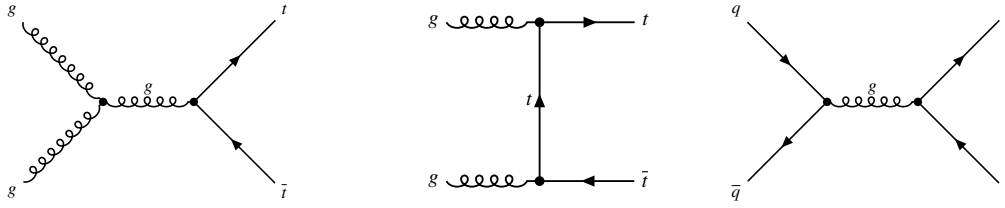

Figure 2.3: Feynman diagrams for $t\bar{t}$ processes at LO in QCD.

Single-top production

There are three separate processes at LO for producing single-top and single anti-top, which can be distinguished based on the virtuality of the exchanged W-boson. The dominant process is the t-channel process, as shown in Figure 2.4(a), where a light quark and a b-quark interact weakly and produce a top-quark along with a quark. The corresponding cross-section $\sigma(tq)$ is greater than $\sigma(\bar{t}q)$ because the density of u-quark is twice than d-quark in proton-proton collisions. The ATLAS collaboration measured $\sigma(tq)$ and $\sigma(\bar{t}q)$ at $\sqrt{s} = 13$ TeV: [9]

$$\sigma(tq) = 156 \pm 28 \text{ pb}, \sigma(\bar{t}q) = 91 \pm 19 \text{ pb.} \tag{2.17}$$

The second dominant production mode is the Wt-channel, as shown in Figure 2.4(b). In this process, an initial state b-quark interacts with a gluon and produces a top-quark and a W-boson. Approximately 24 % of the total single-top production cross-section is contributed by Wt-channel. The single-top production cross-section contributed by Wt-channel is measured by the ATLAS collaboration is: [10]

$$\sigma_{tW} = 94 \pm 10(\text{stat.})^{+28}_{-22}(\text{syst.}) \pm 2(\text{lumi.})\text{pb.} \tag{2.18}$$

The least probable process for single-top production is the s-channel process. Two initial state quarks couple weakly to produce single-top. The Feynman diagram for the s-channel process is shown in Figure 2.4(c) It was investigated by ATLAS collaboration at $\sqrt{s} = 8$ TeV and the measured cross-section is: [11]

$$\sigma_s = 4.8 \pm 0.8(\text{stat.})^{+1.6}_{-1.3}(\text{syst.})\text{pb.} \tag{2.19}$$

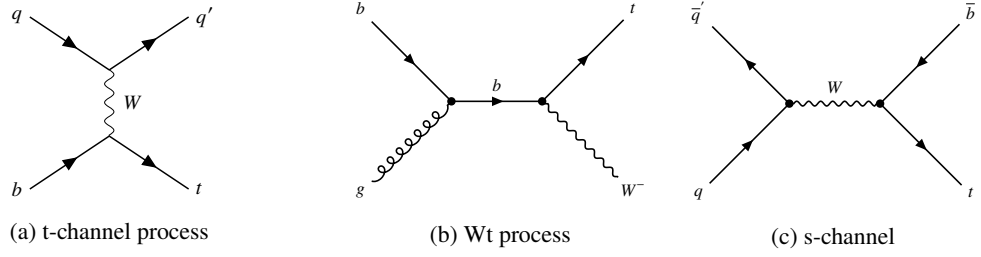(a) t-channel process   (b) Wt process   (c) s-channel

Figure 2.4: Feynman diagrams for single-top production processes at LO in QCD

All the three processes involve a Wtb vertex incorporating the electroweak couplings of the top-quark. Consequently they allow direct measurements of the absolute value of the CKM matrix element $|V_{tb}|$.

2.4.4 Rare processes involving top-quark

The theories beyond the SM predict large couplings of the top-quark with new particles. For obtaining experimental evidence, it is essential to study rare processes involving top-quarks. Top-quark pair production in association with gauge bosons(W,Z) are two of the rare processes. Their production cross section is around 1 pb. Examining these processes one can measure weak couplings of the top-quarks and test the SM. Deviations from the SM predicted value of coupling strength can lead towards new physics. The measured cross-sections for $t\bar{t}W$ and $t\bar{t}Z$ by the ATLAS collaboration are: [12]

$$\sigma_{t\bar{t}W} = 0.87 \pm 0.13(\text{stat}) \pm 0.14(\text{syst.}) \ \text{pb}$$
$$\sigma_{t\bar{t}Z} = 0.95 \pm 0.08(\text{stat}) \pm 0.10(\text{syst.}) \ \text{pb}.$$

The process involving top-quark pair production along with Higgs boson($t\bar{t}H$) probes direct measurement of top-Yukawa coupling y_t at the LHC. Since it is the largest fermion-Higgs coupling, it is important to obtain a precise measurement. Determination of the magnitude of y_t is possible by studying $t\bar{t}H$ process. Another process where single-top is produced with Higgs (tH) can be measured simultaneously with $t\bar{t}H$ and it is sensitive to the sign of y_t. The production cross-sections of both the processes are very small and consistent with SM prediction [13],

$$\sigma_{t\bar{t}H} = 294^{+182}_{-162} \ \text{fb}. \tag{2.20}$$

Evidence for an extremely rare process involving production of four top-quarks ($t\bar{t}t\bar{t}$) has recently been reported at the LHC. The production cross-section of four-tops is measured to be 24^{+7}_{-6} fb [14]. Its significance corresponds to 4.3 standard deviations with an expected significance of 2.4 standard deviations. The $t\bar{t}t\bar{t}$ cross-section is sensitive to the magnitude and CP properties of y_t.

2.4.5 Single-top production with a Z-boson

Rare electroweak processes such as associated production of a single top-quark and a Z-boson can be investigated owing to the high energy and large luminosity at the LHC. Looking at the Feynman

diagrams at LO (Figure 2.6) one can notice that it resembles the *t*-channel production of a single top-quark with an addition of a *Z*-boson radiated from one of the incoming or outgoing quarks, or from the exchanged *W*-boson. The $pp \rightarrow tZ$ process, referred to as the *tZq* process, probes the *WWZ* coupling and *tZ* coupling. It is a unique feature for a single process to probe boson-boson and fermion-boson coupling simultaneously. A study of the *tZq* process can be a precursor to *tHq* which is a process probing similar couplings as the *tZq* process.

Evidence for the *tZq* process was reported by the ATLAS collaboration [15] with a meausred significance of 4.2 standard deviations. Later the production cross-section was measured by ATLAS and CMS experiments. The SM predicted cross-section at NLO in QCD under the condition of the dilepton mass being greater than 30 GeV, is 102^{+5}_{-2} fb. Data obtained from the ATLAS detector at $\sqrt{s}$ = 13 TeV with luminosity corresponding to $139\,\text{fb}^{-1}$ was analyzed in the trilepton channel, where the *Z*-boson decays into two leptons and the *W*-boson from the *t*-quark also decays leptonically. The result of this analysis is: [1]

$$\sigma_{ATLAS}(pp \rightarrow tZq \rightarrow tl^+l^-q) = 97 \pm 13\text{(stat.)} \pm 7\text{(syst.)} \ \text{fb.} \tag{2.21}$$

The CMS measurement for production cross-section with the same final states corresponding to an integrated luminosity of $77.4\,\text{fb}^{-1}$ is: [16]

$$\sigma_{CMS}(pp \rightarrow tZq \rightarrow tl^+l^-q) = 111 \pm 13\text{(stat.)}^{+11}_{-9}\text{(syst.)} \ \text{fb.} \tag{2.22}$$

The production cross-section merely gives an overview of the process. We can get a better understanding of the process through differential cross-section analysis. An overview of production cross-sections for processes involving top-quark is given in Figure 2.5. It combines the measurements carried out by the ATLAS collaboration at different center-of-mass energies. It can be seen that the *tZj* process, referred to as *tZq* in this thesis, has very small cross-section compared to other processes.
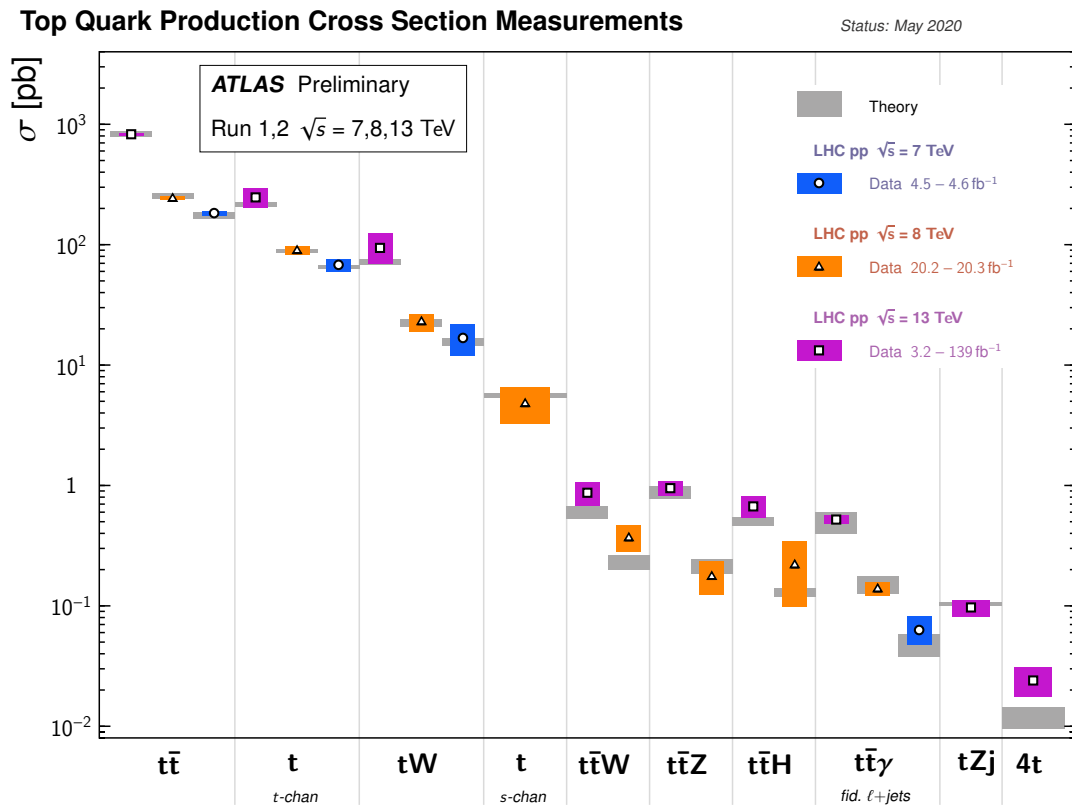
Figure 2.5: Summary of cross-sections for top-quark related processes measured with Run-1 and Run-2 data by the ATLAS collaboration. The theoretical predictions at NLO or higher are also given. Figure is taken from [17]
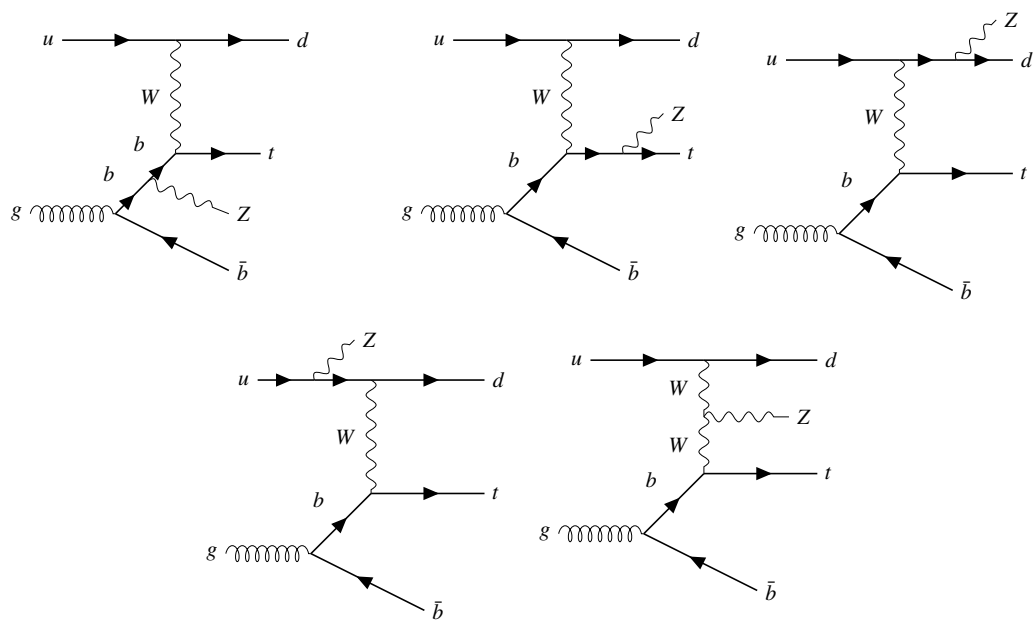
Figure 2.6: Feynman diagrams at LO for the tZq-process. The Z-boson is radiated either from incoming or outgoing quarks or from the exchanged W boson.

Particle detection and reconstruction

This chapter starts with a brief overview of the Large Hadron Collider followed by a detailed explanation of the ATLAS detector in Section 3.2. Section 3.3 discusses how different physics objects are observed in the detector and how they are reconstructed.

3.1 The Large Hadron Collider

The Large Hadron Collider (LHC) is the world's largest particle accelerator situated in CERN near the France-Geneva border, Switzerland. It is a cicular proton-proton collider which can reach 13 TeV center-of-mass energy.

3.1.1 The accelerating modules

The collider is a series of particle accelerators that bring protons to high energies in tiers. Initially, protons are extracted from hydrogen atoms by applying an electric field and injected into LINAC 2, the first accelerator in the series. It accelerates protons to an energy of 50 MeV and feds them to the Proton Synchrotron Booster (PBS), where they achieve an energy of 1.4 GeV. Afterwards the protons enter Proton Synchrotron (PS). It boosts the protons to 25 GeV and injects them into the Super Proton Synchrotron (SPS), which increases the proton energy to 450 GeV. Finally, the protons are inserted into two opposing beams of the LHC, the final machine of the accelerator series. Here, each beam attains a path-breaking energy of 6.5 TeV. The two beams continuously travel in opposite directions until they are brought in collision at the four interaction points where detectors are placed. The total energy at each collision point is 13 TeV [18]. An elaborate sketch of the accelerator complex is shown in Figure 3.1.

3.1.2 The LHC ring

The LHC is a 26.7 km long ring that contains superconducting magnets surrounding the beam pipes. It is installed in a tunnel situated 100 m underground at CERN [20]. There are 1 232 dipole magnets used to control the direction of the beam and 392 quadrupole magnets which focus the beam. In addition, there are insertion magnets which are located near the collision points. Their task is to squeeze the beams so that the chance of collisions increases [18].
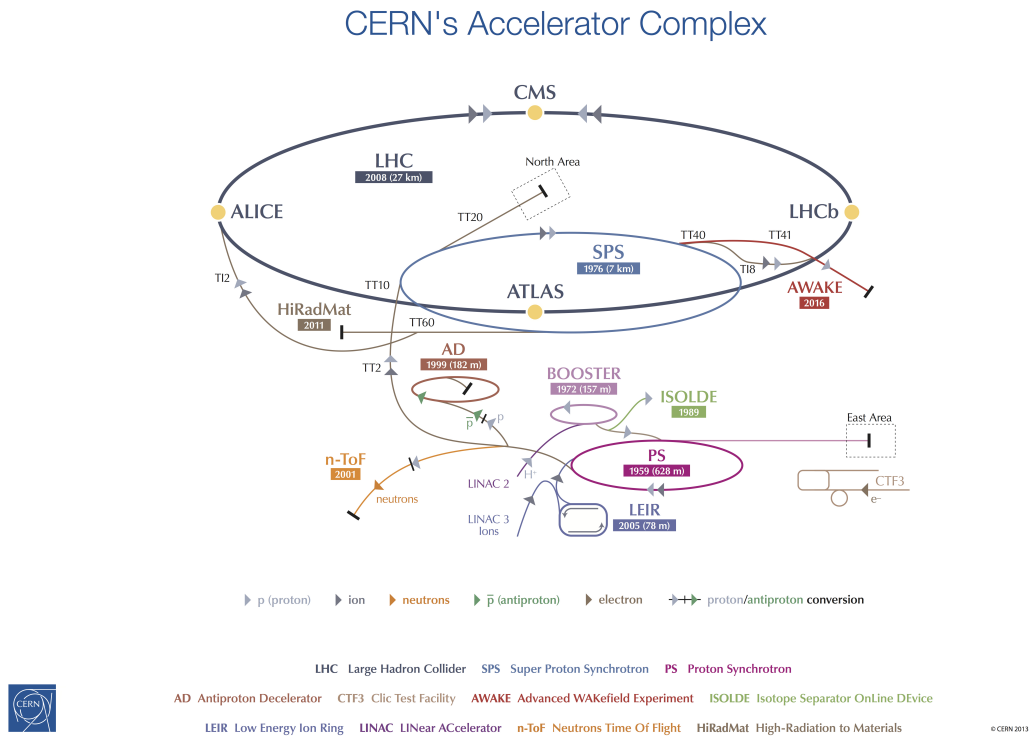
Figure 3.1: Schematic of the LHC along with all the machines in the accelerator series[19].

The LHC has the capability to collide 2 808 bunches per beam separated by 25 ns; each bunch contains approximately 10^{11} protons. During the period from 2015 to 2018, termed as Run-2 of the LHC, the instantaneous luminosity (explained in Section 2.3.1) of 10^{34} cm^{-2} s^{-1} was achieved [21].

3.1.3 Experiments at the LHC

There are detectors positioned at the four collision points of the LHC ring designed to observe the scattered particles after collisions. The LHC not only collides protons but also heavy nuclei such as lead ions at several energies. **A L**arge **I**on **C**ollider **E**xperiment (ALICE) undertakes the study of quark-gluon plasma generated from these lead ion collisions. Quark-gluon plasma is a phase of matter thought to have formed just after the big bang. It plays an important role to understand key aspects of QCD. The **L**arge **H**adron **C**ollider **b**eauty (LHCb) is a series of sub-detectors specialized to study beauty-quarks or *b*-quarks. Everything around us is made up of matter (containing particles) and not antimatter (containing anti-particles). The main aim of LHCb is to study this matter-antimatter asymmetry. The last two detectors, **A T**oroidal **LHC A**pparatu**S** (ATLAS) and the **C**ompact **M**uon **S**olenoid (CMS) are general-purpose detectors built to explore diverse range of physics interactions provided by the LHC. They possess various sub-components to accurately identify different particles and measure their properties. A detailed description of the ATLAS detector is given in the following section.

3.2 The ATLAS experiment

The ATLAS experiment [22] is one of the major experiments at the LHC that investigates Standard Model physics and also provides a window for beyond the SM particle searches. The ATLAS detector as shown in Figure 3.2, is the largest particle detector ever constructed. It weighs 7 000 tonnes and has dimensions of 46 m length and 25 m diameter. The detector consists of six different detecting systems arranged concentrically around the interaction point. Their function is to record energies, momenta and trajectories of particles that can be altogether used to identify individual particles.

Prime components of ATLAS are: the Inner Detector, the Calorimeter, the Muon Spectrometer and the Magnet System. In addition to the detector components, there are Trigger and Data Acquisition System (TDAQ) and the Computing System. The TDAQ selects events important from a physics point of view and ignores the rest. The Computing System analyzes the humongous amount of data from the detector through various software.

Coordinate system

A right-handed coordinate system is defined for ATLAS analyses. The interaction point (IP) is marked as the origin and the beam direction defines the *z*-axis. In the plane transverse to the beam direction, the line joining the IP with the center of the LHC-ring is the *x*-axis while y-axis runs in the upward direction. The angle around the beam axis is considered the azimuthal angle (ϕ) whereas the angle measured from the beam axis is the polar angle (θ).
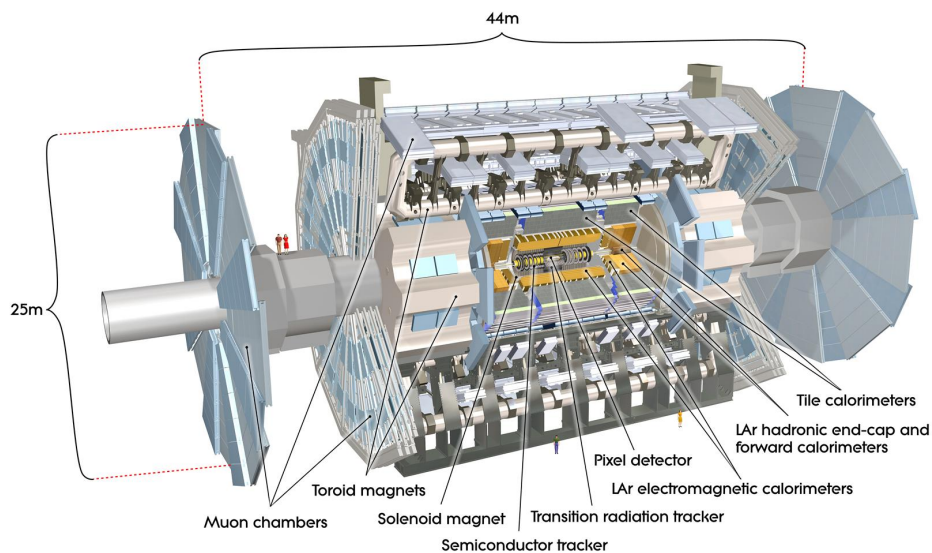

Figure 3.2: Schematic of the ATLAS detector. It includes all its components arranged in an onion-like structure [23].

3.2.1 The Inner Detector

The Inner Detector (ID) is the first component to encounter the decay products of collisions. It is enclosed in a cylindrical envelope immersed in a 2 T magnetic field generated by a solenoid magnets. The ID comprises of the pixel detector and the Semiconductor Tracker (SCT) in its innermost region while the Transition Radiation Tracker (TRT) resides in its outer region. These highly sensitive sub-components are designed to resolve charged particle tracks.

The sub-components register a *hit* whenever a charged particle induces a charge due to ionisation. Consequent *hits* characterise the trajectory of a charged particle. The ID functions within the range of $|\eta| < 2.5$. A schematic of ATLAS-ID is given in Figure 3.3.
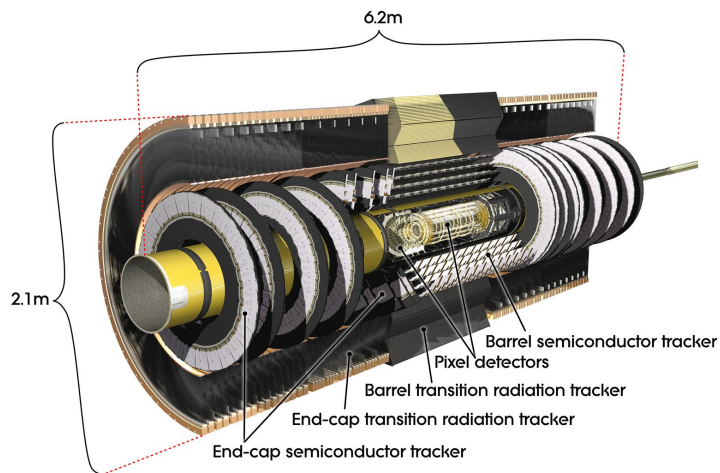

Figure 3.3: Schematic of the ATLAS Inner Detector. The sub-components are labelled[24].

The Pixel Detector

The pixel detector consists of four concentric layers of silicon pixel sensors around the beam axis in the barrel region and three layers placed on disks perpendicular to the beam axis in the end cap region. Each silicon pixel sensor measures $50 \times 400 \ \mu m^2$. Each layer contains rectangular modules with each module having 46 080 pixels. There are 1 744 modules in total [25]. Hits registered by the pixels are readout and are used to reconstruct the trajectory of particle.

Semiconductor Tracker

The SCT is a silicon microstrip detector wrapped around the pixel detector. There are 4 088 modules of silicon strip detectors with each module containing four silicon sensors; arranged in 4 barrel layers and 18 planer end cap disks. The SCT is made up of 6 million readout strips, distributed with a $80 \ \mu$ m spacing. This arrangement allows particle positions to be recorded with an accuracy of $17 \ \mu$ m in the direction transverse to the strip.

Transition Radiation Tracker

The TRT is a gaseous detector and it contains drift tubes or straws of 4 mm diameter each, filled with a mixture of xenon (70%), CO_2 (27%) and O_2 (3%). At the center of each straw there is a thin wire of 31 μ m diameter, kept at ground potential. The wall of the straw is kept at a potential of -1.5 kV. When a charged particle passes through the straw, ionisation occurs and free electrons drift towards the wire creating a current that can be detected [26]. The TRT has 350 000 read out channels that enables to measure the distance between particle track and wire with a precision of 0.17 mm [25].

The TRT not only provides tracking information but also plays a role in particle identification. Spaces between the straws are filled with polymer fibres to create transition radiation. The electromagnetic radiation emitted by a charged particle when it passes through a boundary between two inhomogenous media is called transition radiation. This property is utilized by the TRT to differentiate between different charged particles. Electrons emit the strongest transition radiation which distinguishes them from hadrons.

3.2.2 Calorimeters

The function of calorimeters is to measure the energy lost by a neutral or charged particle while traversing the detector medium. Specific high-density materials such as lead are used inside the calorimeters that have the capability to slow down a particle until it entirely stops inside the material. An incoming particle interacts with the calorimeter medium and creates a series of particles called a *shower*. The ATLAS calorimetry system is divided into the electromagnetic calorimeter (ECAL) and the hadronic calorimeter (HCAL) based on different types of particle-matter interactions.

Electromagnetic calorimeter

Incoming particles such as electrons and photons, interact electromagnetically with the ECAL medium. Pair production and bremsstrahlung[1] result into an electromagnetic shower of particles. The thickness and density of the ECAL absorbers is decided according to the radiation length of the material. Radiation length (X_0) is a property of material defined as the length at which energy of an incident particle becomes $1/e$ of its initial value.

The ECAL is divided into three parts: a barrel part with $|\eta| < 1.475$ coverage and two end caps within $1.375 < |\eta| < 3.2$. The lead absorbers, placed inside liquid argon, are arranged in an accordion geometry which provides a full azimuthal coverage. Moreover, the inner layers closer to the center of the detector have fine granularity to achieve high resolution while the outer layers have coarse granularity to detect any leakage.

Hadronic calorimeter

The tile calorimeter, liquid-argon hadronic end-cap calorimeter (HEC), and the forward calorimeter (FCal) consititute the structure of hadronic calorimeter. The tile calorimeter uses steel as an absorbing material and scintillators as active media. It surrounds the ECAL and covers a range of $|\eta| < 1.7$. The HEC is a liquid-argon and copper sampling calorimeter designed to cover a region within $1.5 < |\eta| < 4.9$ and the FCal is placed at $\eta > 4.9$. The FCal, being farthest from the detector center, encounters

---

[1] The radiation from a charged particle in presence of an electromagnetic field is called *bremsstrahlung*

high particle flux. In order to avoid any leakage, gaps between the absorbers are smaller compared to ECAL.

Incoming hadrons lose or gain electrons through ionisation or interact strongly with the detector medium and lose energy, creating hadronic showers inside the HCAL. These showers are larger than EM showers and therefore the volume of the HCAL is required to be larger to confine hadronic showers.

3.2.3 The muon spectrometer

The outermost part of the ATLAS detector is the muon spectrometer (MS). It is constructed to capture particles which penetrate the calorimeters effectively, specifically muons. It consists of precision tracking chambers and a trigger system. The Monitored Drift Tubes (MDT's) and the Cathode Strip Chambers (CSCs) track the muon path in the region within $|\eta| < 2.7$. These precision tracking chambers are arranged in three concentric shells around the beam axis in the barrel region while in the end caps, they form giant wheels perpendicular to the z-axis.

An important component of the muon spectrometer is the trigger that is designed to provide fast response of the track information. In the barrel regions, Resistive Plate Chambers (RPC) and in the end caps, Thin Gap Chambers (TGC) are built for triggering muon tracks. Measurements from the MDTs along with the trigger system response are used for measuring momenta.

3.2.4 Magnet system

The ATLAS detector is exposed to large flux of decay products during its operation. A strong magnetic field is required to bend the paths of charged particles for momentum measurements. For this purpose, a highly efficient magnet system including a central solenoid, barrel toroidal and two end cap toroidal magnets. The central solenoid magnet, operating with a current of 7.6 kA, is wrapped around the beam axis and provides a 2 T magnetic field to the Inner Detector. The barrel and end cap toroidal magnets operate at 20.5 kA and provide a magnetic field ranging from 0.5 to 1 T in the muon chambers. The barrel toroidal magnet is built from eight coils and kept equi-spaced to form a toroid-shaped magnet. The end cap magnets are placed inside the barrel toroidal magnet at both ends of the central solenoid magnet.

3.2.5 Trigger and Data Acquisition System

The trigger system is responsible for the selection of specific events out of the abundant amount of data received by the detector. It is a multilevel system designed to filter events which are important from a physics point of view. The Level-1 (L1) is a hardware based trigger which selects only a certain subset of events from the calorimeter and the muon spectrometer. The L1 trigger selects events which pass a specific threshold of transverse momentum and missing transverse energy; reducing the event count. It makes this decision every $2.5\,\mu$ s. The resulting subset of events is fed to the High-Level Trigger (HLT) which further refines the selection. The HLT is a software based trigger constructed using an army of CPUs. For improving the trigger selection, it utilizes information from the Inner Detector and selects only a fraction of events.

ATLAS uses a complex and efficient Data Acquisition System (DAQ) which internally connects the trigger systems. It transports data events from the L1 to the HLT. The DAQ brings together modern

technology to transfer the filtered events to permanent storage for offline analysis with an output rate of 1.5 GB/s. The ATLAS DAQ was developed during Run-1 of the LHC (2009-2013) and it was upgraded during Run-2 in order to cope with the increased number of collisions [27].

3.3 Reconstruction of Physics objects

Particles produced in collisions enter the detector and interact with the detector medium in different ways as shown in Figure 3.4. Specific signature left by them can be used to identify the particle with the help of reconstruction algorithms.
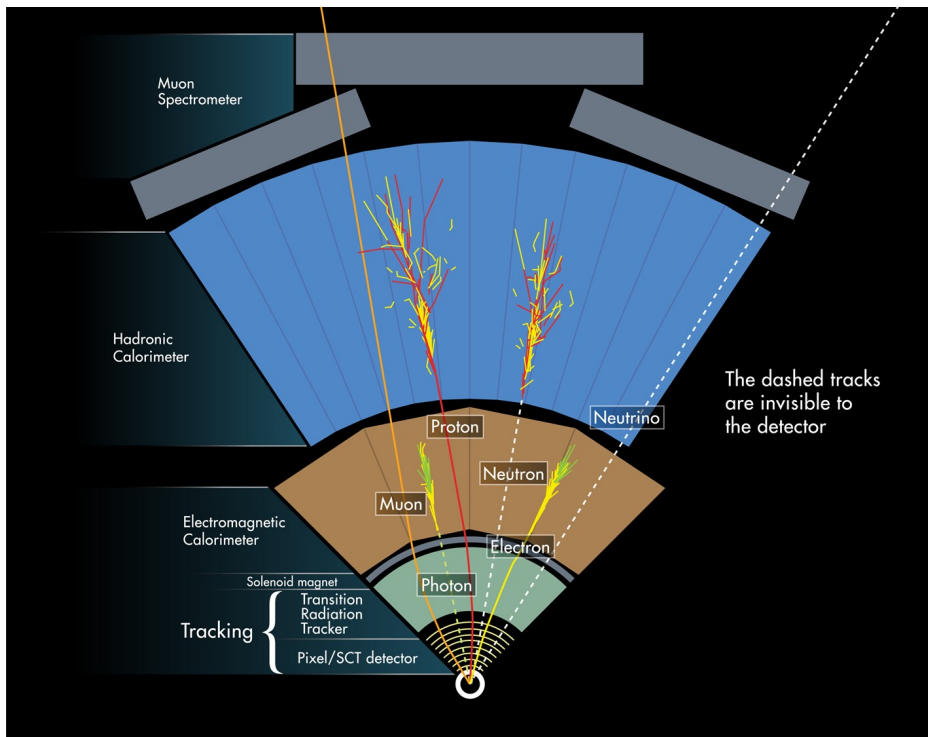

Figure 3.4: Schematic showing how different types of particles react inside the ATLAS detector. The sub detectors and particles they detect, are labelled [28].

Tracking and vertexing

A sequence of algorithms are designed to reconstruct particle tracks from signatures in the Inner Detector. The inside-out algorithm [29] constructs track seeds from sets of three space points in the pixel and SCT detectors. Hits from the ID are added to these seeds by the combinatorial filter. The ambiguities between track candidates are resolved by scoring them and considering the highest scored track [30]. The inside-out algorithm reconstructs tracks with p_T > 400 MeV. It is capable of reconstructing particles that are directly obtained from pp collisions, called primary particles. Similar tracking is done in the TRT. The reconstructed tracks in the TRT are back-tracked to match with the

SCT hits. Such back-tracking is useful to reconstruct secondary particles; the particles obtained from interactions between or decays from primary particles.

The task of finding vertices of interactions is done by vertex finding algorithms. It implements an iterative χ^2 fit of the vertex seed and neighbouring tracks. To each track, it assigns a weight proportional to its compatibility with the fitted vertex. Tracks found at distance greater than 7σ are utilized to construct new vertex seeds. This procedure is followed until no more vertices are found.

Clustering

Clustering algorithms are developed to collect the energy deposited into calorimeter cells by particles traversing the calorimeter medium. These algorithms record the signal from the cells and sum the total deposited energy within each cluster. In principle, there are two active clustering algorithms: sliding-window algorithm and topological algorithm.

The sliding-window algorithm groups the calorimeter cells that fall inside a fixed-size rectangular window. In this way, it fixes the size of the cluster. This algorithm can efficiently gather energy deposits by electrons and photons. The topological algorithm begins recording signal from one seed cell and moves towards neighbouring cells. The cells which contain energy greater than a threshold are recorded. This method is useful to identify jets and missing transverse energy.

3.3.1 Electrons

The reconstruction of electrons is done within the region $|\eta| < 2.47$ [31] using cluster information from ECAL and tracks from the Inner Detector. The sliding-window clustering algorithm records the energy deposits and they are matched with the track candidates from the Inner Detector. Once the energy is recorded, it is then calibrated to correspond to the original energy of the electron. There might be electrons originating from photon conversions. In order to ensure these electrons are not mistaken as electrons from collisions, an additional criteria is imposed according to which electrons are not accounted for if they are associated with a photon vertex. The final step is the identification of electrons out of the possible candidates which is done by a likelihood method. The reconstruction efficiency is greater than 99 % for E_T > 15 GeV. One can differentiate photons from electrons by the absence of a matching track in the ID

3.3.2 Muons

Muons are expected to leave signatures in the Inner Detector and the Muon Spectrometer. Reconstruction of muon tracks in MS is performed by using a fitting procedure. Hits in the muon chambers are connected to form segments, these segments from different layers are then fitted using a global χ^2 fit [32]. Based on the fit results, a muon candidate is selected. Muon tracks are reconstructed in the ID using similar procedure as electrons. Finally, the combined ID-MS reconstruction is performed to obtain the final tracks of muons. Depending on the sub-detector used for reconstruction, the muons are categorized into four different types: Combined muons are reconstructed using information from the ID and the MS, for segment-tagged muons tracks from the ID are extrapolated in the MS, calorimeter-tagged muons are obtained by extrapolating the ID tracks into calorimeter while the stand-alone muons are reconstructed inside the MS only.

3.3.3 Jets

Quarks and gluons produced in the p-p collisions can not exist in a free state and hence they form hadrons. The stream of collimated particles deposit energy in the calorimeters, mostly in the HCAL. These energy deposits are reconstructed as *jets*. For the reconstruction of jets, the clusters collected from the topological clustering algorithm are fed as input to the jet reconstruction algorithm. The anti-k_t algorithm is used in ATLAS analyses which reconstructs jets using radius parameter (R). The radius parameter indicates the geometrical scale of a jet. A specific value of R is selected and clusters confined into that angular distance are termed as jets. The jets associated with gluons and quarks are called small-R jets because they are reconstructed with $R = 0.4$ while the large-R jets, $R = 1.0$, are associated with the hadronic decay of massive particles.

The distance, d_{ij}, between two physical objects i and j is defined as follows: [33]

$$d_{ij} = \min\left(\frac{1}{p_{T,i}^2}, \frac{1}{p_{T,j}^2}\right)\frac{\Delta R_y^2}{R^2}$$

where $\Delta R_y^2 = (y_i - y_j)^2 + (\phi_i - \phi_j)^2$. This analysis takes into account only small-R jets. The anti-k_t algorithm looks for the smallest distances between two objects and merges them into one object. This procedure continues until no objects are left or distance between two objects become greater than their distances from the beam. All the merged objects are then grouped as a jet. Large-R jets are usually corrected by removing undesired pile-up effects with grooming algorithms. It follows a well-defined strategy to rebuild a new jet from selected relevant components of the old jet. A discriminant known as jet-vertex-tagger(JVT) is developed to identify jets originating from the interaction of interest. By placing appropriate cuts on the discriminant, pile-up effects can be reduced.

b-jets

Jets emerging from b-quarks have characteristic features that can be exploited to identify the jet. The b-jets used in this analysis are tagged using the long lifetime, large mass and decay multiplicity of b-hadrons that make up the b-jet. This procedure is called b-tagging. A b-hadron can travel significant distances from the primary vertex from where it originated, before decaying leptonically or into light flavour quarks. The secondary vertex finding algorithm searches for a secondary vertex and measures its properties for instance, number of originated tracks. Detailed information on b-tagging algorithms can be found in [34]. The top-quark almost always decays into a b-quark and a W-boson and therefore it is important to efficiently tag b-jets to accurately detect top quarks. The efficiency of b-tagging algorithms is given by *working points*.

3.3.4 Missing transverse momentum

Missing transverse momentum is computed to identify undetectable particles like neutrinos. These particles penetrate the detector without leaving any signatures. The reason to compute this quantity is given in Section 2.3.2. Missing transverse momentum is the negative vector sum of all transverse momenta of detectable particles.

Event selection and signal extraction

This chapter contains an overview of the tZq process in the trilepton final state. Other processes of importance are discussed in Section 4.2. Data and MC samples used in this analysis are presented in Section 4.3. Different sources of systematic uncertainties are also discussed. Event selection and methods required for extracting signal events are explained in the final part of the chapter.

4.1 The tZq trilepton final state

Presented in this thesis is a measurement of the differential cross-section of a single top-quark production in association with a Z-boson produced in the trilepton final state. Both these particles are short-lived and decay after a short duration. Here, the top-quark and the Z-boson are reconstructed from their decay products. As already discussed in Section 2.4.2, the t-quark always decays into a W-boson and a b-quark. The W-boson can decay either into a charged lepton and a corresponding neutrino or into hadrons. On the other hand, the Z-boson can decay into neutrinos, a quark-antiquark pair or a pair of opposite sign (charge) same flavour (OSSF) leptons. For the final state involving leptons, all flavours (electrons, muons and taus) are equally probable. Possible decay modes of the top-quark and the Z-boson with the corresponding branching ratios are shown in Figure 4.1.

In order for tZq production to have a trilepton signal, the Z-boson must decay into OSSF leptons and the W-boson from the top-quark decay must decay into a lepton and its corresponding neutrino. Taus are only considered if they decay into electrons or muons. Possible combinations of the final state leptons are eee, $\mu\mu\mu$, $e\mu\mu$ and μee. The branching ratio of the trilepton final state is 2 %. A strict requirement of having three leptons in the final state gives a clean signal of the process. The trilepton channel has yielded the best signal to background ratio compared to other channels. A Feynman diagram in Figure 4.2 shows one of various tZq processes and its trilepton final state. It consists of three charged leptons (electrons or muons), two jets (one of which is a b-jet from the t-quark) and a neutrino. The jet associated with the depicted $\bar{b}$-quark in Figure 4.2 is undetected because it travels along beam direction. For reconstruction of the Z-boson, it is required for two out of the three leptons to have invariant mass close to the Z-boson mass. Jets can be reconstructed using anti-k_t algorithm and b-jet can be identified using b-tagging. Computation of missing transverse momentum leads to the reconstruction of the neutrino.

Figure 4.1: The decay modes of the top-quark in association with a Z-boson along with their respective branching ratios are shown. The blue box indicates the branching ratio of the top-quark and the Z-boson decaying leptonically [35].
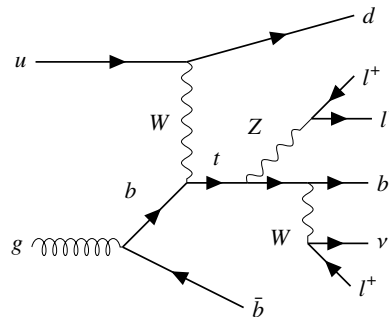

Figure 4.2: Feynman diagram at LO showing the tZq process in the trilepton final state.

4.2 Backgrounds

There are some processes that show similar characteristics to that of our signal. These processes are called backgrounds. As described in the previous section, the signal is defined to have three real (or prompt) leptons originating from taus or massive bosons(W,Z). Some background processes involve three real leptons in their final states while other background processes decay into a dileptonic final state but they get an additional fake or non-prompt lepton contribution. A fake lepton can come from a jet misidentified as electron while non-prompt lepton has various sources: kaon or pion decay, photon conversion, decay of bottom or charm quarks. The background contribution is estimated from simulated MC samples.

Background processes involving fake or non-prompt leptons

Pair production of top-quarks, known as $t\bar{t}$ production, contributes largely to background events. A Feynman diagram of $t\bar{t}$ production is shown in Figure 4.3(a). If one of the b-quarks decay leptonically

then a non-prompt lepton produced. Thus, qualifying the event for our imposed selection. Moreover, the production of the Z-boson along with jets as shown in Figure 4.3(b), also involves a fake or a non-prompt lepton. If the jets are light, they can be misidentified as lepton and in case of heavy flavour jets, leptonic decays can lead to a non-prompt lepton. With an additional untagged jet contribution, these processes satisfy the signal requirements.
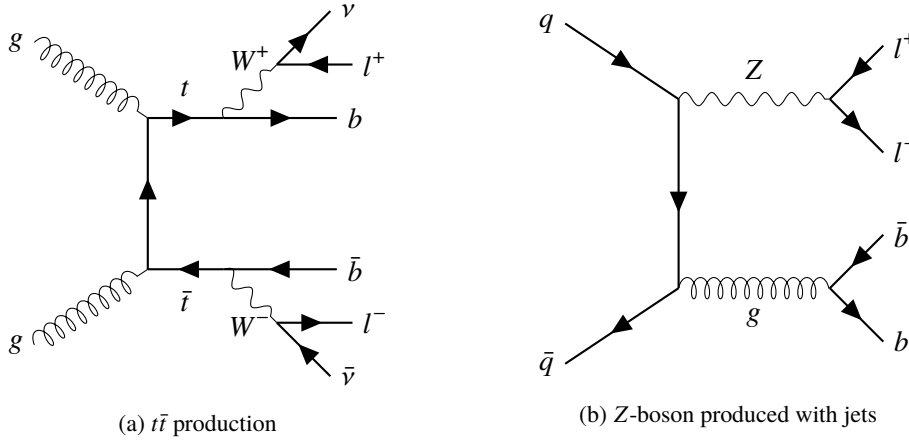

(a) $t\bar{t}$ production   (b) Z-boson produced with jets

Figure 4.3: LO Feynman diagrams of background processes involving non-prompt leptons

Background processes involving prompt leptons

These background processes involve three real leptons in the final state.

Diboson

Production of two massive bosons (WW,WZ or ZZ) is considered as a main background of the tZq production. The WZ process is a major contribution when both bosons decay into leptons and additional jets are produced. In contrast, the ZZ process does not contribute as much. For the ZZ process, one of the leptons from either Z fails the required condition to get selected as a real lepton or is not reconstructed. Consequently, its final state involves only three leptons and with additional jets it would pass our tZq selection. Feynman diagrams for diboson processes are shown in Figure 4.4 and Figure 4.5.

$t\bar{t}V$ and $t\bar{t}H$

Top-quark pair production in association with a massive boson $t\bar{t}V$, $V = Z$, W or H, are important background processes in the tZq production. Contribution from the $t\bar{t}H$ is small because cross-section of the Higgs decaying into leptons is small. On the other hand, the $t\bar{t}Z$ process has a significant contribution to backgrounds because it already has a Z-boson and a top-quark which are a part of the signal. If one of the b-jets is not tagged, then the resulting final state is similar to the signal process. A Feynman diagram displaying $t\bar{t}Z$ is shown in Figure 4.6.
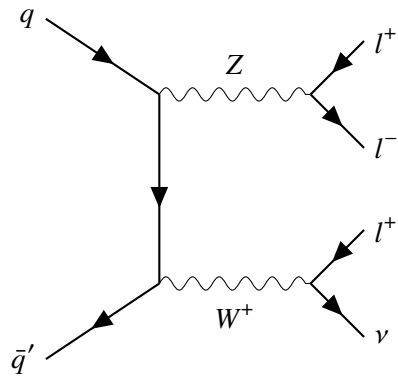
Figure 4.4: LO Feynman diagram showing production of W- and Z- decaying leptonically.
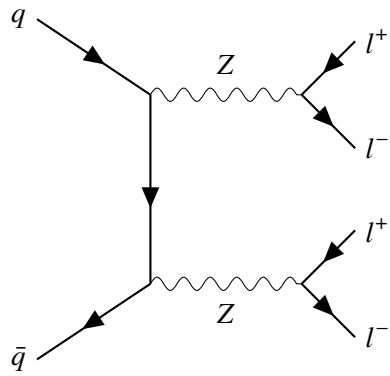

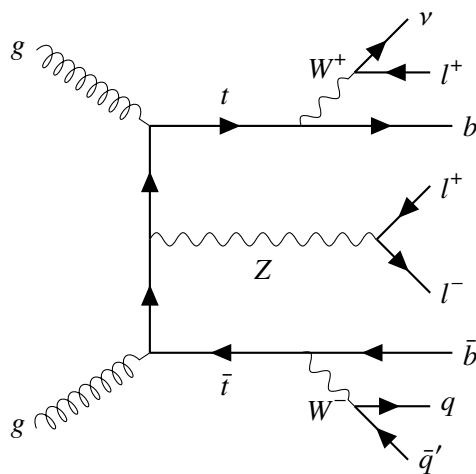Figure 4.5: Feynman diagram showing production of two Z-bosons at LO.

Figure 4.6: Feynman diagram of $t\bar{t}Z$ process at LO.

tWZ

Production of the single top-quark accompanied by two massive bosons is a rare process at the LHC. It yields three real leptons in the final state, provided two out of the three mentioned particles decay into leptons. Together with the leptonic decay of Z, third lepton can be considered from either the W-boson or the top-quark in the tWZ production. A tWZ production diagram is shown in Figure 4.7.
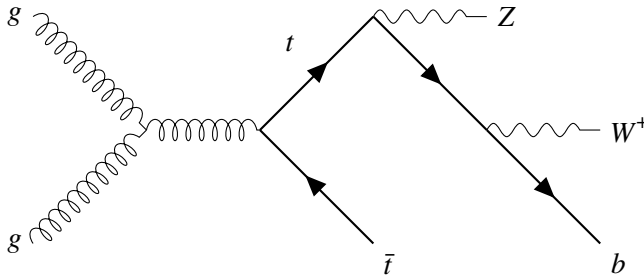

Figure 4.7: Feynman diagram of tWZ process at LO.

4.3 Datasets

Data recorded by the ATLAS detector is used for performing SM measurements and searching for new physics beyond the SM. This is generally done by comparing the recorded data with simulated Monte Carlo (MC) samples. MC is a software based calculation which is used to simulate events. Detailed description of MC simulations is given in Section 4.3.2. The ATLAS Top Working Group has developed a framework named `AnalysisTop` [36] which produces single top *ntuples* which are basically ROOT files containing the kinematic information of particles recorded by the detector (for data) or simulated kinematic values (for MC). In this thesis, Version 28 of the ntuples, produced using `AnalysisTop-21.2.58`, were used. These include data and MC for the aforementioned processes. For a differential cross-section measurement, a MC signal sample is required which contains truth-level and reconstruction-level information which is defined in Section 4.3.2.

4.3.1 Data Samples

This analysis investigates data from proton-proton collisions at $\sqrt{s}$ = 13 TeV, recorded by the ATLAS detector in the time period 2015 to 2018. Data obtained from the ATLAS detector are divided into *runs*. A run is referred to as the time period in which the detector records data without any interruption. The list of data usable for physics analyses is known as the *Good Runs List*. This list contains data recorded when the LHC beams were stable and all detector components were fully functional. Out of the total data recorded by the ATLAS detector during Run-2, 95.6 % is declared suitable for physics analyses [37]. Figure 4.8 presents values of the total integrated luminosity delivered by the LHC and values recorded by the ATLAS detector during Run-2.

4.3.2 Monte Carlo simulations

A typical collision event is constructed in a similar fashion as it might occur inside the collider. MC generators use known physics properties and distributions to simulate final state particles. The
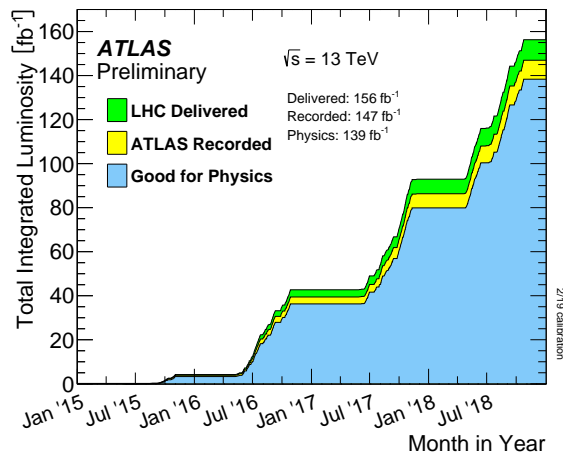
Figure 4.8: Plot showing the integrated luminosity delivered by the LHC and recorded by the ATLAS detector during 2015-2018. From the maximum recorded value, an integrated luminosity of 139 fb^{-1} is certified for physics analyses [38].

generated kinematic distributions are called *truth-level* information. In order to obtain reconstruction-level information, these generated events are exposed to detector effects. This procedure is called detector simulation and it is performed with a software called GEANT4.

Three campaigns called MC16a, MC16d and MC16e were dedicated to generate MC samples based on Run-2 detector conditions such as pile-up. MC16a was associated with pile-up conditions of 2015-2016; MC16d and MC16e for pile-up conditions of 2017 and 2018, respectively. All of them are used for Run-2 data analyses. For this analysis certain predefined conditions were considered. The mass of the top-quark was fixed to $m_t = 172.5$ GeV in all generated MC. Furthermore, tau leptons were only accounted for if they decay into leptons. Further details about the MC samples used in this thesis is given in Appendix A.

Simulations of signal and background processes

Simulation of the tZq signal sample at NLO was done by the MadGraph5_aMC@NLO v2.3.3 [39] generator using the NNPDF3.0NLO PDF [40]. The simulated tZq signal and background events followed the four-flavour scheme (4FS), in which masses of all quarks except the b-quark and the t-quark are set to zero. In order to obtain a 5FS prediction of the cross section, the events are scaled.

The $t\bar{t}$ and the $t\bar{t}H$ backgrounds were simulated using the PowhegBox [41] v2 MC generator while the $t\bar{t}V$ and the tWZ processes were simulated with the MadGraph5_aMC@NLO v2.3.3 generator. The Sherpa v2.2 generator [42] was used for diboson and Z + jets background simulations. An overview of generators used to simulate backgrounds is given in Table 4.1. Detailed information about MC event generators used in ATLAS analyses can be found in [43].

Weighting of MC events

In order to compare real collision data with simulated MC samples, it is important for the MC generator to duplicate detector conditions that prevailed during data taking. To ensure MC events are assigned

Process	MC generator	Parton Showering
$t\bar{t}$	`PowhegBox v2`	`Pythia 8.230`
Single-top	`PowhegBox v2`	`Pythia 8.230`
$t\bar{t}H$	`PowhegBox v2`	`Pythia 8.230`
$t\bar{t}V$	`MadGraph5_aMC@NLO v2.3.3`	`Pythia 8.210`
tWZ	`MadGraph5_aMC@NLO v2.3.3`	`Pythia 8.212`
Diboson	`Sherpa v2.2`	`Sherpa`
Z + jets	`Sherpa v2.2`	`Sherpa`

Table 4.1: Overview of generators used for simulations of backgrounds

certain weights. The weight assigned to a MC event can be written as: [44]

$$w_{\text{event}} = w_{\text{MC}} \cdot w_{\text{pileup}} \cdot w_{\text{lepton}} \cdot w_{\text{JVT}} \cdot w_{\text{trigger}} \cdot w_{\text{b-tagging}}. \tag{4.1}$$

Each weight is described as follows: [35]

- w_{MC} is the MC event weight. It is applied to obtain a correct estimate of number of events in a MC sample.

- $w_{\text{pile-up}}$ is the pile-up weight which is applied to ensure that the pile-up presumptions taken for MC matches the pile-up conditions of data.

- w_{lepton} is related to efficiency of lepton isolation and reconstruction.

- w_{JVT} is known as the jet-vertex-tagger (described in Section 3.3.3) weight. It takes into account the differences in efficiencies of applying cuts on the JVT discriminant for data and MC.

- w_{trigger} is the weight associated with trigger selection efficiency of data and MC.

- $w_{\text{b-tagging}}$ is implemented to obtain efficient b-tagging since we require b-tagged jets for the signal.

In addition to these weights, MC events are further scaled by the luminosity weight w_{lumi}. This weight is required so that MC sample and data have equal integrated luminosity. The luminosity weight:

$$w_{\text{lumi}} = \sigma_{\text{process}} \frac{\mathcal{L}}{N_0}$$

where σ_{process} is cross-section of the specific process, $\mathcal{L}$ is integrated luminosity overall and N_0 corresponds to the number of events in the original MC sample. The total weight, $w_{\text{total}} = w_{\text{event}} \cdot w_{\text{lumi}}$, is assigned to each MC event.

4.4 Event selection

Out of the innumerable decay products from the pp collisions reconstructed by the ATLAS detector, a finite number of events based on specific criteria are selected for any particular analysis. This step is

called preselection. For this analysis, a set of selection criteria in the form of cuts are applied to events in the MC and the data samples. Preselection procedure discards events which have different final states than tZq production in the trilepton decay mode.

In order to get selected for the tZq analysis, events are required to have exactly three leptons (electrons or muons) with $|\eta| < 2.5$. The transverse momentum of the highest lepton has to be $p_T(l_1) >$ 28 GeV while the other two leptons should have $p_T(l_2) > 20$ GeV and $p_T(l_3) > 20$ GeV. In addition to the lepton momenta requirements, the transverse momenta of jets should be greater than 35 GeV. The b-jets at $|\eta| < 2.5$ should be tagged at 70 % working point. Jets which are not b-tagged are called untagged jets. If a jet has a high eta value, it is then called a *forward jet*. These criteria are summarized in Table 4.2.

Selection requirements
Exactly 3 leptons with $\eta(l) < 2.5$
$p_T(l_1) > 28$ GeV, $p_T(l_2) > 20$ GeV, $p_T(l_3) > 20$ GeV
$p_T(\text{jet}) > 35$ GeV

Table 4.2: Summary of selection criteria (cuts) applied to events

4.4.1 Determination of the signal regions

Candidate events that have three leptons, one b-tagged jet, one untagged jet and missing transverse momentum form the signal region. Two of the three leptons must have opposite charge and same flavour (OSSF) used to reconstruct the Z-boson. Difference between the invariant mass of these leptons and the mass of the Z-boson should be less than 10 GeV. In cases where more than one lepton pairs are OSSF, then the pair which has an invariant mass closest to the mass of Z-boson is selected. The top-quark is reconstructed from the remaining lepton, b-tagged jet and missing transverse momentum. The untagged jet originating from the spectator quark is a forward jet. Candidate events that satisfy these requirements build up the SR-$2j1b$ signal region. There is a possibility of another untagged jet originating due to QCD radiation. This defines another signal region, SR-$3j1b$. The selection cuts for these signal regions are summarized in Table 4.3.

SR-$2j1b$	SR-$3j1b$
≥ 1 OSSF lepton pair	≥ 1 OSSF lepton pair
$|m_{ll} - m_Z| < 10$ GeV	$|m_{ll} - m_Z| < 10$ GeV
2 jets, $|\eta| < 4.5$	3 jets, $|\eta| < 4.5$
1 b-jet, $|\eta| < 2.5$	1 b-jet, $|\eta| < 2.5$

Table 4.3: Summary of the selection criteria applied on events that define signal regions

4.4.2 Determination of the control regions

Control regions are defined to estimate the contribution from background processes. There are six control regions associated with the main sources of backgrounds described in Section 4.2. The

diboson CRs, namely the $2j0b$ and $3j0b$ have same selection cuts as the signal region except there is no b-tagged jet. The $t\bar{t}(2j1band3j1b)$ CR contains events with at least one opposite sign different flavour lepton pair (OSDF) and zero OSSF pair. It is defined to have 2 or 3 jets out of which one is b-tagged. Since there are two b-jets in the $t\bar{t}$ production, its contribution is determined by a method called b-jet replacement method [45]. In addition, the jet multiplicity of the $t\bar{t}$ CRs is same as that of the SRs. To control the $t\bar{t}Z$ background, the $3j2b$ and the $4j2b$ control regions are defined with same criteria as the signal except higher jet multiplicity. These regions contain events with similar requirements as the signal region but with an additional b-tagged jet. Table 4.4 gives an overview of different control regions along with event selection criteria for each of them.

CR diboson $2j0b$	CR $t\bar{t}$ $2j1b$	CR $t\bar{t}Z$ $3j2b$
≥ 1 OSSF lepton pair	≥ 1 OSDF lepton pair	≥ 1 OSSF lepton pair
$\|m_{ll} - m_Z\| < 10$ GeV	0 OSSF lepton pair	$\|m_{ll} - m_Z\| < 10$ GeV
2 jets, $\|\eta\| < 4.5$	2 jets, $\|\eta\| < 4.5$	3 jets, $\|\eta\| < 4.5$
0 b-jets	1 b-jet, $\|\eta\| < 2.5$	2 b-jets, $\|\eta\| < 2.5$

CR diboson $3j0b$	CR $t\bar{t}$ $3j1b$	CR $t\bar{t}Z$ $4j2b$
≥ 1 OSSF lepton pair	≥ 1 OSDF lepton pair	≥ 1 OSSF lepton pair
$\|m_{ll} - m_Z\| < 10$ GeV	0 OSSF lepton pair	$\|m_{ll} - m_Z\| < 10$ GeV
3 jets, $\|\eta\| < 4.5$	3 jets, $\|\eta\| < 4.5$	4 jets, $\|\eta\| < 4.5$
0 b-jets	1 b-jet, $\|\eta\| < 2.5$	2 b-jets, $\|\eta\| < 2.5$

Table 4.4: Summary of selection criteria applied on events in the control regions

4.5 Uncertainties in measurements

Measurements, however accurate, carry with them a certain degree of uncertainty which can be interpreted as accuracy of the measurement. Uncertainties are classified into statistical and systematic uncertainties. Statistical uncertainties are a result of the stochastic fluctuations caused by a finite number of observations. A measurement based on small set of observations tend to have higher statistical uncertainties. On the other hand, systematic uncertainties are due to errors related to assumptions or approximations considered in the measurement; theoretical models used for inferences, or simulations and detector effects. If a measurement results into a continuous distribution, the uncertainties can be separated into two parts: rate uncertainty, associated with number of observations and the shape uncertainty that affects the shape of a distribution.

4.5.1 Sources of systematic uncertainties

Object reconstruction and calibration uncertainties

Uncertainties are aroused while reconstruction of physics objects and detector calibration. These uncertainties are associated with accurate measurements of the properties of particles. Properties such as energy and momenta of particles are measured by analysing events with clean signatures and then

comparing the results between data and MC simulations. The sources of systematics are choice of MC generator, selection criteria or data and MC disagreement. Different reconstruction and calibration uncertainties considered in the tZq analysis can be found in [1].

Background rate uncertainty

In order to measure the signal to background ratio in data, it is important to correctly estimate the background contribution using MC simulations. The MC modelling of different backgrounds give rise to systematic uncertainties. As these systematics modify the estimated number of background events, they are called background rate uncertainties.

Normalisation of diboson background process is performed by estimating its contribution in the SR using `Sherpa` and `Powheg+Pythia` generators. The difference in the estimated yields is taken as the background rate uncertainty for diboson production. Uncertainty in estimation of Z+jets and $t\bar{t}$ production is derived from a data-driven method as explained in [35]. MC samples of $t\bar{t}V$, $t\bar{t}H$ and tWZ backgrounds are normalised to their predicted cross-sections. An uncertainty is assigned due to the choice of PDF used to measure the cross-sections. Uncertainties in normalisation estimation of diboson, production of a Z-boson with jets, $t\bar{t}H$ and $t\bar{t}V$, and tWZ backgrounds are considered in this analysis.

Luminosity

There exists an uncertainty in the integrated luminosity measurement of the ATLAS detector. According to the ATLAS collaboration, there is an uncertainty of 1.7 % [46] in the combined luminosity measurement from 2015 to 2018. A variation of 1.7 % is applied to signal and all backgrounds.

4.6 Signal Extraction

4.6.1 Artificial Neural network

A neural network is a computation tool developed to function in a similar way as the human mind. It is widely used in high energy physics for data analysis. The structure of a neural network (NN) is made up of neurons or *nodes*. Their function is to examine unknown systems and identifying interesting features, just like the job of neurons in human mind. Generally, these nodes are arranged in three different layers: the input layer, the hidden layer and the output layer. A list of variables is given as input to the nodes of the input layer. Processing takes place through the subsequent layers and at the end, the output layer returns the conclusions derived by the network. Connections between nodes of different layers are referred to as the *synapses*. Each connection between nodes of two consecutive layers, has a weight associated to it. Figure 4.9 shows a diagram of a neural network.

The input received by each node is the sum of weighted output of all nodes of the previous layer. As given in Equation 4.2, y_j is the input to node j, w_{ij} is the weight from the i-th node and x_i is that node's output. The term w_{0j} is called bias.

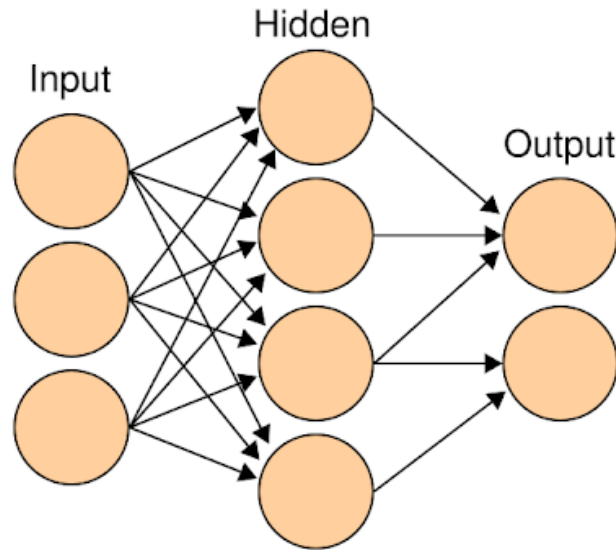$$y_j = \Sigma_{i=1}^{n} w_{ij} x_i + w_{0j} \qquad (4.2)$$

Figure 4.9: Diagram of a neural network including the input, hidden and output layers [47].

The output of a node is defined by an *activation* function. Common choice of an activation function is the sigmoid function. It provides output between 0 and 1. A feature that makes a NN special is its capability to *learn* from examples with known inputs and outputs. This is referred to as *training* a neural network. The purpose of training is to find appropriate weights. In supervised training, inputs and outputs are provided to a NN. It processes input and then compares the resultant output with the desired output. Comparison is done by calculating a *loss function*. It is a way to determine how well is the network trained. For better performance of a network the loss function should be minimised. In order to do that, errors of the resultant output are propagated back in a model and the initial weights are readjusted so that output is closer to the desired output. This is how a network learns. A dataset flows inside a network several times and each time weights are refined until a minimum value of the loss function is obtained.

NNs for the tZq analysis

The `NeuroBayes` [48] package is used for the tZq multivariate analysis. A set of variables, shown in Table 4.5 and Table 4.6, is provided to the network so that it learns to differentiate between tZq and other processes. The preprocessing of input data transforms the input variables values into a Gaussian distribution with standard deviation of 1 and mean of 0. The output layer has a single node which provides a value between -1 and 1. Events with response -1 are interpreted as background and events with response of 1 are considered signal. In this way, a NN is used to separate signal and background.

For each SR defined, a NN was trained using MC samples with the same set of 15 variables. Each neural network takes as input 15 kinematic variables. Details of neural network training in the tZq analysis can be found in [1].

Variable	Rank	Definition
m_{bj_f}	1	(Largest) invariant mass of the b-jet and the untagged jet(s)
m_{top}	2	Reconstructed top-quark mass
$|\eta(j_f)|$	3	Absolute value of the η of the j_f jet
$m_T(l, E_T^{\text{miss}})$	4	Transverse mass of the W-boson
b-tagging score	5	b-tagging score of the b-jet
H_T	6	Scaler sum of the p_T of the leptons and jets
$q(l_W)$	7	Electric charge of the lepton from the W-boson decay
$|\eta(l_W)|$	8	Absolute value of the η of the lepton from the W-boson decay
$p_T(W)$	9	p_T of the reconstructed W-boson
$p_T(l_W)$	10	p_T of the lepton from the W-boson decay
$m(ll)$	11	Mass of the reconstructed Z boson
$|\eta(Z)|$	12	Absolute value of the η of the Z boson
$\Delta R(j_f, Z)$	13	ΔR between the j_f jet and the reconstructed Z boson
E_T^{miss}	14	Missing tranverse energy
$p_T(j_f)$	15	p_T of the j_f jet
$\eta(j_r)$	-	Absolute value of the η of the j_r jet
$p_T(Z)$	-	p_T of the reconstructed Z boson
$p_T(j_r)$	-	p_T of the j_r jet

Table 4.5: List of all variables used for training the tZq signal against the backgrounds in SR 2j1b. Ranks of the variables are also given [1].

4.6.2 Likelihood fit

In statistics, when a distribution of a variable X is known, the probability of a certain observed value of X can be measured using its probability density function. However, in cases where observations of X are known but its distribution is unknown, a likelihood function is used to estimate the underlying distribution. A likelihood function is defined as a function of parameters associated with a distribution of data points. In high energy physics, most analyses are based on counting experiments in which events are distributed in *bins* forming a histogram. A binned likelihood function for a variable X can be written as:

$$
\begin{aligned}
L(k, \theta) &= \prod_{i=\text{bins}} P(n_i | S_i(k_i, \theta) + B_i(k_i, \theta)) \prod_{j=\text{syst}} \mathcal{G}(\theta_j) \\
&= \prod_{i=\text{bins}} e^{-\nu_i} \frac{\nu_i^{n_i}}{n_i!} \prod_{j=\text{syst}} \mathcal{G}(\theta_j)
\end{aligned}
\tag{4.3}
$$

In Equation 4.3, k is a set of unconstrained parameters such as the parameter of interest (POI). Depending on the analysis, POI can be signal strength or cross-section. θ is a set of nuisance parameters associated with systematic uncertainties. Corresponding to each source of systematic uncertainty, there is a unique nuisance parameter in the likelihood model. A likelihood model is constructed from data and simulated events which are considered to follow Poisson distribution. For each bin, n is number of observed events while S and B are signal and background expectations

Variable	Rank	Definition
m_{bj_f}	1	(Largest) invariant mass of the b-jet and the untagged jet(s)
m_{top}	2	Reconstructed top-quark mass
$\|\eta(j_f)\|$	3	Absolute value of the η of the j_f jet
$m_T(l, E_T^{\text{miss}})$	4	Transverse mass of the W-boson
b-tagging score	11	b-tagging score of the b-jet
H_T	-	Scaler sum of the p_T of the leptons and jets
$q(l_W)$	8	Electric charge of the lepton from the W-boson decay
$\|\eta(l_W)\|$	12	Absolute value of the η of the lepton from the W-boson decay
$p_T(W)$	15	p_T of the reconstructed W-boson
$p_T(l_W)$	14	p_T of the lepton from the W-boson decay
$m(ll)$	-	Mass of the reconstructed Z boson
$\|\eta(Z)\|$	13	Absolute value of the η of the Z boson
$\Delta R(j_f, Z)$	7	ΔR between the j_f jet and the reconstructed Z boson
E_T^{miss}	-	Missing tranverse energy
$p_T(j_f)$	10	p_T of the j_f jet
$\eta(j_r)$	5	Absolute value of the η of the j_r jet
$p_T(Z)$	6	p_T of the reconstructed Z boson
$p_T(j_r)$	9	p_T of the j_r jet

Table 4.6: List of all variables used for training the tZq signal against the backgrounds in SR 3j1b. Ranks of the variables are also given [1].

respectively. Signal and background predictions can be summed and written as v_i. Assuming that systematic uncertainties are uncorrelated, their effect on the signal and background events can be parametrised by a product of Gaussian functions $\mathcal{G}$ for all systematic uncertainties j.

A likelihood function estimates parameter values by performing a maximum likelihood (ML) fit of a model to data. A set of parameters which offer a maximum value of a likelihood function are called best fit values. They are considered to best describe data. Generally, instead of maximising the likelihood function, its negative logarithm -2ln(L), is minimized. For this purpose a tool called Minuit [49] is used.

For the tZq analysis, a ML fit is performed by `TRExFitter` [50, 51]. It is a framework that builds likelihood models by taking histograms as inputs and performing ML fits. In order to do a likelihood fit, `TRExFitter` uses a tool called `HistFactory` [52]. Histograms associated with the SRs and CRs described in Section 4.4 are provided as input. Parameter of interest in this model is the signal strength $\mu_{sig} = \sigma_{tZq}/\sigma_{tZq}^{theo}$.

Unfolding methods to measure differential cross-sections

This chapter presents different techniques used in this thesis for differential cross-section measurements. Section 5.1 presents a brief motivation behind the measurements. Section 5.2 describes the unfolding methods implemented in this work. The methods of estimating uncertainties are explained in Section 5.3. A distinction between parton level and particle level unfolding is given in the final section.

5.1 Motivation

Cross-section measurements provide an overview of a process. In order to study a process in detail, differential cross-section measurements are performed. One can measure the cross section of a process with an inclusive measurement of some production and decay channel. In contrast, a differential measurement allows one to see how the cross section behaves as a function of kinematic and reconstructed variables. This information is beneficial as BSM particles may modify these distributions. Differential cross-sections are sensitive to MC generators, hence they can be used to tune MC parameters and obtain more accurate simulations.

One of the ways to perform a measurement accurately is by using unfolding methods. It is required if outcomes need to be compared with the results from other detectors or theoretical models.

5.2 Unfolding

5.2.1 General concept

In any experiment, the accuracy of measurement highly depends on performance of the apparatus being used. In particle physics, an ideal detector provides the original and complete information of collisions but in reality, the data received from a detector is distorted due to various effects such as limited acceptance and finite resolution. *Unfolding* is a technique to estimate the original data devoid of these detector effects.

Ideally, observed data should be comparable to generated events before the detector is simulated. Using unfolding tactics, one can revert detector effects and estimate the truth-level data from the observed data. This is also called unsmearing or deconvolution. Figure 5.1 shows an example of

original and distorted spectra. Unfolding methods are applied on the distorted spectrum to restore the original fine structure. In contrast, the process of obtaining a smeared distribution from a true distribution is called *folding*.
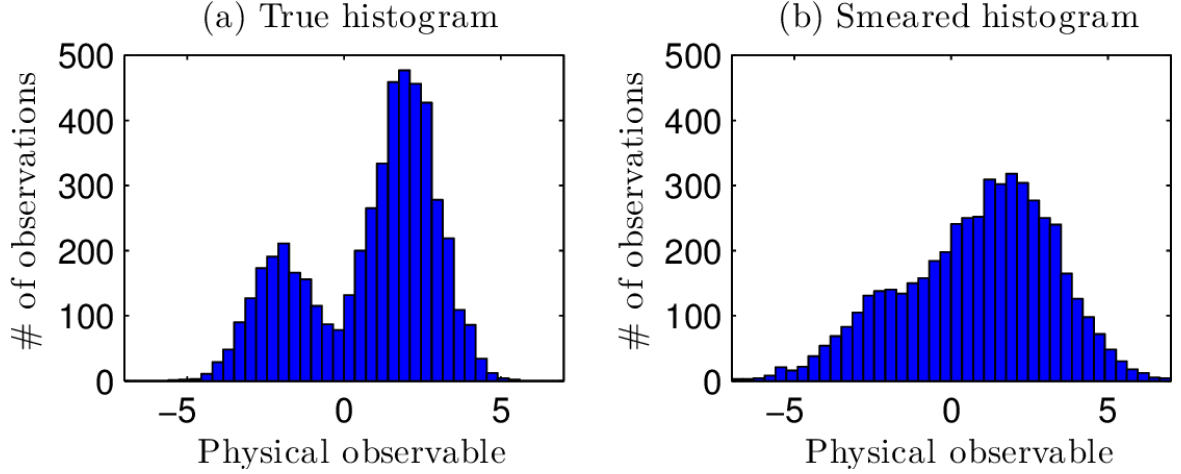

Figure 5.1: An example of an original spectrum (left) and smeared spectrum (right) [53].

Let x be a continuous variable with probability density function $f_{\text{meas}}(x)$ and y is associated with the true values of x. The measured and true density functions are related by response matrix $\mathcal{R}$ by [54]

$$f_{\text{meas}}(x) = \int \mathcal{R}(x|y) f_{\text{true}}(y). \tag{5.1}$$

If x is discrete, then Equation 5.1 can be written similarly as

$$x_i = \sum_{j=1}^{\text{bins}} \mathcal{R}_{ij} y_j. \tag{5.2}$$

Here, x_i corresponds to an observed value of x in bin i where the true value y is in bin j. Both are related by a *response* matrix $\mathcal{R}_{ij}$ which can be defined as a conditional probability:

$$\mathcal{R}_{ij} = \text{P(observed in bin } i|\text{true value in bin } j)$$

A response matrix quantifies the detector effects and smears the original information. Depending on number of bins in true and observed distributions, it can be square or non-square. In particle physics, unfolding techniques are applied to distributions of kinematic variables associated with final state particles. For this purpose, a response matrix is calculated from MC simulations. Moreover, x_i is represented by n_i which is the number of signal events in bin i. While dealing with detector data, one also needs to account for background events b. Therefore Equation 5.2 becomes,

$$\vec{x} = \vec{n} = \mathcal{R}\vec{y} + \vec{b} \tag{5.3}$$

Mathematically, the idea of unfolding is to solve Equation 5.3 for given $\mathcal{R}$, x and b. The resultant values of y can be interpreted as determined true number of events at the truth-level.

5.2.2 Matrix inversion

Looking at Equation 5.3, one would notice a simple way to find the estimators by inverting the response matrix,

$$\vec{y} = \mathcal{R}^{-1}(\vec{x} - \vec{b}) \tag{5.4}$$

For i-th and j-th bin in measured and true distributions respectively,

$$y_i = \sum_{j=1}^{\text{bins}} \mathcal{R}_{ij}^{-1}(n_j - b_j) \tag{5.5}$$

Equation 5.5 can be written in terms of sub-components of $\mathcal{R}$; namely efficiency (ϵ), acceptance (a) and the migration matrix (M):

$$y_i = \frac{1}{\epsilon_i} \sum_{j=1}^{\text{bins}} M_{ij}^{-1} a_j (n_j - b_j) \tag{5.6}$$

The reconstruction-level and truth-level distributions are used to compute the sub components of a response matrix. These are defined as follows: [55]

- Efficiency describes the number of events found at the truth level but do not exist at the reconstruction level.

- Acceptance provides the number of events existing at the reconstruction-level but not found at the truth-level.

- Migration matrix describes bin-to-bin migrations occurring in both observed and true distributions [56]. An off-diagonal component of the migration matrix, M_{ij}, gives the probability that an event with true value in bin j is reconstructed in bin i. The inverse of the migration matrix (M^{-1}) is called the unfolding matrix.

Although matrix inversion method is easy to implement, it is a strategy that one should avoid because of its limitations: in some situations, the response matrix is non-invertible then Equation 5.4 becomes ill-posed. Assume inversion is possible, statistical fluctuations in the observed data may cause negative entries in the unfolding matrix. This leads to negative number of events in the unfolded distribution which is unrealistic. When a response matrix acts on a true spectrum, it distorts any fine structure present at the truth-level. Despite of that, some residue of this fine structure still remains in the reconstructed spectrum [54]. The inverted matrix, acting on the measured data, assumes its statistical fluctuations are the residual fine structure and restores it. In this way, statistical fluctuations are amplified in the unfolded distribution [57] which is undesirable. Figure 5.2 shows the effect of matrix inversion.

In order to overcome the limitations of matrix inversion, various unfolding methods are developed. In the following sections, profile likelihood unfolding with regularisation and iterative Bayesian unfolding are described in detail as they are techniques used to measure the differential cross-sections.
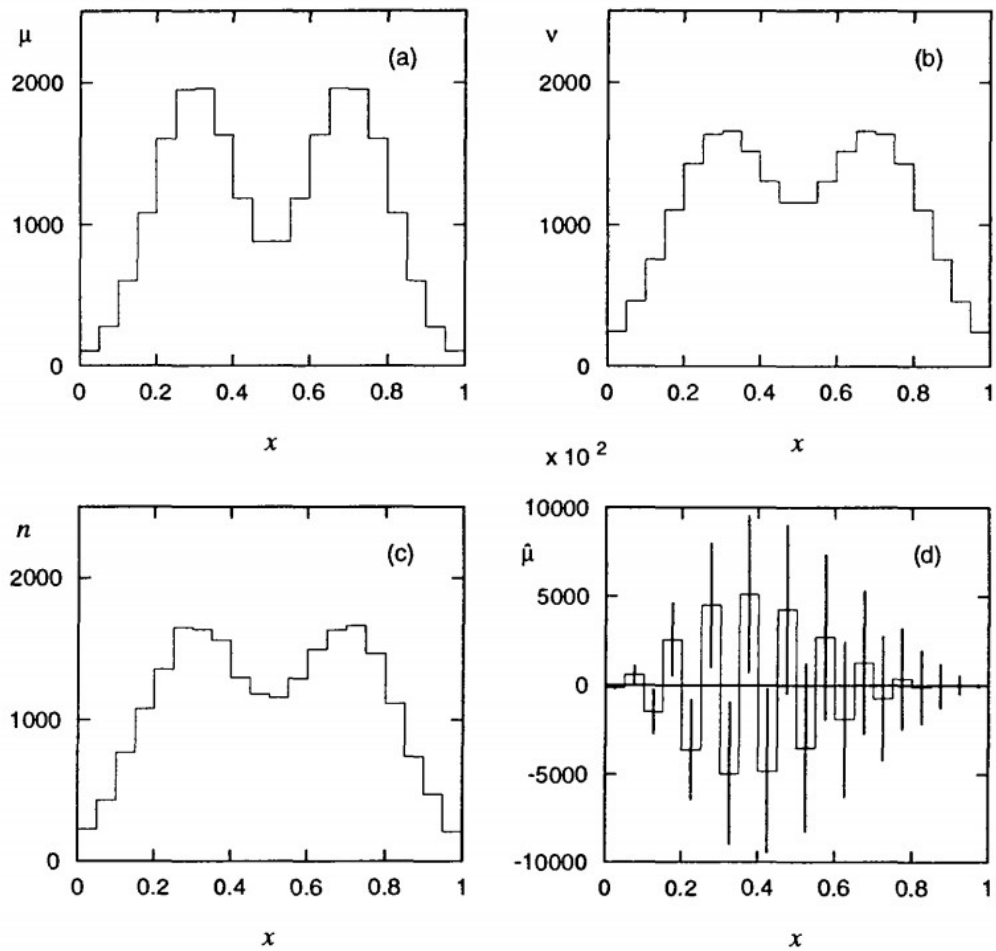
Figure 5.2: The top-left figure is an example of a truth-level distribution. The top-right figure shows how a reconstructed distribution is expected to look like and the bottom-left figure is the measured distribution. The bottom-right figure is the unfolded distribution obtained by matrix inversion [54].

5.2.3 Profile Likelihood Unfolding

General idea

In this method, unfolding is done by performing a maximum likelihood fit. Profile likelihood unfolding (PLU) [58, 59] executes a similar fitting procedure as explained in Section 4.6.2 except additional parameters are employed. Apart from the parameter of interest and nuisance parameters, new unconstrained parameters, called the normalisation factors (NFs), are introduced in the model. They are associated with the shape of the unfolded distribution. *Profiling* typically means to incorporate systematic uncertainties into a fit model.

In PLU, the problem of unfolding is transformed into multi-dimensional likelihood maximisation by assigning one POI and one NF to each bin of the truth distribution. In this analysis, a normalisation factor is interpreted as the number of unfolded events in each bin and the parameter of interest (μ) is defined as the ratio of unfolded data events over the SM prediction.

Implementation

PLU is implemented within the `TRExFitter` framework. The procedure begins by *folding* each bin of the truth distribution (referred to as truth bins) using a response matrix. This will result into sub-samples of folded truth distribution. If there are N truth bins, N separate sub-samples are created. Afterwards, a profile likelihood fit of the reconstructed distribution is performed on the sum of these sub-samples. This step results into N normalisation factors corresponding to each folded truth bin. Now, the nominal truth distribution is scaled by the obtained NFs. This result of this scaling is the required unfolded distribution. For a kinematic variable X in bin i, a differential cross-section can be calculated by dividing the unfolded yields by bin width ΔX and luminosity $\mathcal{L}$ as presented in Equation 5.7.

$$\frac{\mathrm{d}\sigma_{\mathrm{PLU}}}{\mathrm{d}X^i} = \frac{1}{\mathcal{L} \cdot \Delta X^i} N^i_{\mathrm{unf}} \tag{5.7}$$

where unfolded bin contents N_{unf} are calculated from observed events N_{obs} and background events N^j_{bkg} by,

$$N^i_{\mathrm{unf}} = \sum_{j=1}^{\mathrm{bins}} \mathcal{R}^{-1}_{ij} (N^j_{\mathrm{obs}} - N^j_{\mathrm{bkg}}) = \frac{1}{\epsilon_i} \sum_{j=1}^{\mathrm{bins}} M^{-1}_{ij} a_j (N^j_{\mathrm{obs}} - N^j_{\mathrm{bkg}}). \tag{5.8}$$

Acceptances are calculated as a ratio of number of events at reconstructed and truth-level to the number of events at reconstructed level only [56],

$$a_j = \frac{N^j_{\mathrm{truth} \wedge \mathrm{reco}}}{N^j_{\mathrm{reco}}}. \tag{5.9}$$

In cases where $N^j_{\mathrm{truth} \wedge \mathrm{reco}} > N^j_{\mathrm{reco}}$, which might happen due to negative total event weight, the acceptance was set to the default 1. The efficiency is the ratio of events at reconstructed and truth-level

to the events at truth-level only,

$$\epsilon_j = \frac{N^i_{\text{truth} \wedge \text{reco}}}{N^i_{\text{truth}}}. \tag{5.10}$$

The parameter of interest that is the signal strength associated with bin i is,

$$\mu_i = \frac{(\mathrm{d}\sigma/\mathrm{d}X^i)_{\text{PLU}}}{(\mathrm{d}\sigma/\mathrm{d}X^i)_{\text{truth}}} \tag{5.11}$$

where $(\mathrm{d}\sigma/\mathrm{d}X^i)_{\text{truth}}$ is the cross-section calculated from truth-level distribution.

Regularisation in PLU

During the unfolding process, statistical fluctuations may be amplified leading to large uncertainties in the final distribution. Regularisation is a mathematical technique to impose a level of smoothness on the unfolded distribution. It can be achieved by adding a constraint term (or penalty term) to the original likelihood function defined in Equation 4.3. The modified likelihood function $L(\mu', \theta')$ can be written as [60],

$$L(\mu', \theta') = \prod_{i=\text{bins}} P(n_i | S_i(\mu'_i, \theta'_i) + B_i(\mu'_i, \theta'_i)) \times \prod_{j=\text{syst}} C(\theta'_j) + e^{-\frac{1}{2}\tau^2 \sum (\mu'_i - \mu_i)^2} \tag{5.12}$$

where, μ_i is the nominal value of the parameter interest and μ'_i is the value obtained after the constraint term is added. τ is defined as the regularisation parameter and its value decides the strength of regularisation.

This term adds additional constraint for the selection of events from the relevant distributions, to determine the likelihood. Due to this, any nonphysical features which may cause statistical fluctuations, are not allowed to enter the likelihood model. As a result, the uncertainties on the regularised solution are reduced. However, by adding a penalty, the expected unfolded output deviates from the non regularised expected output [57]. Thus, regularisation leads to a finite level of bias on the output.

Regularisation is a compromise between bias and error in measurement. Therefore, it is important to decide the extent of regularisation. There are various regularisation schemes used in particle physics. The *Tikhonov* [61] scheme is used in this analysis. Conventionally, there is no regularisation when τ is set to zero. One can select different tau values for each bin.

5.2.4 Bin-by-bin unfolding

In this method, correction factors are calculated from MC samples. A correction factor K_i for bin i is expressed as: [54]

$$K_i = \frac{N^i_{\text{truth}}}{N^i_{\text{reco}}} \tag{5.13}$$

where N^i_{truth} and N^i_{reco} are the number of true and reconstructed events in bin i respectively. Unfolded yields can be obtained by multiplying correction factors to the difference of observed (N^i_{obs}) and estimated background (N^i_{bkg}) events,

$$N_{\text{unf}}^i = K_i \cdot (N_{\text{obs}}^i - N_{\text{bkg}}^i) \tag{5.14}$$

The expression for the differential cross-section with respect to variable X can be written similar to Equation 5.7 as,

$$\frac{\mathrm{d}\sigma_{\text{BBB}}}{\mathrm{d}X^i} = \frac{K_i}{\mathcal{L} \cdot \Delta X^i} \cdot (N_{\text{obs}}^i - N_{\text{bkg}}^i). \tag{5.15}$$

Bin-by-bin unfolding (BBB) is sensitive to differences between data and MC and that is only possible where MC and data agree. It is necessary to select a MC generator which can model data well. Thus by construction, BBB is sensitive to the choice of MC generator. Moreover, it is required to have equal binning of the truth and reconstructed level histograms. Correction factors are estimated for each bin individually which means it can not account for bin-to-bin migrations. Therefore, it is only beneficial to use this method if migrations can be neglected.

5.2.5 Iterative Bayesian unfolding

D'Agostini [62] proposed a method called iterative Bayesian unfolding (IBU) which makes use of Bayes' theorem. To describe this method, consider true events as *causes* ($C_i, i = 1, 2, ..., n_C$) and reconstructed events as *effects* ($E_j, j = 1, 2, ..., n_j$). The conditional probability that a cause C_i gave rise to effect E_j, denoted by $P(C_i|E_j)$, is given by Bayes' theorem:

$$P(C_i|E_j) = \frac{P(E_j|C_i)P(C_i)}{P(E_j)} \tag{5.16}$$

where, $P(E_j|C_i)$ can be interpreted as probability of reconstructed event given true event which is the element M_{ij} of the migration matrix. Consequently, $P(C_i|E_j)$ can be identified as the unfolding matrix. One can determine the number of events ($\hat{n}$) due to cause C_i as

$$\hat{n}(C_i) = \frac{1}{\hat{\epsilon}_i} \sum_{j=1}^{n_E} \hat{n}(E_j)P(C_i|E_j). \tag{5.17}$$

It is important to note that the total number of events due to all causes and all effects are equal because only migration effects are considered so far. By dividing both the sides of Equation 5.17 by total number of events, we obtain

$$P(C_i) = \frac{1}{\hat{\epsilon}_i} \sum_{j=1}^{n_E} P(E_j)P(C_i|E_j). \tag{5.18}$$

Here, $P(C_i)$ is the unfolded distribution. The steps performed in iterative Bayesian unfolding to find $P(C_i)$, are shown in Figure 5.3 and explained below:

- An initial guess $P_0(C_i)$ is made and inserted into Equation 5.18. $P(E_j)$ is obtained from MC reconstructed distribution. The solution provides $P(C_i|E_j)$ which is the unfolding matrix.

- The obtained $P(C_i|E_j)$ is used in Bayes' theorem (Equation 5.16) to get a value of $P(C_i)$ which is different from the initial guess.

- This process is repeated for number of iterations specified by user.
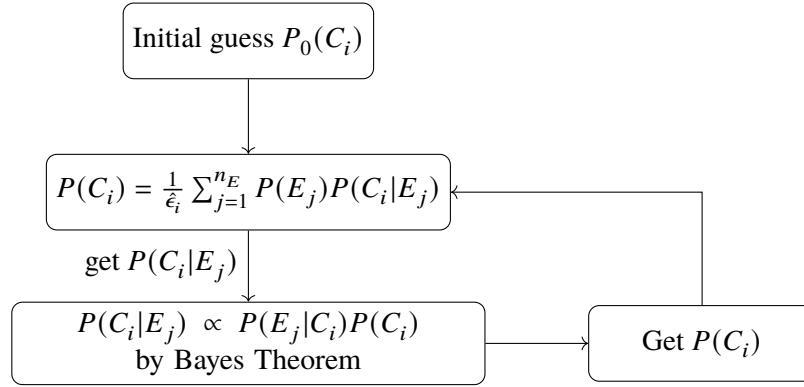
Figure 5.3: Flow chart showing steps followed in iterative Bayesian unfolding

This technique is implemented in the `RooUnfold` [63] software package. The unfolding matrix obtained by performing IBU can be used to calculate unfolded yields and consequently measure differential cross-section. Equation 5.6 and Equation 5.7 can be used to derive the expression

$$\frac{d\sigma_{\text{IBU}}}{dX^i} = \frac{1}{\mathcal{L} \cdot \Delta X^i \cdot \epsilon_i} \sum_{j=1}^{\text{bins}} M_{ij}^{-1} a_j (N_{\text{obs}}^i - N_{\text{bkg}}^i). \tag{5.19}$$

In iterative Bayesian unfolding, there is no involvement of response matrix inversion. In addition, it accounts for migrations between different bins unlike bin-by-bin unfolding.

5.3 Estimation of uncertainties

The procedure adapted for uncertainty estimation in the unfolded distributions is described in the following sections. Statistical uncertainties are estimated for profile likelihood, bin-by-bin and iterative Bayesian unfolding while systematic uncertainties are included only for profile likelihood unfolding.

Estimating statistical and systematic uncertainties in profile likelihood unfolding

In PLU, the best-fit parameter values determine the unfolded yields. Hence, the uncertainties associated with the parameter determination are reflected in the unfolded results. As mentioned in Section 4.6.2, Minuit is used for minimizing the log-likelihood and giving the best fit values of the parameters. In order to calculate the statistical uncertainties, Minuit processors, namely Migrad and Hesse, generate a covariance matrix (or error matrix). It is produced by inverting the matrix of second derivatives of the likelihood function [64]. In this calculation, correlations between the parameters are taken into account. Afterwards, a statistical error equal to the square root of diagonal elements of the covariance matrix is assigned to the parameters.

The inclusion of systematic uncertainties on the unfolded distribution can be done using response matrix for each source of systematic uncertainty. In addition, specific weights corresponding to the impact of each systematic uncertainty are given. These weights are interpreted as up and down variation of the observed distribution. The framework efficiently constraints the nuisance parameters by transforming the up and down variation into a continuous variation.

Estimating statistical uncertainties in bin-by-bin unfolding

The way bin-by-bin unfolding works does not include any bin-to-bin correlations. Due to this, there is no requirement of a covariance matrix for error estimation. The Gaussian error propagation is used to determine statistical uncertainty on bin-by-bin unfolded distributions,

$$\delta\left(\frac{\mathrm{d}\sigma_{\mathrm{BBB}}}{\mathrm{d}X^i}\right) = \frac{K_i}{\mathcal{L}\cdot\Delta X^i}\cdot\sqrt{N_{\mathrm{obs}}^i} \tag{5.20}$$

where δ is used to denote statistical uncertainty.

Estimating statistical uncertainties in iterative Bayesian unfolding

Iterative Bayesian unfolding allows for correlations between bins to be included. In order to calculate the necessary covariance matrix, a bootstrap method is implemented as described in [65]: Fluctuate each event in the MC reconstructed sample by a random number from a Poisson distribution with mean one. Each event in the sample has a unique event-number associated with it. This event-number is given as a *seed* to the random number generator, a seed is a value used to initialise the generator. In other words, fluctuation of each individual event is associated with a unique seed. Fluctuating all events, gives a replica of the reconstructed sample. This is one toy experiment.

Similarly several toy experiments can be performed to obtain replicated samples. Iterative Bayesian unfolding is applied on these samples using the nominal unfolding matrix. From the output, a covariance matrix is computed using,

$$C_{ij} = \frac{1}{N_{\mathrm{toys}}}\sum_{k=1}^{N_{\mathrm{toys}}}\left(N_{\mathrm{unf}}^{i,k} - \overline{N_{\mathrm{unf}}^i}\right)\left(N_{\mathrm{unf}}^{j,k} - \overline{N_{\mathrm{unf}}^j}\right) \tag{5.21}$$

where N_{toys} are the number of toy experiments. For bins i and j, $N_{\mathrm{unf}}^{i(j),k}$ are the unfolded yields and $\overline{N_{\mathrm{unf}}^{i(j)}}$ are the mean values of the bin contents for all experiments: $\overline{N_{\mathrm{unf}}^i} = 1/N_{\mathrm{toys}}\sum_{\mathrm{toys}}N_{\mathrm{unf}}^i$. The statistical uncertainty associated with each bin of the unfolded distribution is:

$$\delta(N_{\mathrm{unf}}^i) = \sqrt{C_{ii}} \tag{5.22}$$

5.4 Normalised differential cross-section

A relative quantity called normalised differential cross-section can be derived. Given that the total cross-section can be written as

$$\sigma = \sum_{i=1}^{\mathrm{bins}}\frac{\mathrm{d}\sigma}{\mathrm{d}X^i}\Delta X^i = \sum_{i=1}^{\mathrm{bins}}\frac{N_{\mathrm{unf}}^i}{\mathcal{L}}, \tag{5.23}$$

the expression for normalised differential cross-section is defined as

$$\frac{1}{\sigma}\frac{\mathrm{d}\sigma}{\mathrm{d}X^i} = \frac{N_{\mathrm{unf}}^i}{X^i\sum_{j=1}^{\mathrm{bins}}N_{\mathrm{unf}}^i}. \tag{5.24}$$

5.5 Parton level and particle level unfolding

Parton level unfolding is performed when MC truth-level information of the particle that needs to be analysed, is directly available. In case of the tZq process, full kinematic information of the top-quark was available at parton level. In addition, there are no cuts applied to the truth-level distribution. In this thesis, particles are considered at parton level, i.e before their decay.

Particle level unfolding is done if distribution of the particle which is to be investigated is not available directly. For example, the top quark distribution in the tZq production, is required to be reconstructed from the W-boson and the b-quark which are in turn reconstructed from their decay products. In particle level unfolding cuts are applied on the truth level distributions.

Results

The migration matrix, acceptances and efficiencies required for the unfolding procedure are provided in Section 6.1. Section 6.2 describes a series of validation tests undertaken to demonstrate that the unfolding framework performs as expected. The parton-level profile likelihood unfolding is performed on distributions of $p_T(W)$ and $p_T(t)$. The results are presented in Section 6.3. A brief comparison between iterative Bayesian, profile-likelihood and bin-by-bin is given in the final part of this chapter.

6.1 Preparations for unfolding

Signal Purity

For differential cross-section measurements, a cut on the NN output was imposed in order to obtain more signal to background ratio. Neural network used for cross-section measurement, described in Section 4.6.1, are used here as well. The set of variables shown in Table 4.5, remain unchanged. Event yields from both SRs were summed up in every bin (see Figure 6.1). A cut $O_{NN} > 0.6$ was applied which resulted into a signal to background ratio greater than one in the remaining bins.
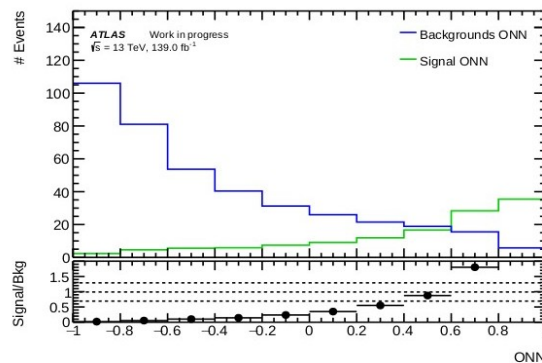
Figure 6.1: Distribution of O_{NN} [66].

(a) Acceptances for $p_T(W)$ (b) Acceptances for $p_T(t)$
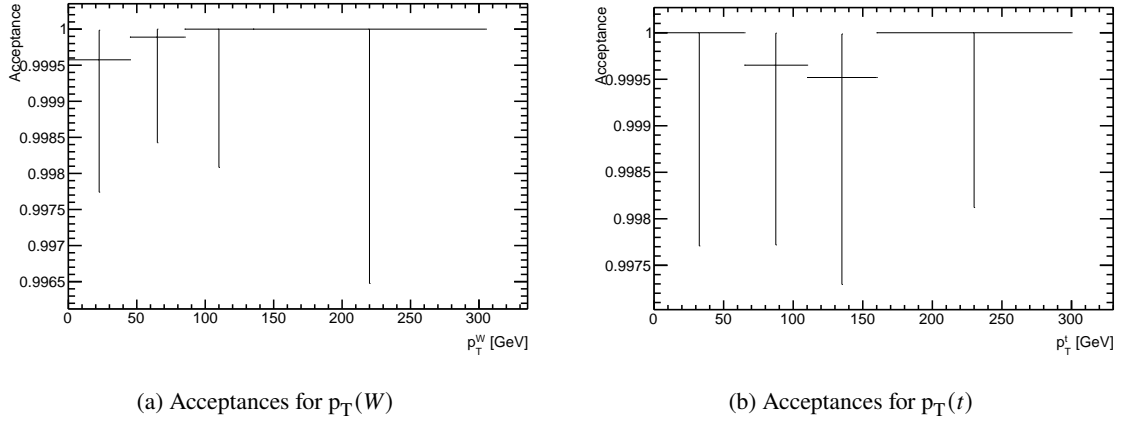
Figure 6.2: Distributions of acceptances

Choice of variables, binning and regularisation parameter

In this analysis, distributions of transverse momenta of the top-quark and the W-boson decaying from it, are unfolded. Due to insufficient kinematic information of the Z-boson, no variable of the Z-boson was considered. An important factor to take into account while unfolding, is the binning of the reconstructed and the truth distributions. An optimised binning is required which can have enough statistics in each bin so that the unfolded results are reliable and statistical fluctuations are minimised. In addition to this criteria, the binning was chosen in such a way that the diagonal elements of the migration matrix are greater than 60 %. This condition was also implemented in previous theses [66, 67].

The chosen binning returned the smallest value of χ^2 when the MC unfolded sample was compared to the truth sample. For $p_T(t)$, 4 bins were selected with the binning of $[0, 65, 110, 160, 300]$ (all values in GeV). The upper bound is fixed to 300 GeV because less than 5 % of the simulated events have momentum greater than 300 GeV. No overflow bins are taken into account since the differential cross-section calculation requires a division by the bin width ΔX_i (refer to Section 5.2.3). For $p_T(W)$, 4 bins were selected with a binning of $[0, 45, 85, 135, 305]$.

In case of profile likelihood unfolding, values of the regularisation parameter (tau) were selected by looking at the changes in bin correlations caused by different values. The change in correlations due to different values of tau is explained in Section 6.3.4. In addition to the non regularised case, i.e $\tau = 0$, two more values of τ were considered: $\tau = 1$ and $\tau = 1.5$. Due to time constraint, amount of bias added to the unfolded results due to different values, was not calculated.

Unfolding requirements

Acceptances and efficiencies are calculated according to the formula given in Section 5.2.3. The resulting distributions are shown in Figure 6.2 and Figure 6.3. Uncertainties are determined using Clopper-Pearson intervals at 68 % confidence interval. The migration matrices for both the unfolded variables are shown in Figure 6.4 and Figure 6.5.

(a) Efficiencies for $p_T(W)$

(b) Efficiencies for $p_T(t)$
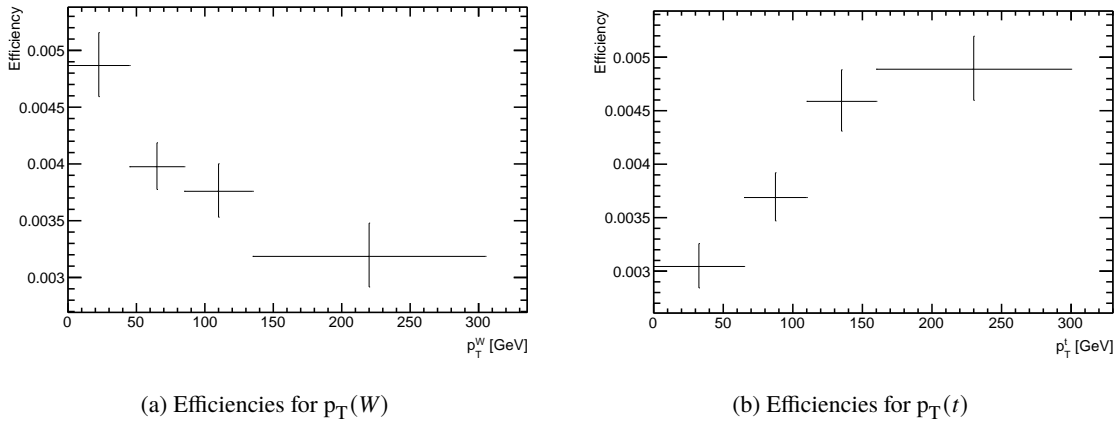
Figure 6.3: Distributions of efficiencies
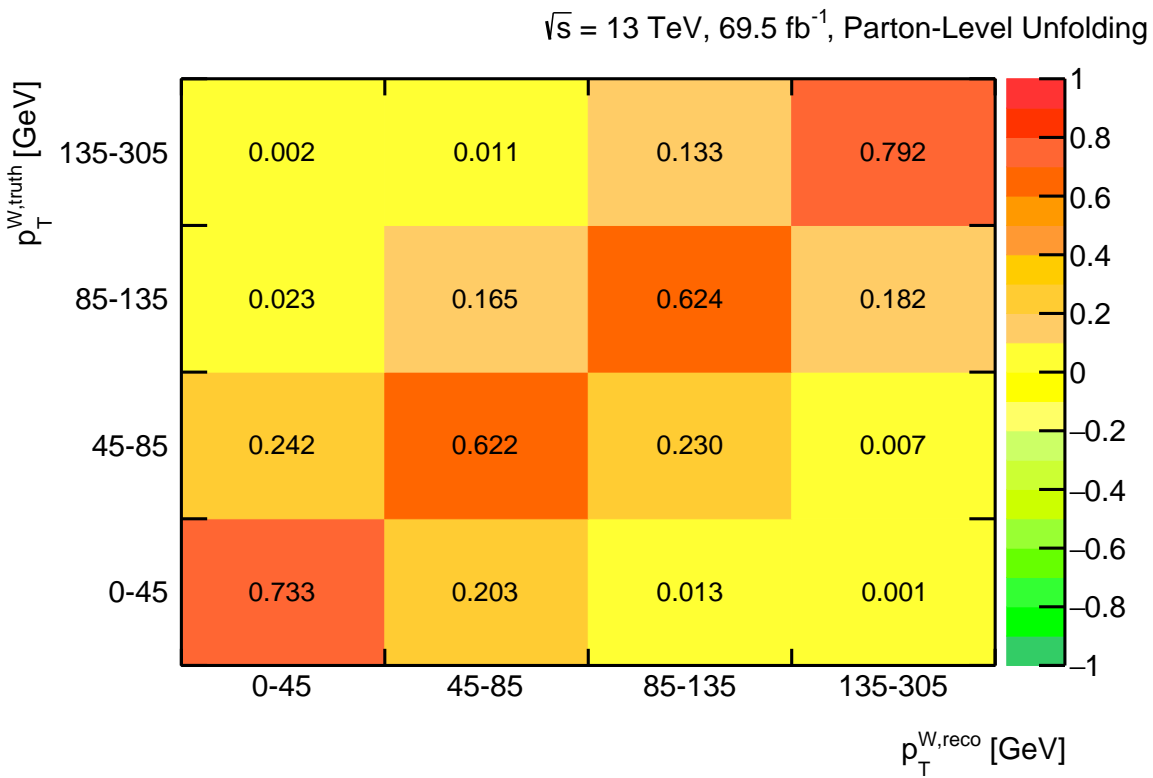
Figure 6.4: Migration matrix for $p_T(W)$
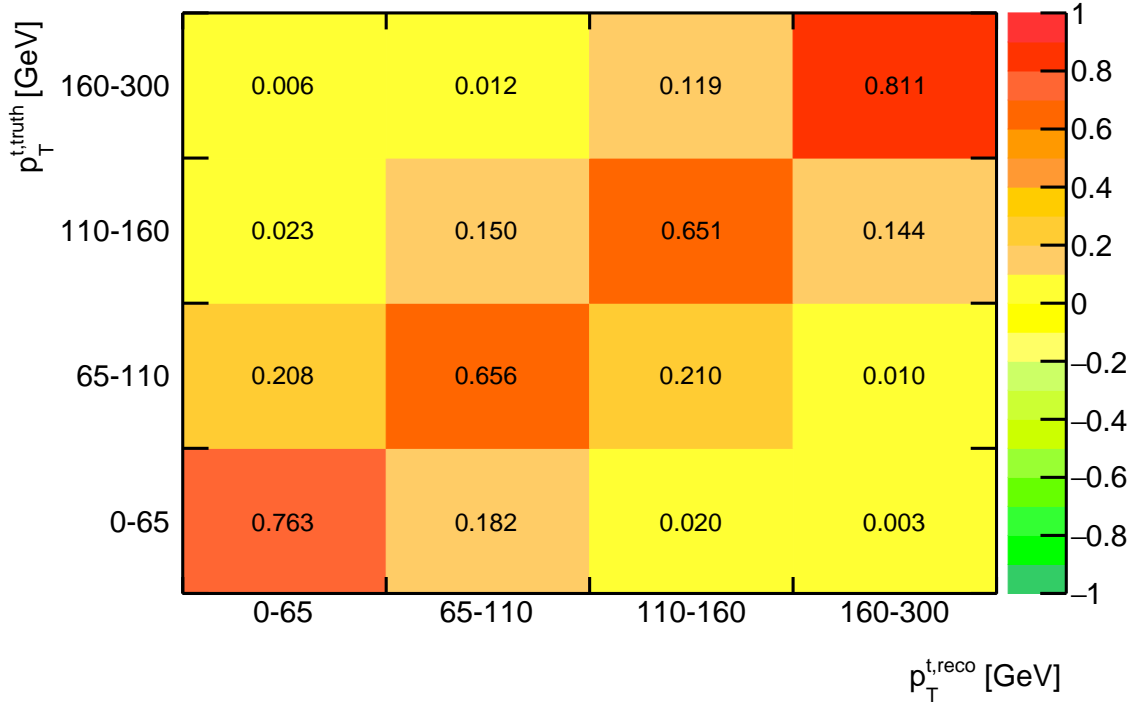
Figure 6.5: Migration matrix for $p_T(t)$

6.2 Validation tests

In order to check if the unfolding framework performs as expected, few validation tests were performed using MC samples. The tests are described in the following section. The resulting distributions accompanied by statistical uncertainties are provided for $p_T(W)$ and $p_T(t)$ variables.

6.2.1 Consistency Test

In a consistency test, the unfolding requirements ϵ, a and M are computed from the whole MC sample. Afterwards, these are used to unfold the same MC sample. The unfolded distribution is expected to completely match with the truth distribution. This is achieved in cases of $p_T(W)$ and $p_T(t)$ unfolding. The normalisation factors shown in Figure 6.6 and Figure 6.7, have a value of 1 for all bins along with statistical uncertainties. The unfolded distributions are shown in Figure 6.8 and Figure 6.9. Moreover, the level of agreement between unfolded MC sample and the truth distribution is visible from the parameter of interest values (signal strength) shown in Table 6.1 and Table 6.2.

6.2.2 Pseudo experiments

In order to check whether the uncertainties estimated in profile likelihood unfolding are correct, pseudo experiments are performed. A set of 10 000 toys are generated by fluctuating the nominal
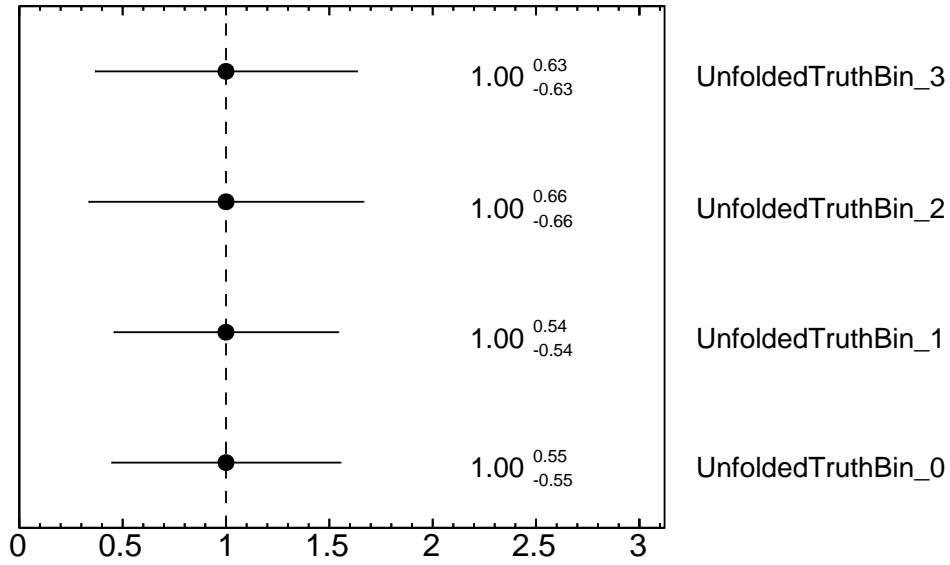
Figure 6.6: Normalisation factors for $p_T(W)$
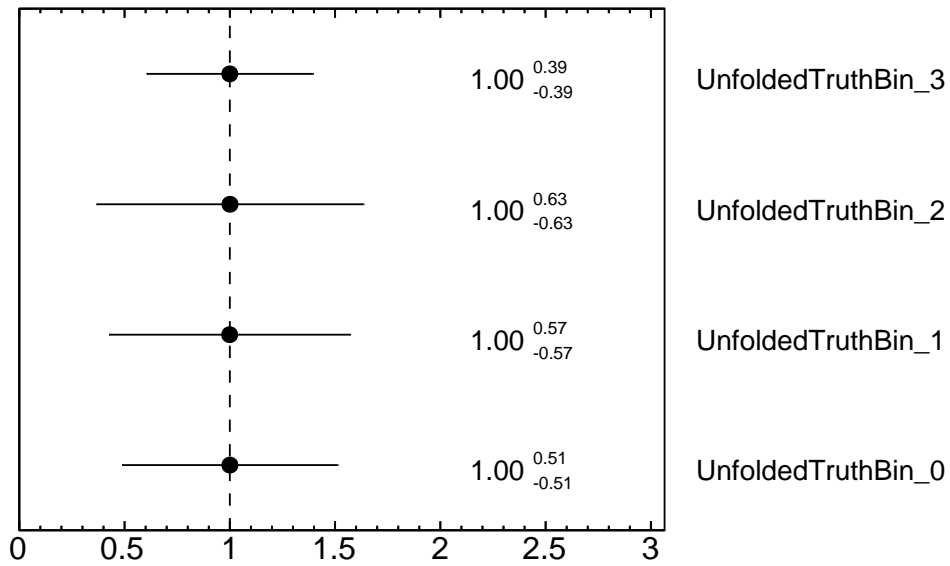
Figure 6.7: Normalisation factors for $p_T(t)$

(a) Unfolded distribution of $p_T(W)$ (b) Unfolded distribution of $p_T(t)$
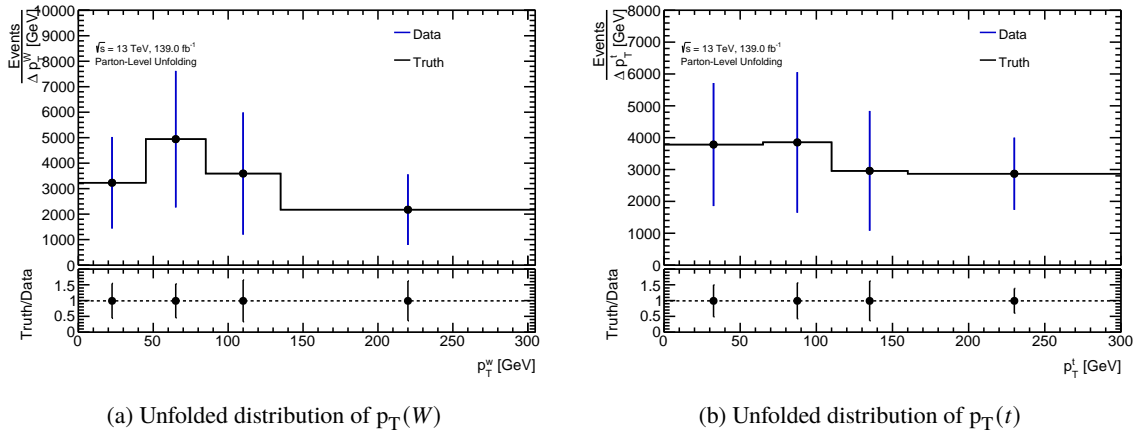
Figure 6.8: Distributions of unfolded number of events obtained from PLU

(a) Differential cross-section for $p_T(W)$ (b) Differential cross-section for $p_T(t)$
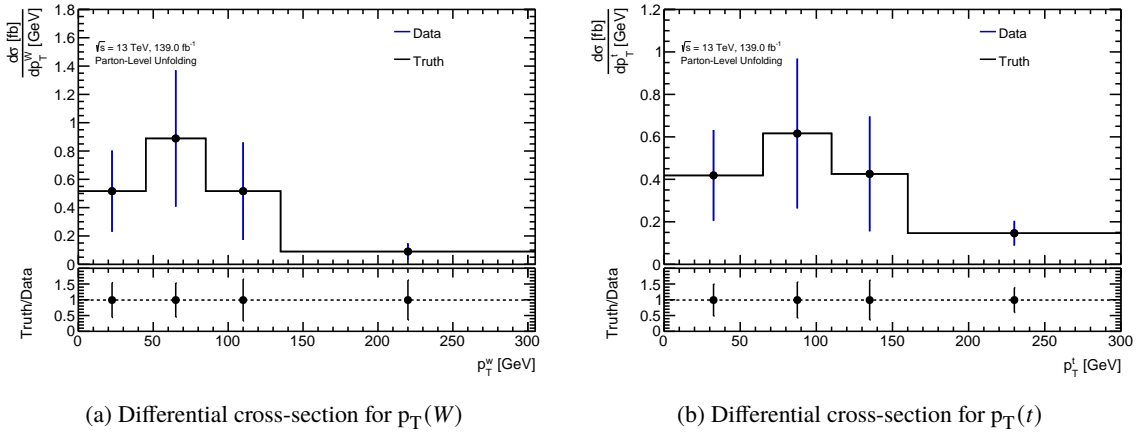
Figure 6.9: Unfolded differential cross-sections obtained after applying profile likelihood unfolding

MC sample within its expected statistical uncertainty. All these toys are unfolded. Furthermore, the resulting parameter values are fitted as shown in Figure 6.10 and Figure 6.11. It was observed that the values for each bin follow a Gaussian distribution. The mean and standard deviation of these Gaussian distributions, for both the variables are summarised in Table 6.3 and Table 6.4. By comparing Table 6.1 and Table 6.3, it is observed that the standard deviation of the parameter values (for $p_T(W)$) is consistent with its uncertainty given by the fit. Similar observation can be made in case of $p_T(t)$ by comparing Table 6.2 and Table 6.4. Therefore, the uncertainties in parameter values are correctly estimated in profile likelihood unfolding.

6.2.3 Pull test

In statistics, if x is a random variable with mean m[1] and standard deviation s then the distribution of $Z = (x - m)/s$ is supposed to follow a standard normal distribution; i.e, with mean zero and width

---

[1] Here m is used to denote the mean instead of the general denotation μ because μ is used for POI

Bins	μ
1	1.00 ± 0.55
2	0.99 ± 0.54
3	1.00 ± 0.66
4	0.99 ± 0.63

Table 6.1: Signal strength values for $p_T(W)$

Bins	μ
1	1.00 ± 0.51
2	0.99 ± 0.57
3	1.00 ± 0.63
4	0.99 ± 0.40

Table 6.2: Signal strength values for $p_T(t)$

Bins	Mean	Standard deviation
1	1.01	0.55
2	0.99	0.54
3	1.00	0.66
4	1.00	0.62

Table 6.3: Summary of mean and standard deviation from the toys for $p_T(W)$

Bins	Mean	Standard deviation
1	1.00	0.50
2	1.00	0.56
3	1.00	0.62
4	0.99	0.39

Table 6.4: Summary of mean and standard deviation from the toys for $p_T(t)$

one. In problems of parameter estimation, this property is used to check if the errors estimated by the fit are correct. Interpreting the parameter obtained from the fit as a random variable, its values from the pseudo experiments are used to perform a pull test. Consider an observation in bin i, $\mu_{\text{fitted}}^{n,i}$, where $1 < n <$ number of toys. A quantity termed as *pull*, $p_{n,i}$ is computed as

$$p_{n,i} = \frac{\mu_{\text{fitted}}^{n,i} - \mu_{\text{exp}}}{\sigma_{\text{fitted}}^{i}}. \tag{6.1}$$

Here, μ_{exp} is the expected POI, i.e 1 and $\sigma_{\text{fitted}}^{i}$ is the standard deviation of the observations in bin i. For each bin, a normal distribution is fitted on the computed pulls. Figure 6.12 and Figure 6.13 show the mean and standard deviation of the fitted distribution of pulls. The mean is close to 0 and standard deviation is close to 1. Thus, validating the statistical uncertainties estimated by the fit. A detailed explanation of a pull test can be found in [68]. If the standard deviation of the pull plot is greater (smaller) than 1, it means the errors are under (over) estimated [56]. This effect is observed when pull test is performed on regularised distributions (refer to Appendix B.2).

(a) Toy distribution for bin 1

(b) Toy distribution for bin 2

(c) Toy distribution for bin 3

(d) Toy distribution for bin 4
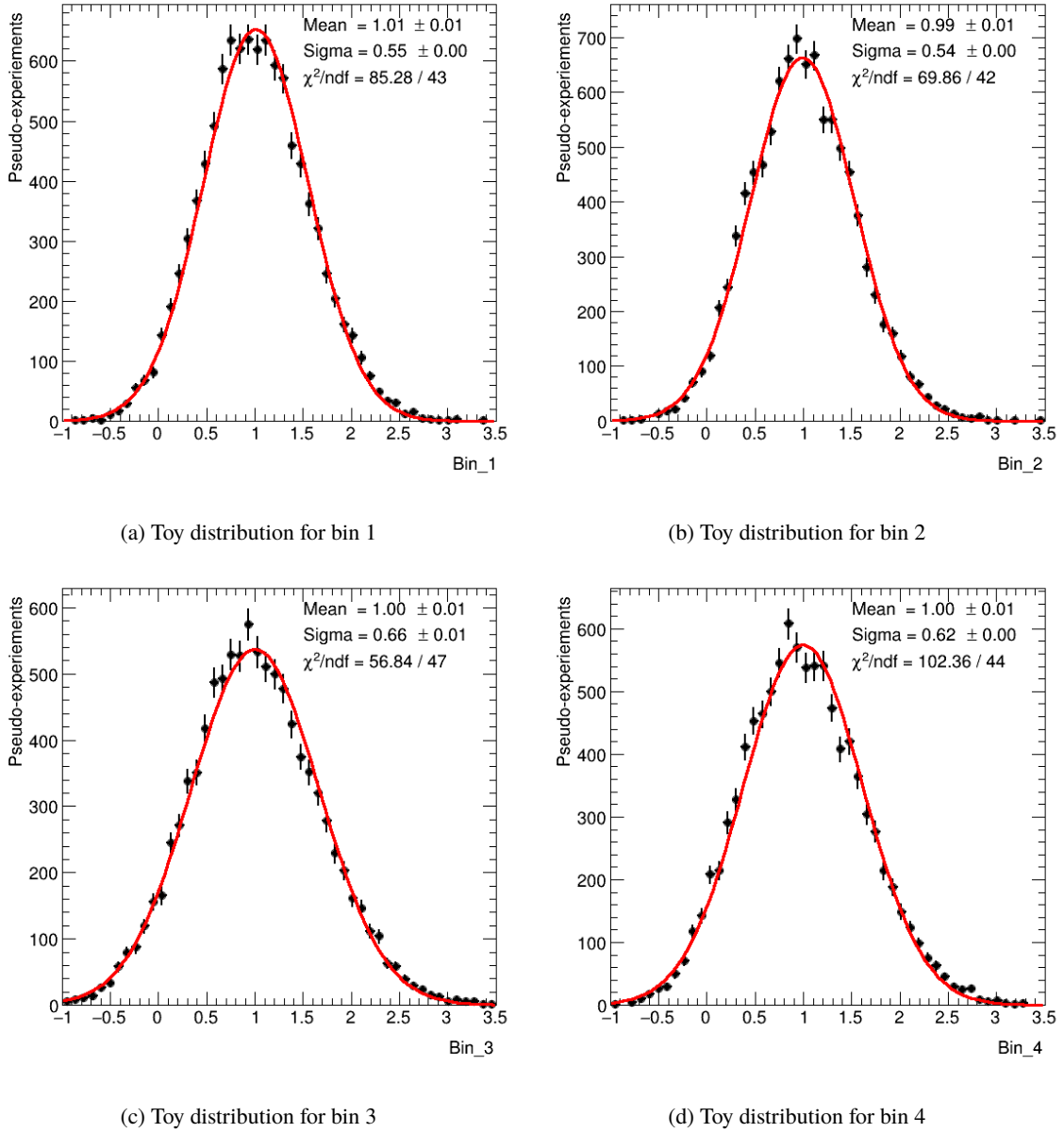
Figure 6.10: Toy distributions of all bins for $p_T(W)$

6.3 Unfolding Data

The outcomes of the validation tests proved that the framework is trustworthy. Hence, unfolding of the actual data samples was performed. Unfolded distributions of $p_T(W)$ and $p_T(t)$ with statistical uncertainties are presented. Results obtained after including regularisation (as explained in Section 5.2.3) in the process of unfolding, are shown in Section 6.3.3.

(a) Toy distribution for bin 1

(b) Toy distribution for bin 2

(c) Toy distribution for bin 3

(d) Toy distribution for bin 4
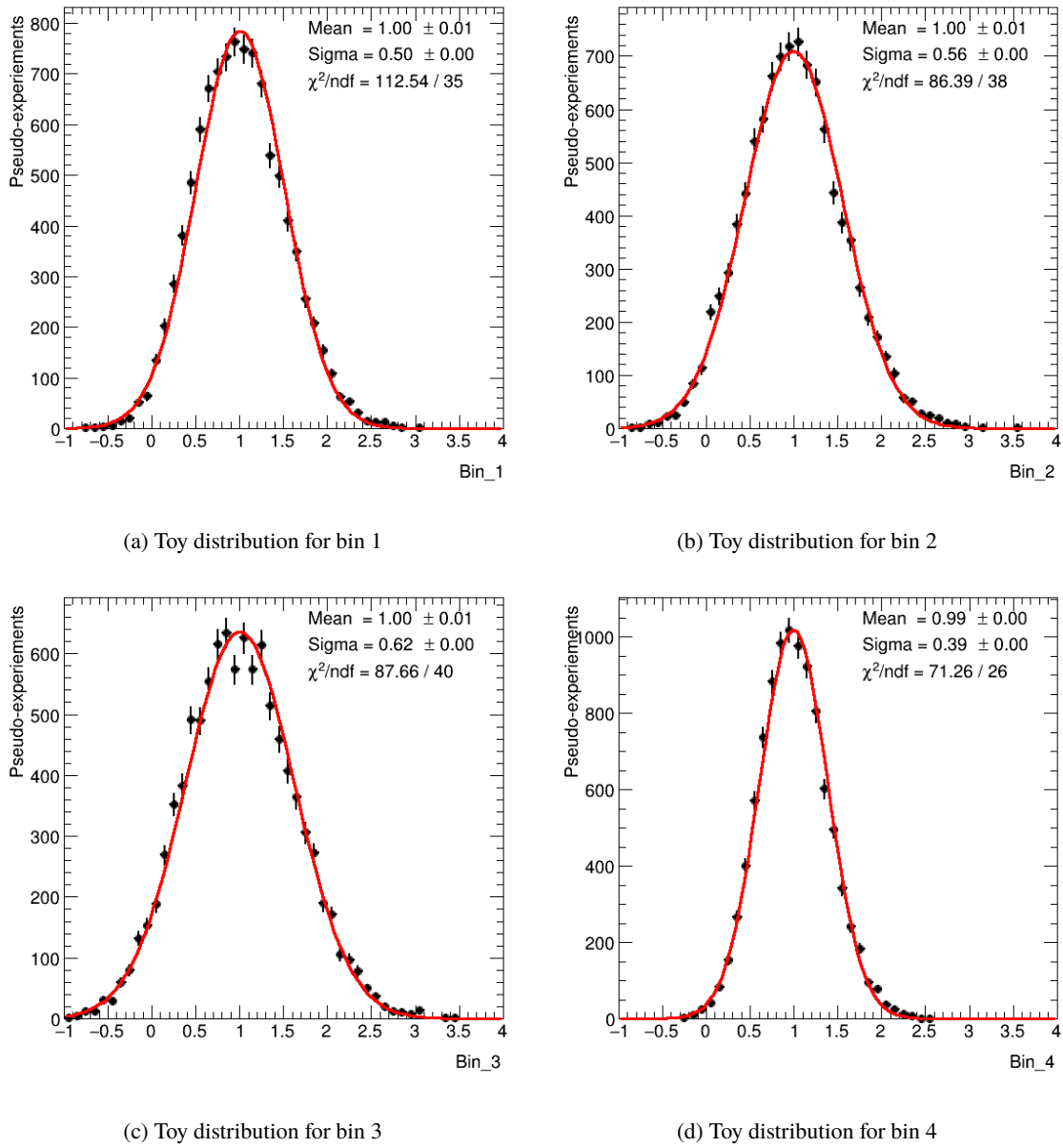
Figure 6.11: Toy distributions of all bins for $p_T(t)$

6.3.1 W-boson p_T

Unfolded distributions of differential cross-sections obtained for $p_T(W)$ are shown in Figure 6.14. The normalisation factors are shown in Figure 6.16. An overview of the differential cross-sections in each individual bin and the best-fit values of signal strength (μ) is given in Table 6.5.
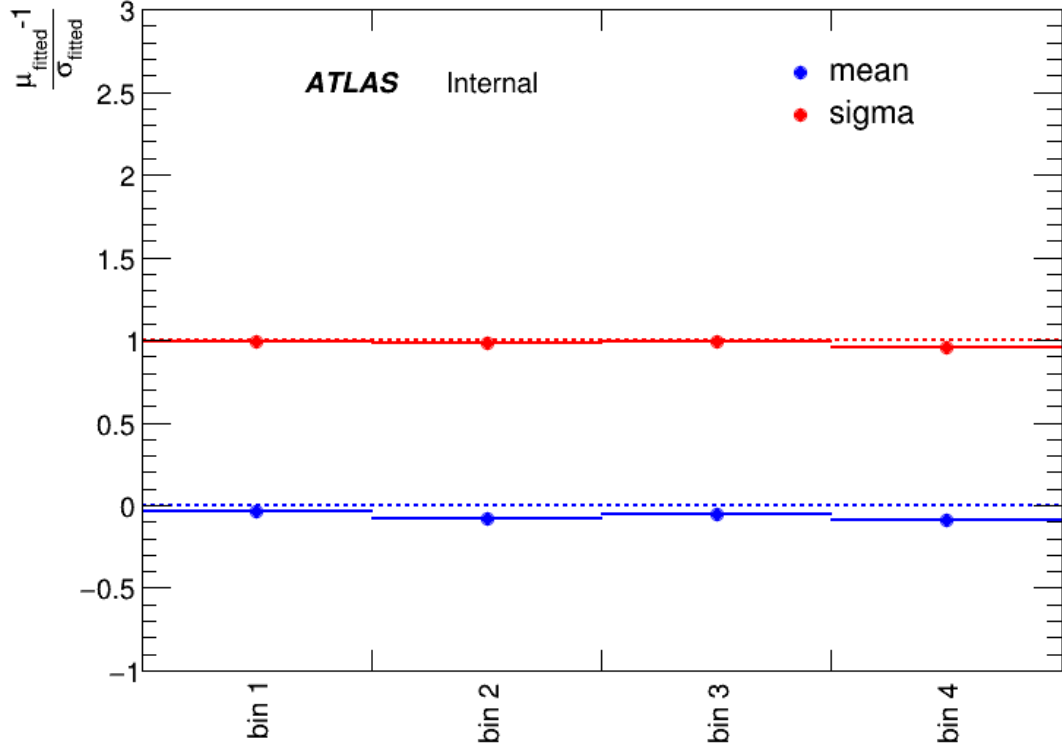
Figure 6.12: Mean and standard deviation of distribution of pulls for every bin in case of $p_T(W)$

$p_T(W)$[GeV]	$\frac{\mathrm{d}\sigma}{\mathrm{dp_T}(W)}$[fb/GeV]	$\frac{1}{\sigma}\frac{\mathrm{d}\sigma}{\mathrm{dp_T}(W)}[10^{-3}/\mathrm{GeV}]$	μ
0-45	0.35 ± 0.29	3.62 ± 3.08	1.01 ± 0.54
45-85	1.33 ± 0.45	13.7 ± 4.67	0.82 ± 0.51
85-135	0.19 ± 0.26	1.92 ± 2.75	1.75 ± 0.63
135-305	0.11 ± 0.04	1.12 ± 0.47	1.72 ± 0.72

Table 6.5: Overview of the individual bin contents of the differential and normalised differential cross-sections
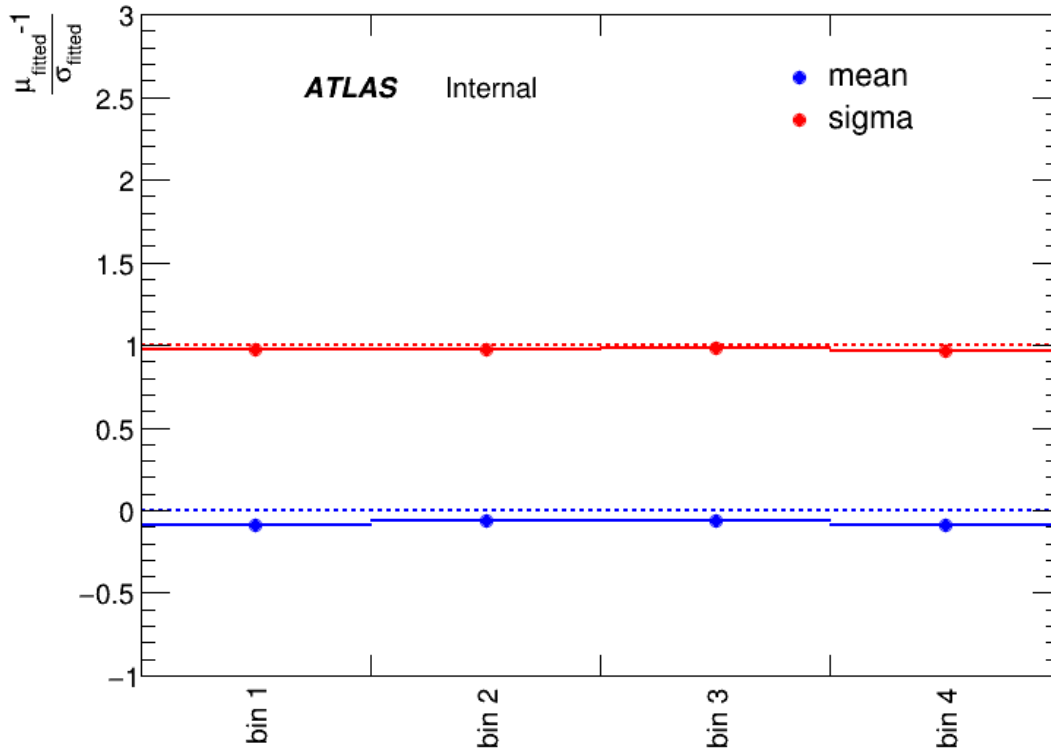
Figure 6.13: Mean and standard deviation of distribution of pulls for every bin in case of $p_T(t)$

$p_T(t)$[GeV]	$\frac{d\sigma}{dp_T(t)}$[fb/GeV]	$\frac{1}{\sigma}\frac{d\sigma}{dp_T(t)}[10^{-3}/\text{GeV}]$	μ
0-65	0.25 ± 0.21	2.51 ± 2.13	0.58 ± 0.49
65-110	1.18 ± 0.40	12.2 ± 4.15	1.92 ± 0.65
110-160	0.19 ± 0.27	1.92 ± 2.75	0.44 ± 0.62
160-300	0.13 ± 0.05	1.36 ± 0.58	0.89 ± 0.38

Table 6.6: Overview of the individual bin contents of the differential and normalised differential cross-sections

6.3.2 Top-quark p_T

Differential cross-sections obtained for $p_T(t)$ are shown in Figure 6.15. The normalisation factors are shown in Figure 6.17. An overview of the differential cross-sections in each individual bin and the best-fit values of signal strength (μ) is given in Table 6.6.

6.3.3 Regularised results

Regularisation is allowed in the unfolding procedure. Results for $\tau = 1$ and $\tau = 1.5$ are shown in Figure 6.18 and Figure 6.19 respectively. On applying regularisation, the errors are reduced
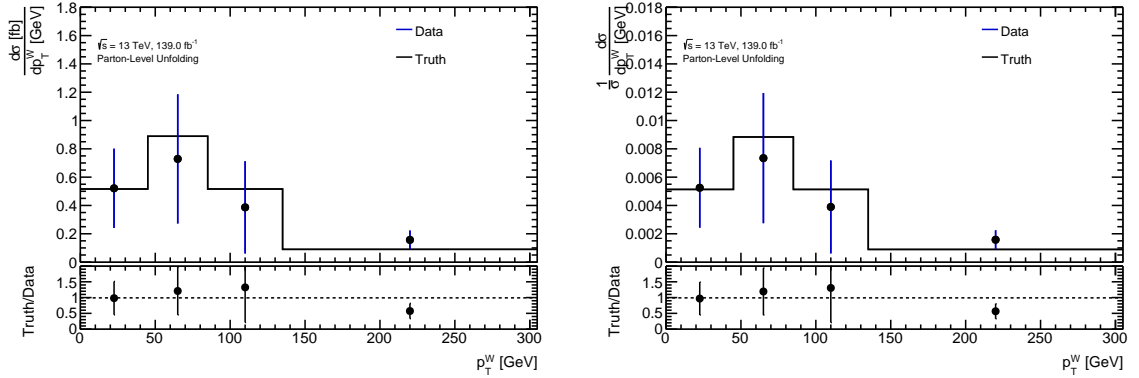
Figure 6.14: Unfolded distributions of $p_T(W)$
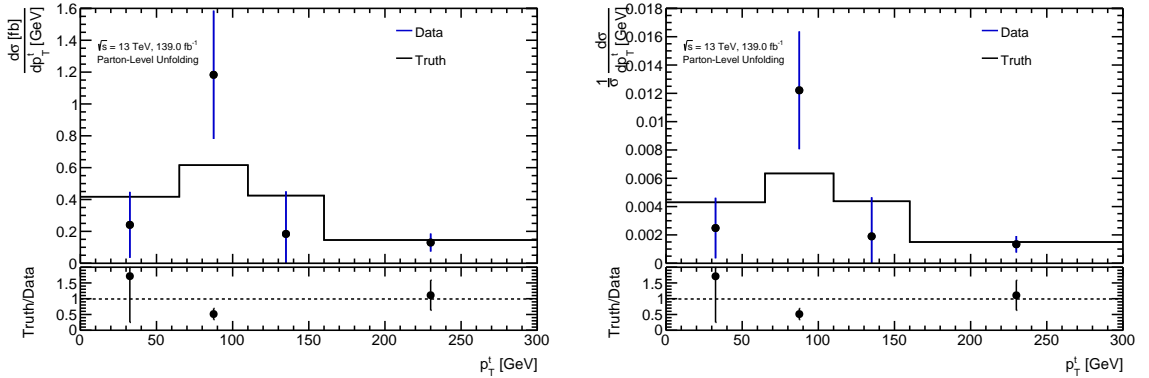
Figure 6.15: Unfolded distributions of $p_T(t)$

compared to the non regularised case. The values of normalisation factors are shown in Figure 6.20 and Figure 6.21. By comparing these values to Figure 6.16 and Figure 6.17, a reduction in statistical uncertainty of the values is noticed. In addition to that, normalisation factors approach to one as the value of τ increase. The results obtained after applying regularisation on MC sample of $p_T(W)$ are presented in Appendix B.

6.3.4 Correlation matrices

Matrices quantifying correlations between different bins were computed for iterative Bayesian and profile likelihood unfolding. In case of IBU, a bootstrap method as described in Section 5.3 was implemented. In order to compare the correlations obtained from IBU, an inbuilt method of the `RooUnfold` class was employed for calculating a correlation matrix. This method is named `Ereco(kCovToy)`. By selecting the option `kCovToy`, matrix is computed internally using toy experiments. In case of PLU, the correlation matrix is computed from the covariance matrix generated by Minuit processors. Correlation matrices for PLU are shown in Figure 6.22 while matrices associated with IBU are shown in Figure 6.25 and Figure 6.26.

The construction of iterative Bayesian and profile likelihood unfolding methods, allow bin correl-
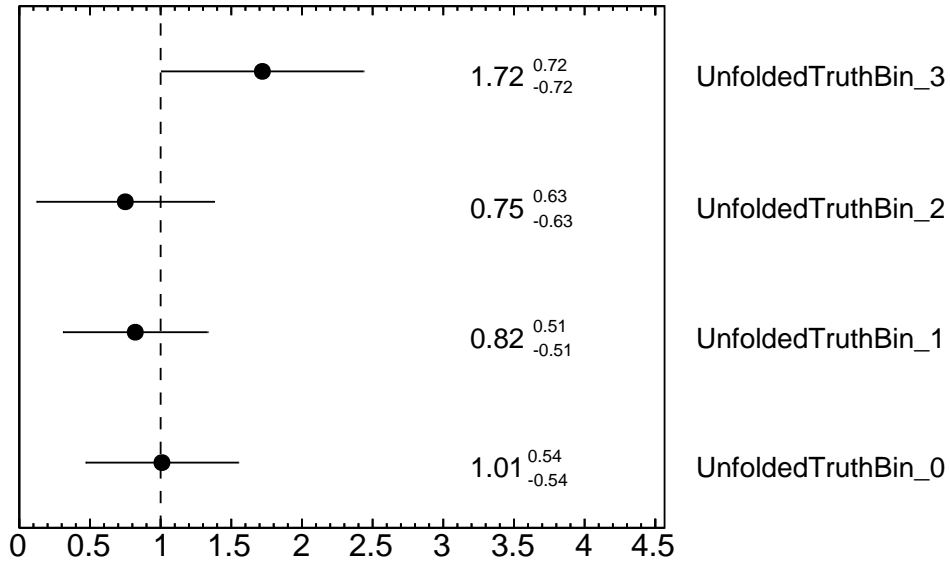
Figure 6.16: Normalisation factors for $p_T(W)$
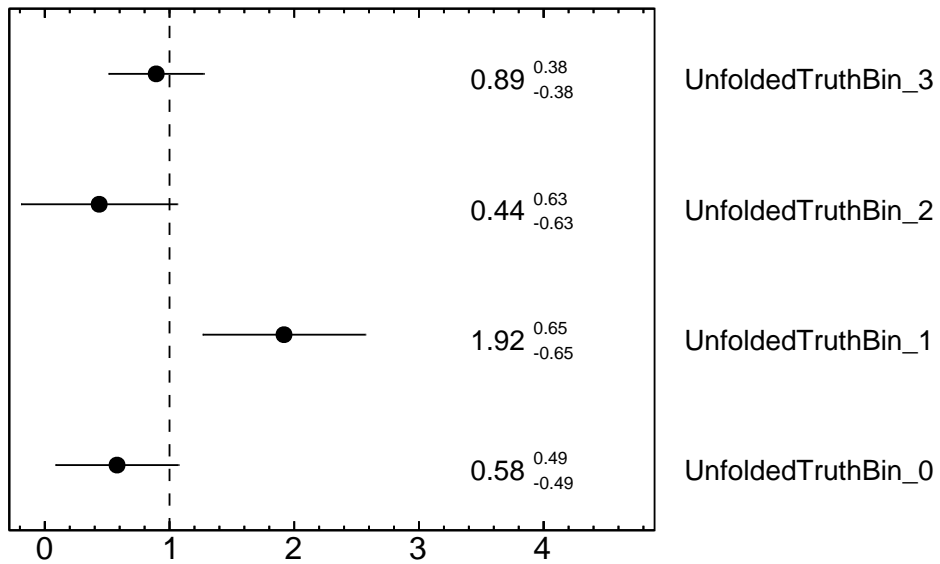
Figure 6.17: Normalisation factors for $p_T(t)$

(a) Regularised result for $p_T(W)$

(b) Regularised result for $p_T(t)$
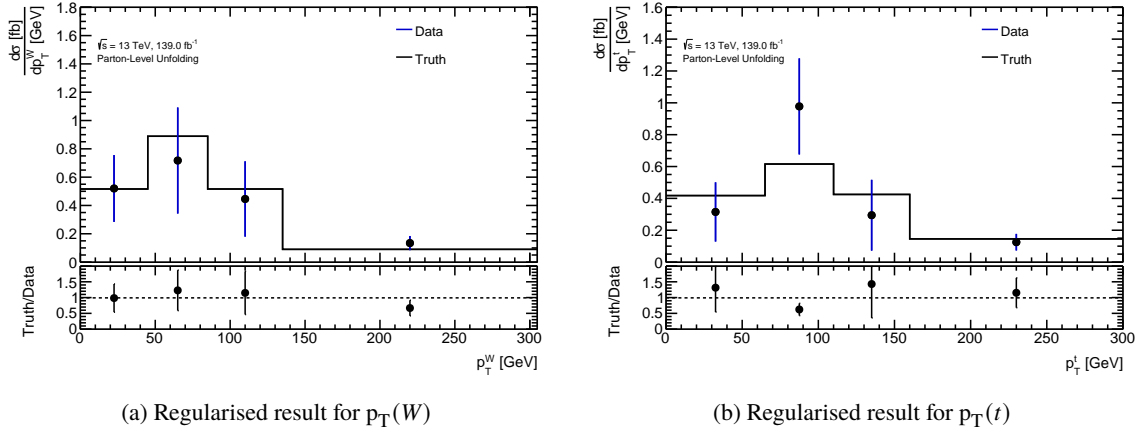
Figure 6.18: Regularised unfolded distributions in case of $\tau = 1$

(a) Regularised result for $p_T(W)$

(b) Regularised result for $p_T(t)$
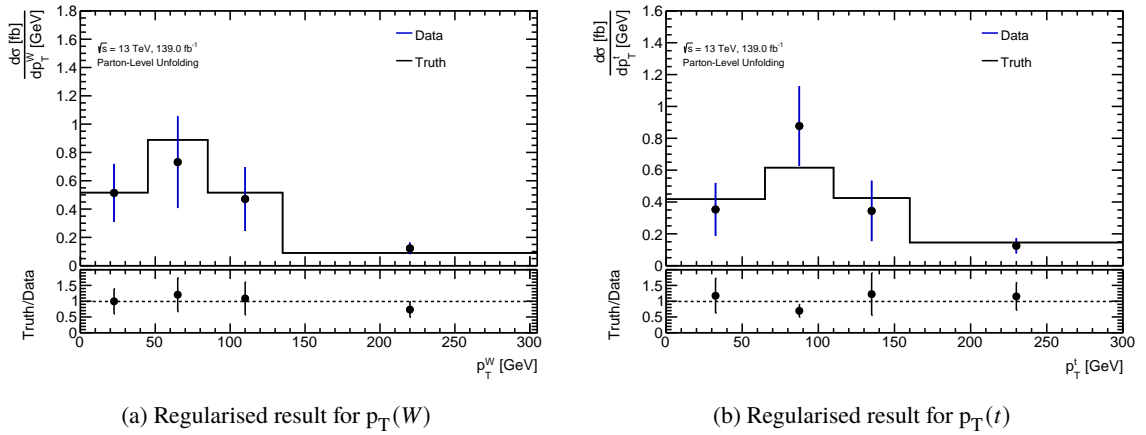
Figure 6.19: Regularised unfolded distributions in case of $\tau = 1.5$

ations in the unfolded distributions. Bin-by-bin unfolding does not consider bin correlations. For IBU, the bootstrap method yields large positive correlations whereas the Ereco(kCovToy) method provides small and negative correlations. An alternative method of generating toy experiments and computing correlations using them, was implemented in [66] and the results are similar to that from the bootstrap method. In order to validate the bootstrap method, it was applied to bin-by-bin unfolding. Expected negligible values appear in the correlation matrix as shown in Figure 6.27 and Figure 6.28. On the other hand, unfolded bins are negatively correlated in case of PLU. Furthermore, correlations decrease after applying regularisation. This effect can be observed by comparing Figure 6.22 with Figures 6.23 and 6.24.

6.3.5 Systematic uncertainties

Uncertainties associated with background modelling are included in the $p_T(W)$ MC sample. Main backgrounds in the tZq production are described in Section 4.2. Uncertainties associated with each background process is taken from [1]. The diboson contribution is split into heavy flavour (VV+HF)

(a) Regularised result for $p_T(W)$

(b) Regularised result for $p_T(t)$
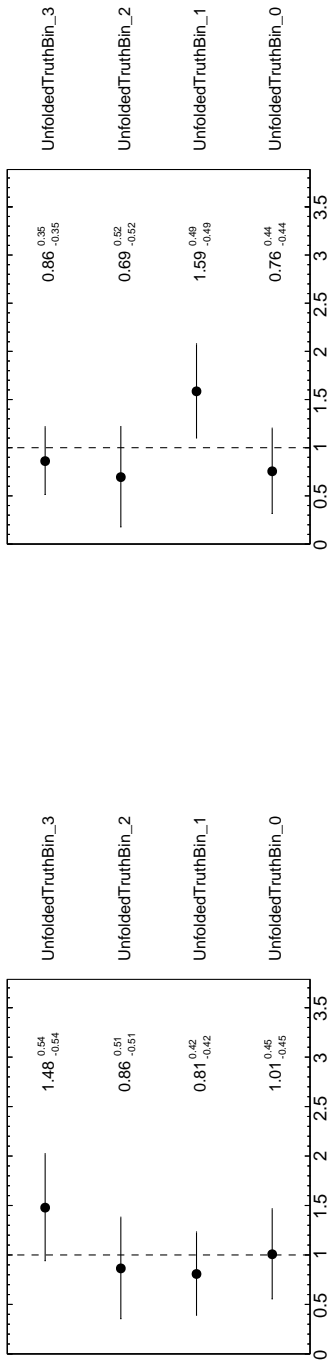
Figure 6.20: Regularised normalisation factors in case of $\tau = 1$

(a) Regularised result for $p_T(W)$

(b) Regularised result for $p_T(t)$
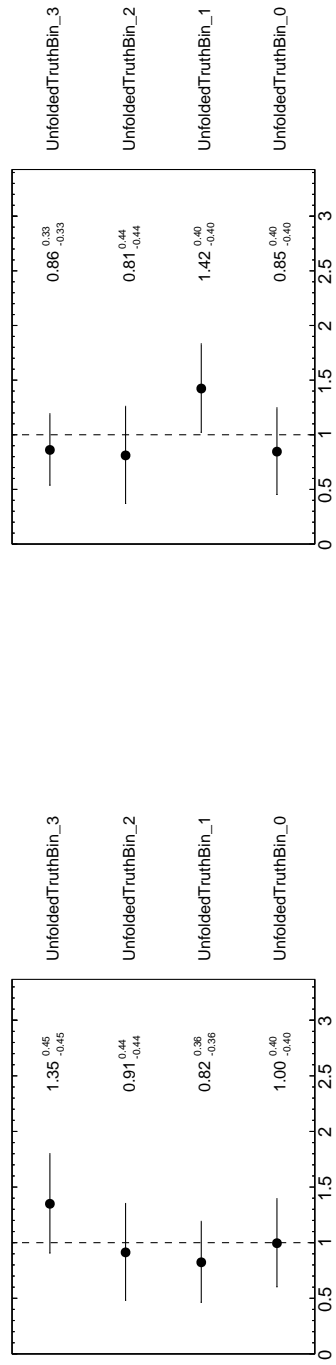
Figure 6.21: Regularised normalisation factors in case of $\tau = 1.5$

65

(a) Correlation matrix for $p_T(W)$

(b) Correlation matrix for $p_T(t)$
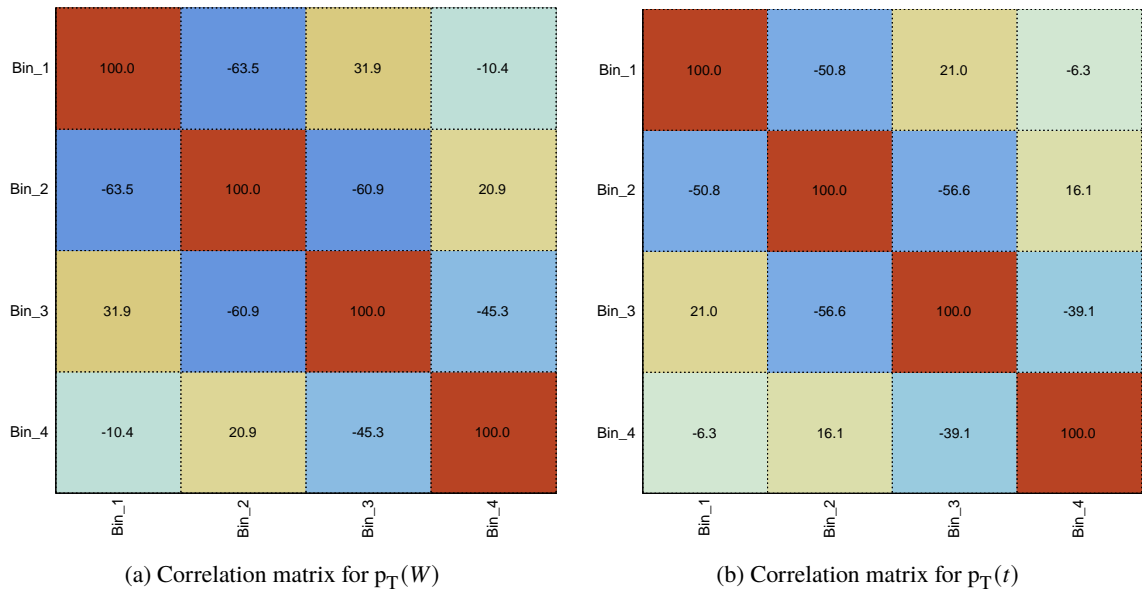
Figure 6.22: Correlation matrices (in %) obtained from profile likelihood unfolding ($\tau = 0$)

(a) Correlation matrix for $p_T(W)$

(b) Correlation matrix for $p_T(t)$
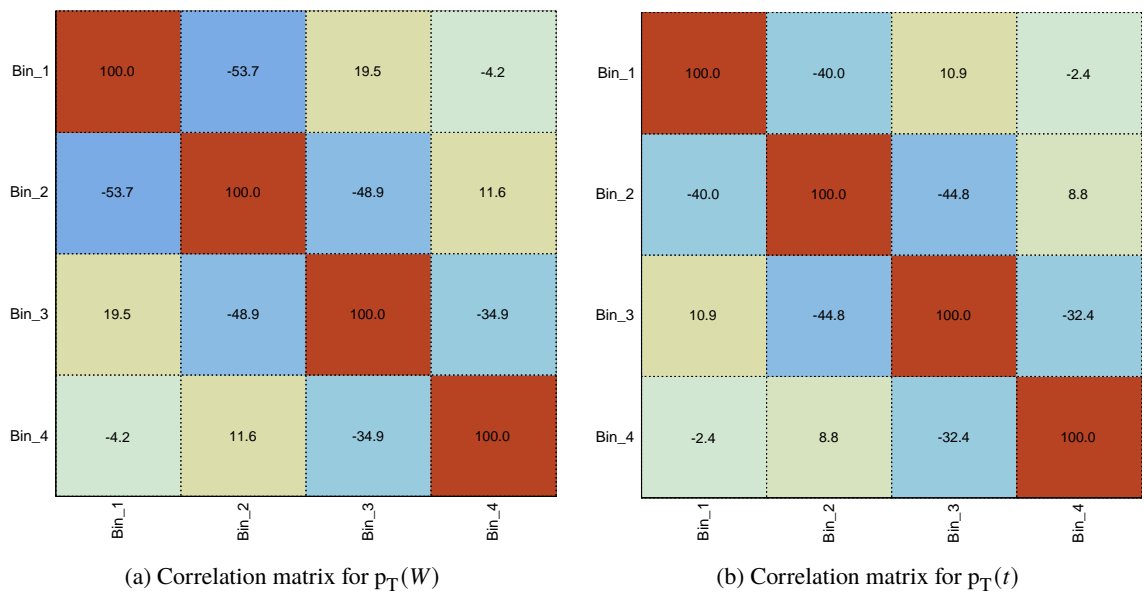
Figure 6.23: Correlation matrices (in %) obtained from profile likelihood unfolding ($\tau = 1$)

(a) Correlation matrix for $p_T(W)$

(b) Correlation matrix for $p_T(t)$
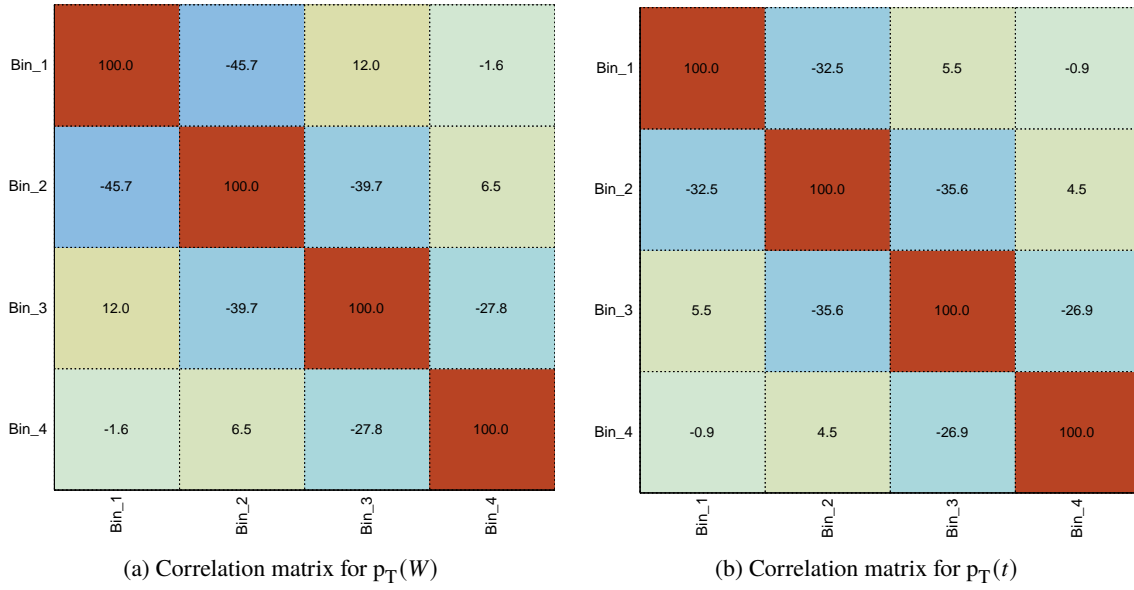
Figure 6.24: Correlation matrices (in %) obtained from profile likelihood unfolding ($\tau = 1.5$)

and light flavour (VV+LF) according to the origin of associated jets. Diboson events having b and c jets are included in heavy flavour group. Uncertainty in VV+HF events is 30 % and that in VV+LF is 20 %. Contribution from $t\bar{t}W$ and $t\bar{t}H$ are combined because their contribution is small. The uncertainty associated with them is 15 %. The uncertainty for backgrounds $t\bar{t}Z$ and tWZ (combined) is 12 %. For unconstrained backgrounds namely Z+jets and $t\bar{t} + tW$, an uncertainty of 15 % and 7 % is included respectively.

The effect of a nuisance parameter on the signal strength (μ) is shown in the ranking plot in Figure 6.29. Nuisance parameters (θ) associated with all the included systematics are ranked as per their impact. The impact ($\Delta\mu$) is defined as the shift in μ when the nuisance parameter is deviated in both directions ($\hat{\theta} \pm \Delta\hat{\theta}$), where $\hat{\theta}$ is the best-fit value of a nuisance parameter and $\Delta\hat{\theta}$ is its uncertainty. The empty boxes in the ranking plot show pre-fit impact while the coloured boxes show the post-fit impact. The post-fit impact is smaller than the pre-fit impact when the parameters are constrained by the fit. The lower axis of the ranking plot describes the nuisance parameter pull. It is defined as a ratio of the difference between best-fit value and pre-fit value (θ_0) of a nuisance parameter to the pre-fit uncertainty ($\Delta\theta$). More information about the ranking plot is given in [69].

6.3.6 Comparison of unfolding methods

A brief comparison of the unfolded differential cross-sections obtained from profile likelihood unfolding is done with the results obtained from iterative Bayesian and bin-by-bin unfolding. Only statistical uncertainties are included for all the three methods. Figure 6.30 shows unfolded $p_T(t)$ distribution after iterative Bayesian (with 3 iterations) and bin-by-bin unfolding is performed. Both these methods were implemented in a previous thesis [66].

By comparing IBU and BBB results with that from PLU (refer to Figure 6.15), it is observed that the statistical error in IBU and BBB is small compared to PLU. Although, the regularised distribution (refer to Figure 6.19) show a similar uncertainty. Here, it is important to note the bin correlations are
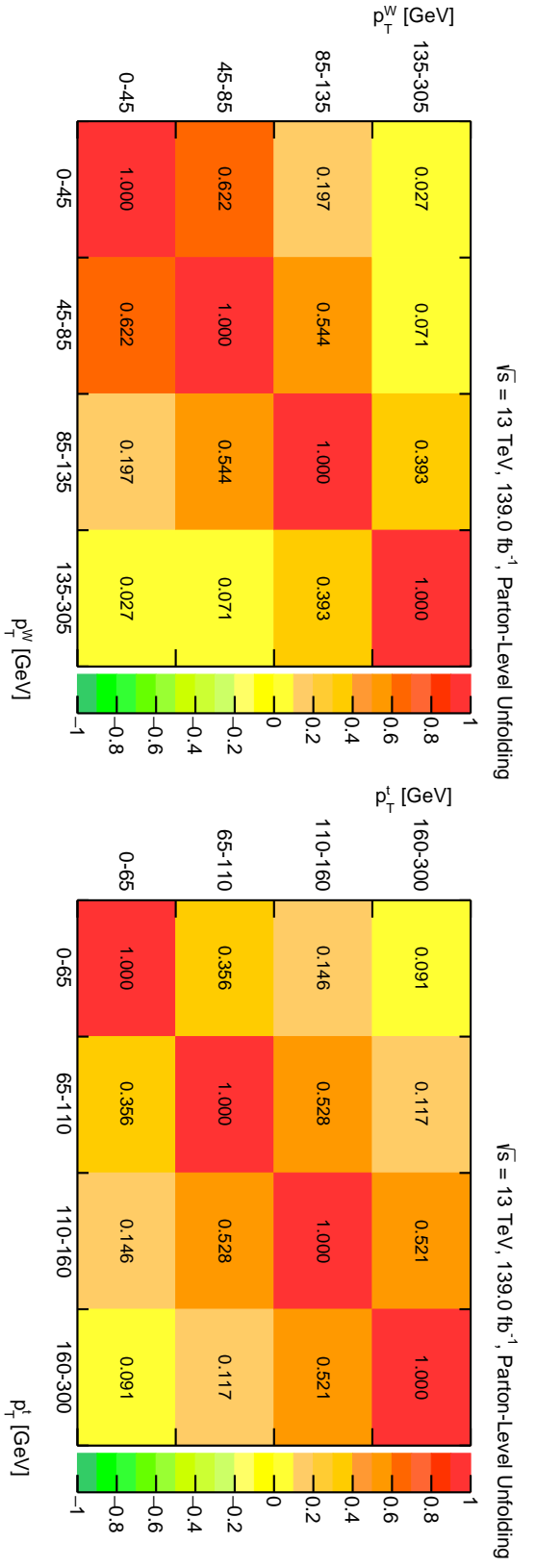
(a) Correlation matrix for $p_T(W)$

(b) Correlation matrix for $p_T(t)$

Figure 6.25: Correlation matrices in case of IBU obtained using bootstrap method
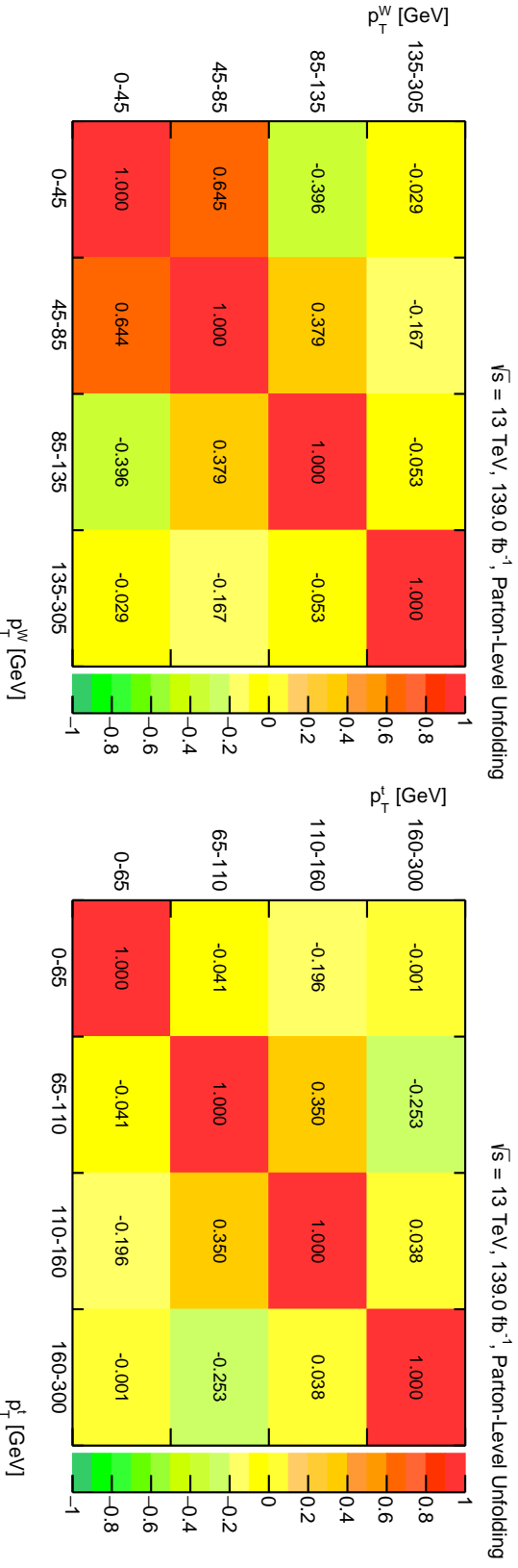
(a) Correlation matrix for $p_T(W)$

(b) Correlation matrix for $p_T(t)$

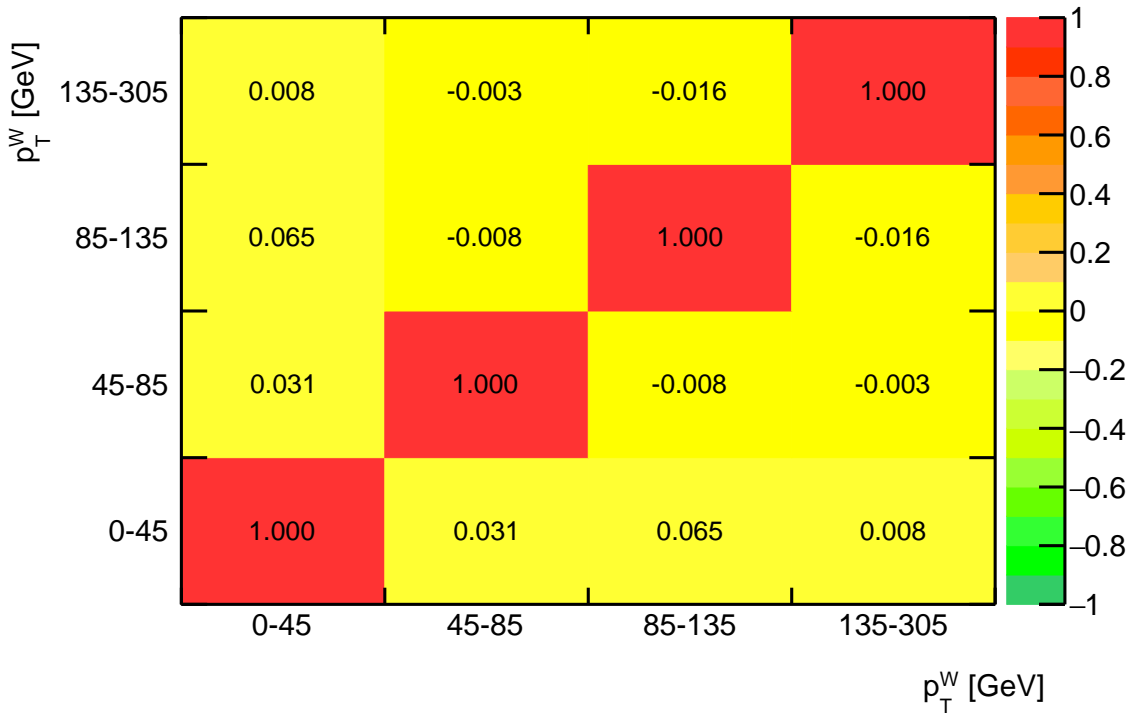Figure 6.26: Correlation matrices in case of IBU obtained from RooUnfold

Figure 6.27: Correlation matrix for $p_T(W)$ in bin-by-bin unfolding

excluded from the IBU results. Standard deviations in case of iterative Bayesian are observed to be between 20 % to 39 % while for bin-by-bin it is between 22 % to 60 %. Profile likelihood unfolded results have standard deviations between 60 % to 75 % including bin correlations. A comparison between the correlation matrices calculated for these methods is discussed in Section 6.3.4. Due to time constraint, a robust comparison could not be carried out for all the three methods.
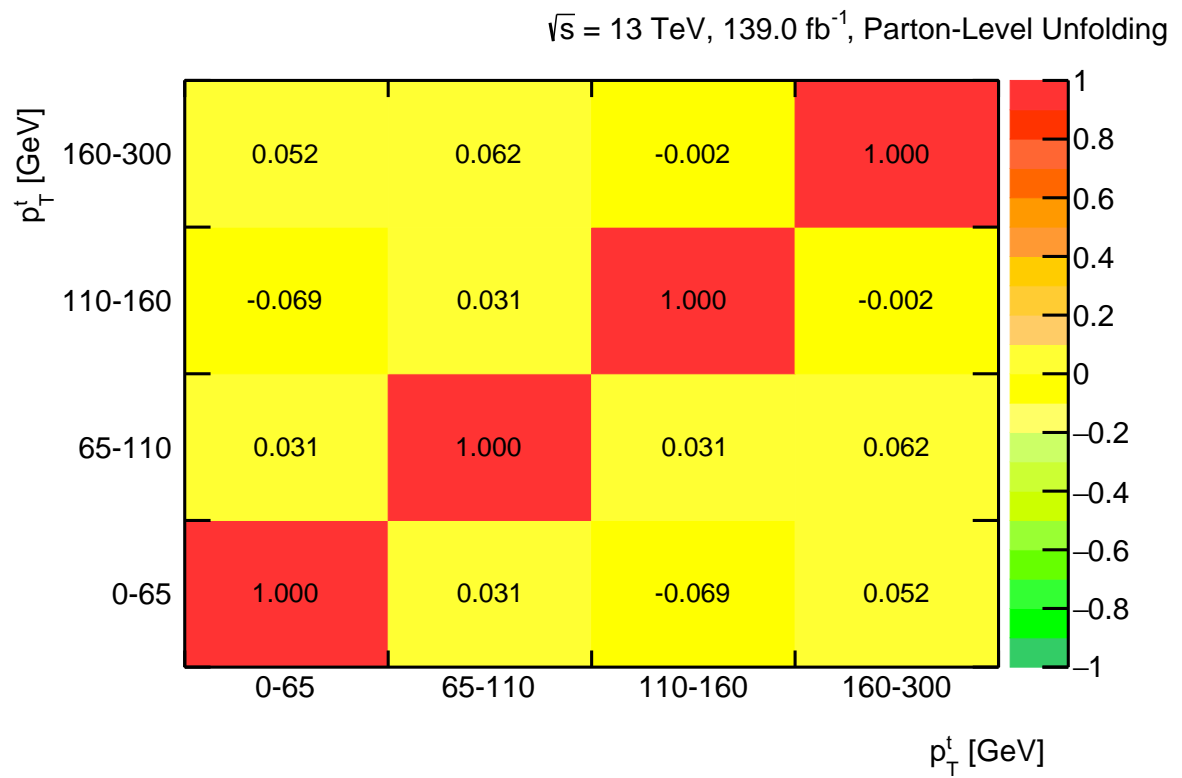
Figure 6.28: Correlation matrix for $p_T(t)$ in bin-by-bin unfolding
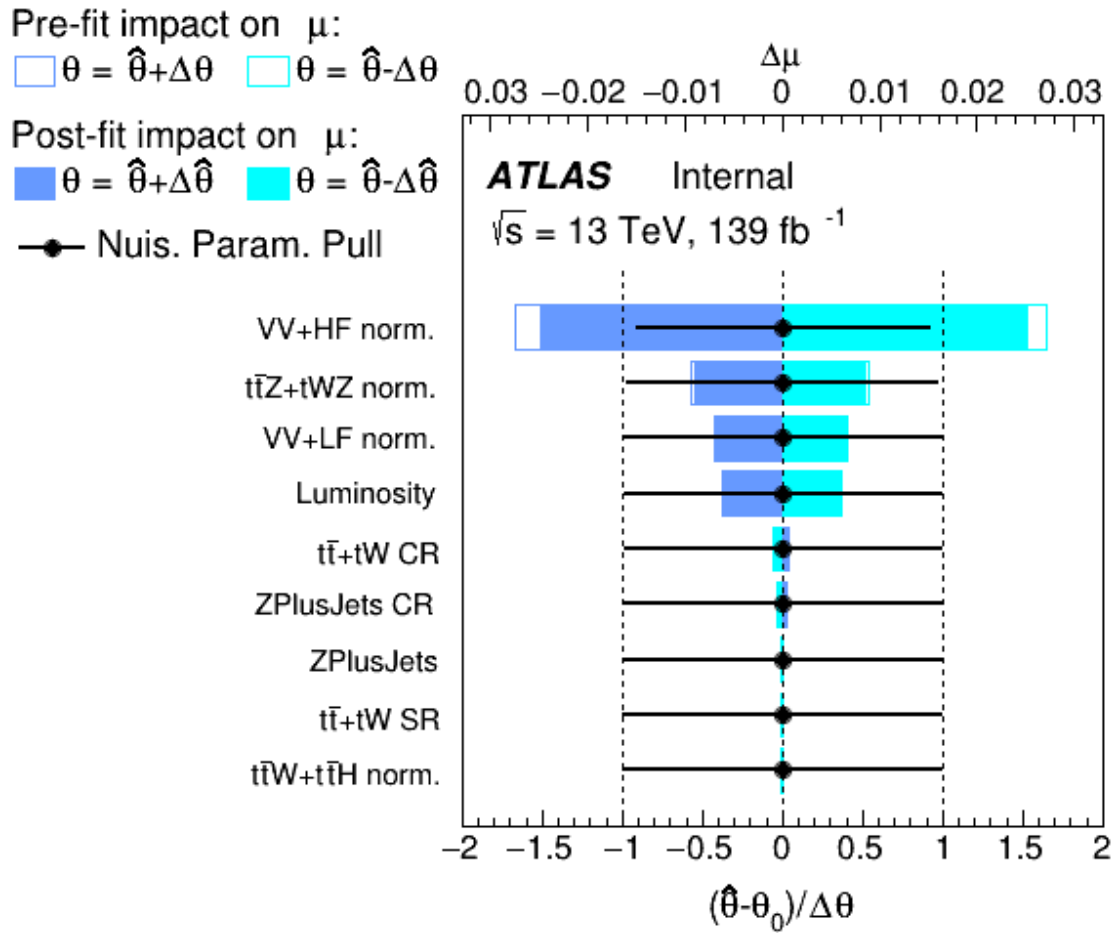
Figure 6.29: Ranking plot for all included systematics
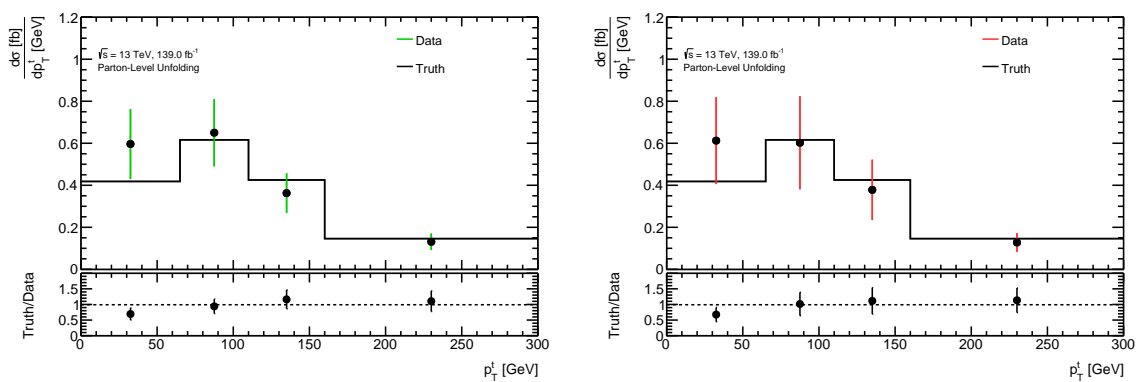
(a) Iterative Bayesian unfolded $p_T(t)$ distribution

(b) Bin-by-bin unfolded $p_T(t)$ distribution

Figure 6.30: Unfolded distributions for IBU and BBB

Conclusion

7.1 Summary

This thesis presents the differential cross-section measurements of the associated production of a single top-quark with a Z-boson, known as the tZq process. The data analysed in this work corresponds to an integrated luminosity of $139\,\text{fb}^{-1}$ recorded by the ATLAS detector during Run-2 (2015-2018) of the LHC. The tZq process is studied in the trilepton channel. The differential cross-sections are measured as a function of p_T of the top-quark and p_T of the W-boson decaying from it.

Unfolding is implemented to estimate the true distribution from the distorted observed distribution. This is the first time where profile likelihood unfolding is used for measurement of differential cross-sections. Other unfolding methods including iterative Bayesian and bin-by-bin were used in a previous thesis [66]. A brief comparison is done for all the three methods. Correlation matrices for iterative Bayesian unfolding are calculated using a bootstrap method. In addition to that, a built-in method of the `RooUnfold` class is also used for the same purpose.

Profile likelihood unfolding is implemented using `TRExFitter`. Unfolding requirements such as efficiency, acceptance and migration matrix are calculated using optimal binning. In order to make sure that the profile likelihood model is robust, few validation tests are performed. From these tests, it is inferred that the model correctly estimates the uncertainties. Statistical uncertainties for PLU are observed to be between $60\,\%$ to $75\,\%$ including bin correlations. One of the reasons for this is the low statistics of the tZq process. Normalised distributions are also computed.

In order to damp amplifications of statistical fluctuations caused during the unfolding process, regularisation is included. This resulted into a decrease in the statistical uncertainties of the unfolded distributions. Profile likelihood unfolding allows the inclusion of systematic uncertainties in a simple way. This is one of the reasons why this method was implemented. Systematic uncertainties related to background modelling are included in the MC sample. These uncertainties are caused due to the MC generators used to determine background events. Effect of each systematic on the parameter of interest is determined from the ranking plot. The measured differential cross-sections for both variables are in agreement with the Standard Model predictions.

7.1.1 Future Aspects

Differential cross-section measurement of the tZq process can be improved in a number of possible ways. Some of the ways are discussed below:

- In this work, only variables related to the top-quark were unfolded. This framework can be extended to unfolding of variables associated with the Z-boson. Moreover, particle-level unfolding can be performed to gain more understanding.

- A robust comparison can be done between results obtained from iterative Bayesian, bin-by-bin and profile likelihood unfolding methods.

- As far as the regularisation is concerned, an appropriate technique can be implemented to select values of τ. In addition to that, the bias added due to different τ values can also be measured by setting up a stress test.

- All the systematic uncertainties can be included in the framework.

Bibliography

[1] ATLAS Collaboration, *Observation of the associated production of a top quark and a Z boson in pp collisions at $\sqrt{s}$ = 13 TeV with the ATLAS detector*, (2020), arXiv: 2002.07546 [hep-ex] (cit. on pp. 1, 13, 36–39, 64).

[2] *Standard Model of Particle Physics*, Accessed on: 06.09.2020, URL: https://en.wikipedia.org/wiki/Standard_Model (cit. on p. 4).

[3] P. Z. et al. Particle Data Group, *Review of Particle Physics*, J. Phys. G **37** (2020) 075021, URL: http://pdg.lbl.gov (cit. on pp. 5, 10).

[4] I. Brock and T.Schorner-Sadenius, *Physics at the Terascale*, 1st ed., Wiley-VCH, 2011 (cit. on p. 7).

[5] R.Placakyte, *Parton Distribution Functions*, 2011, arXiv: 1111.5452 (cit. on p. 7).

[6] Z. Marshall and the ATLAS Collaboration, *Simulation of Pile-up in the ATLAS Experiment*, J. Phys.: Conf. Ser 513 022024 (2014) (cit. on p. 10).

[7] S. Dawson, *Introduction to electroweak symmetry breaking*, (1999), arXiv: hep-ph/9901280 (cit. on p. 10).

[8] ATLAS Collaboration, *Measurement of the $t\bar{t}$ production cross-section in the lepton+jets channel at $\sqrt{s}$ = 13 TeV with the ATLAS experiment*, (2020), arXiv: 2006.13076 [hep-ex] (cit. on p. 11).

[9] ATLAS Collaboration, *Measurement of the inclusive cross-sections of single top-quark and top-antiquark t-channel production in pp collisions at $\sqrt{s}$ = 13 TeV with the ATLAS detector*, JHEP **04** (2017) 086, arXiv: 1609.03920 [hep-ex] (cit. on p. 11).

[10] ATLAS Collaboration, *Measurement of the cross-section for producing a W boson in association with a single top quark in pp collisions at $\sqrt{s}$ = 13 TeV with ATLAS*, JHEP **01** (2018) 063, arXiv: 1612.07231 [hep-ex] (cit. on p. 11).

[11] ATLAS Collaboration, *Evidence for single top-quark production in the s-channel in proton–proton collisions at $\sqrt{s}$ = 8 TeV with the ATLAS detector using the Matrix Element Method*, Phys. Lett. B **756** (2016) 228, arXiv: 1511.05980 [hep-ex] (cit. on p. 11).

[12] ATLAS Collaboration, *Measurement of the $t\bar{t}Z$ and $t\bar{t}W$ cross sections in proton–proton collisions at $\sqrt{s}$ = 13 TeV with the ATLAS detector*, Phys. Rev. D **99** (2019) 072009, arXiv: 1901.03584 [hep-ex] (cit. on p. 12).

[13]   ATLAS Collaboration,
       Analysis of tt̄H and tt̄W production in multilepton final states with the ATLAS detector,
       ATLAS-CONF-2019-045, 2019, URL: https://cds.cern.ch/record/2693930
       (cit. on p. 12).

[14]   ATLAS Collaboration, *Evidence for tt̄tt̄ production in the multilepton final state in
       proton-proton collisions at $\sqrt{s} = 13\,TeV$ with the ATLAS detector*, (2020),
       arXiv: 2007.14858 [hep-ex] (cit. on p. 12).

[15]   ATLAS Collaboration, *Measurement of the production cross-section of a single top quark in
       association with a Z boson in proton–proton collisions at* 13 *TeV with the ATLAS detector*,
       Phys. Lett. B **780** (2018) 557, arXiv: 1710.03659 [hep-ex] (cit. on p. 13).

[16]   CMS Collaboration, *Observation of single top quark production in association with a Z boson
       in pp collisions at $\sqrt{s} = 13$ TeV*, (2019), arXiv: 1812.05900 [hep-ex] (cit. on p. 13).

[17]   ATLAS Collaboration, *Top working group cross-section summary plots Spring 2020*,
       ATL-PHYS-PUB-2020-012, Status: May 2020,
       URL: http://cdsweb.cern.ch/record/2718946 (cit. on p. 14).

[18]   URL: https://home.cern/science (cit. on p. 17).

[19]   J. Haffner, *The CERN accelerator complex. Complexe des accélérateurs du CERN*,
       General Photo, 2013, URL: https://cds.cern.ch/record/1621894 (cit. on p. 18).

[20]   L. Evans and P. Bryant, *LHC Machine*, JINST **3** (2008) S08001 (cit. on p. 17).

[21]   J.T.Boyd, *LHC Run-2 and Future Prospects*, (2020), arXiv: 2001.04370 [hep-ex]
       (cit. on p. 18).

[22]   ATLAS Collaboration, *The ATLAS Experiment at the CERN Large Hadron Collider*,
       JINST **3** (2008) S08003 (cit. on p. 19).

[23]   J. Pequenao, *Computer generated image of the whole ATLAS detector*, 2008,
       URL: http://cds.cern.ch/record/1095924 (cit. on p. 19).

[24]   J. Pequenao, *Computer generated image of the ATLAS inner detector*, 2008,
       URL: http://cds.cern.ch/record/1095926 (cit. on p. 20).

[25]   Accessed: 27-09-2020,
       URL: http://atlas.cern/discover/detector/inner-detector (cit. on pp. 20, 21).

[26]   A. Vogel,
       ATLAS Transition Radiation Tracker (TRT): Straw Tube Gaseous Detectors at High Rates,
       CERN, 2013, URL: https://cds.cern.ch/record/1537991 (cit. on p. 21).

[27]   P. Astigarraga and M. Eukeni, *THE ATLAS DATA ACQUISITION SYSTEM IN LHC RUN 2*,
       ATL-DAQ-PROC-2017-043, CERN, 2017, URL: https://cds.cern.ch/record/2292434
       (cit. on p. 23).

[28]   J. Pequenao and P. Schaffner,
       "How ATLAS detects particles: diagram of particle paths in the detector", 2013,
       URL: https://cds.cern.ch/record/1505342 (cit. on p. 23).

[29] ATLAS Collaboration, *Performance of the ATLAS Inner Detector Track and Vertex Reconstruction in High Pile-Up LHC Environment*, ATLAS-CONF-2012-042, 2012, URL: https://cds.cern.ch/record/1435196 (cit. on p. 23).

[30] ATLAS Collaboration, *Performance of the ATLAS track reconstruction algorithms in dense environments in LHC Run 2*, Eur. Phys. J. C **77** (2017) 673, arXiv: 1704.07983 [hep-ex] (cit. on p. 23).

[31] ATLAS Collaboration, *Electron reconstruction and identification in the ATLAS experiment using the 2015 and 2016 LHC proton–proton collision data at $\sqrt{s}$ = 13 TeV*, Eur. Phys. J. C **79** (2019) 639, arXiv: 1902.04655 [hep-ex] (cit. on p. 24).

[32] ATLAS Collaboration, *Muon reconstruction performance of the ATLAS detector in proton–proton collision data at $\sqrt{s}$ = 13 TeV*, Eur. Phys. J. C **76** (2016) 292, arXiv: 1603.05598 [hep-ex] (cit. on p. 24).

[33] M. Cacciari, G. P. Salam and G. Soyez, *The anti-ktjet clustering algorithm*, Journal of High Energy Physics **2008** (2008), ISSN: 1029-8479, URL: http://dx.doi.org/10.1088/1126-6708/2008/04/063 (cit. on p. 25).

[34] ATLAS Collaboration, *Performance of b-jet identification in the ATLAS experiment*, JINST **11** (2016) P04008, arXiv: 1512.01094 [hep-ex] (cit. on p. 25).

[35] Irina Antonela Cioară, *Associated Production of a Top Quark and a Z Boson in pp Collisions at s = 13 TeV Using the ATLAS Detector*, Rheinische Friedrich-Wilhelms-Universität Bonn, 2018, URL: http://hdl.handle.net/20.500.11811/7636 (cit. on pp. 28, 33, 36).

[36] Accessed: 30-10-2020, URL: https://twiki.cern.ch/twiki/bin/viewauth/AtlasProtected/AnalysisTop (cit. on p. 31).

[37] ATLAS Collaboration, *ATLAS data quality operations and performance for 2015–2018 data-taking*, JINST **15** (2020) P04003, arXiv: 1911.04632 [physics.ins-det] (cit. on p. 31).

[38] The ATLAS Collaboration, *Luminosity plots for Run2 operations*, URL: https://twiki.cern.ch/twiki/bin/view/AtlasPublic/LuminosityPublicResultsRun2#Multiple_Year_Collision_Plots (cit. on p. 32).

[39] J. Alwall et al., *The automated computation of tree-level and next-to-leading order differential cross sections, and their matching to parton shower simulations*, Journal of High Energy Physics **2014** (2014), ISSN: 1029-8479, URL: http://dx.doi.org/10.1007/JHEP07(2014)079 (cit. on p. 32).

[40] R. D. Ball et al., *Parton distributions for the LHC run II*, Journal of High Energy Physics **2015** (2015), ISSN: 1029-8479, URL: http://dx.doi.org/10.1007/JHEP04(2015)040 (cit. on p. 32).

[41] S. Alioli et al., *A general framework for implementing NLO calculations in shower Monte Carlo programs: the POWHEG BOX*, Journal of High Energy Physics **2010** (2010), ISSN: 1029-8479, URL: http://dx.doi.org/10.1007/JHEP06(2010)043 (cit. on p. 32).

[42] T. Gleisberg et al., *Event generation with SHERPA 1.1*,
Journal of High Energy Physics **2009** (2009) 007,
URL: https://doi.org/10.1088%2F1126-6708%2F2009%2F02%2F007 (cit. on p. 32).

[43] ATLAS Collaboration,
Validation of Monte Carlo event generators in the ATLAS Collaboration for LHC Run 2,
ATL-PHYS-PUB-2016-001, URL: https://cds.cern.ch/record/2119984 (cit. on p. 32).

[44] *SgTopRun2NtuplesContents*, Accessed: 16-10-2020, URL: https://twiki.cern.ch/twiki/bin/viewauth/AtlasProtected/SgTopRun2NtuplesContents (cit. on p. 33).

[45] M. Blaut, *Non-prompt Lepton Background Estimation for Associated Production of a Top Quark and a Z boson in pp Collisions at $\sqrt{s}$ = 13 TeV at ATLAS*,
Rheinische Friedrich-Wilhelms-Universität Bonn, 2018 (cit. on p. 35).

[46] ATLAS Collaboration, *Luminosity determination in pp collisions at $\sqrt{s}$ = 13 TeV using the ATLAS detector at the LHC*, ATLAS-CONF-2019-021, 2019,
URL: https://cds.cern.ch/record/2677054 (cit. on p. 36).

[47] *Artificial Neural Network*, Accessed on: 18.10.2020,
URL: https://en.wikipedia.org/wiki/Artificial_neural_network (cit. on p. 37).

[48] M. Feindt and U. Kerzel, *The NeuroBayes neural network package*,
Nuclear Instruments and Methods in Physics Research Section A: Accelerators, Spectrometers, Detectors and Associated Equipment **559** (2006) 190, ISSN: 0168-9002,
URL: http://www.sciencedirect.com/science/article/pii/S0168900205022679
(cit. on p. 37).

[49] F. James and M. Roos, *Minuit - a system for function minimization and analysis of the parameter errors and correlations*, Computer Physics Communications **10** (1975) 343,
ISSN: 0010-4655,
URL: http://www.sciencedirect.com/science/article/pii/0010465575900399
(cit. on p. 39).

[50] *Documentation for TRExFitter*, Accessed: 20-10-2020,
URL: https://trexfitter-docs.web.cern.ch/trexfitter-docs/ (cit. on p. 39).

[51] TRExFitter tutorial, URL: https://indico.cern.ch/event/918238/contributions/3859402/attachments/2049381/3437677/TRExFitterTutorial2020.pdf
(cit. on p. 39).

[52] K. Cranmer et al.,
HistFactory: A tool for creating statistical models for use with RooFit and RooStats,
CERN-OPEN-2012-016, New York U., 2012,
URL: https://cds.cern.ch/record/1456844 (cit. on p. 39).

[53] Accessed: 25-10-2020, URL: https://amva4newphysics.wordpress.com/2016/01/29/shape-constrained-unfolding/
(cit. on p. 42).

[54] G. Cowan, *A survey of unfolding methods for particle physics*, Oxford University Press, 1998
(cit. on pp. 42–44, 46).

[55] S. Biondi, *Experience with using unfolding procedures in ATLAS*,
      URL: http://pi.physik.uni-bonn.de/pi_only/thesis.php (cit. on p. 43).

[56] J. Howarth, Talk at the Top Working Group Workshop 2019, URL:
      https://indico.cern.ch/event/795477/contributions/3378783/attachments/
      1848586/3033879/JayHowarth_ATLAS_TopWorkshop_UnfoldingTutorial.pdf
      (cit. on pp. 43, 45, 57).

[57] Spanò, Francesco, *Unfolding in particle physics: a window on solving inverse problems*,
      EPJ Web of Conferences **55** (2013) 03002,
      URL: https://doi.org/10.1051/epjconf/20135503002 (cit. on pp. 43, 46).

[58] *Unfolding using profile likelihood*, Accessed: 30-10-2020, URL: https://trexfitter-
      docs.web.cern.ch/trexfitter-docs/AdvancedTutorial2020/Unfolding/
      (cit. on p. 45).

[59] Accessed: 30-10-2020,
      URL: https://indico.cern.ch/event/890060/contributions/3754199/
      attachments/1991168/3320058/Unfolding_with_TRExFitter.pdf (cit. on p. 45).

[60] W. Buttinger, URL: https://indico.cern.ch/event/670305/contributions/
      2742204/attachments/1535980/2406195/troofitUnfolding.pdf (cit. on p. 46).

[61] D. Calvetti et al., *Tikhonov regularization and the L-curve for large discrete ill-posed problems*,
      Journal of Computational and Applied Mathematics **123** (2000), ISSN: 0377-0427,
      URL: http://www.sciencedirect.com/science/article/pii/S0377042700004143
      (cit. on p. 46).

[62] G. D'Agostini, *A multidimensional unfolding method based on Bayes' theorem*,
      Nuclear Instruments and Methods in Physics Research Section A: Accelerators, Spectrometers,
      Detectors and Associated Equipment **362** (1995) 487, ISSN: 0168-9002,
      URL: http://www.sciencedirect.com/science/article/pii/016890029500274X
      (cit. on p. 47).

[63] *RooUnfold*, URL: https://gitlab.cern.ch/RooUnfold/RooUnfold (cit. on p. 48).

[64] F.James, *MINUIT: Function Minimization and Error Analysis*,
      URL: https://cds.cern.ch/record/2296388/files/minuit.pdf (cit. on p. 48).

[65] A. Armbruster, K. Kröninger, B. Malaescu, F. Spano, *Practical considerations for unfolding*,
      ATL-COM-PHYS-2014-277, 2014 (cit. on p. 49).

[66] C. Boever, *Differential cross-section measurement of the tZq process with the ATLAS detector*,
      Universität Bonn, 2019 (cit. on pp. 51, 52, 64, 67, 73).

[67] Rui Zhang, *Inclusive and differential cross-section measurements of tW single top-quark
      production at s = 13 TeV with the ATLAS detector*,
      PhD thesis: Rheinische Friedrich-Wilhelms-Universität Bonn, 2019,
      URL: http://hdl.handle.net/20.500.11811/7942 (cit. on p. 52).

[68] R. Frigg and I. Votsis,
      Everything You Always Wanted to Know About Structural Realism But Were Afraid to Ask,
      European Journal for Philosophy of Science **1** (2011) 227 (cit. on p. 57).

[69]   *Nuisance parameter ranking*, Accessed: 30-10-2020, URL: `https://trexfitter-docs.web.cern.ch/trexfitter-docs/BasicTutorial2020/Ranking/` (cit. on p. 67).

[70]   M. Alhroob et al.,
       Observation of the associated production of a top quark and a Z boson at 13 TeV with ATLAS,
       tech. rep., 2018, URL: `https://cds.cern.ch/record/2304824` (cit. on p. 81).

List of Monte Carlo samples

An overview of the nominal Monte Carlo samples used in this thesis are provided. A detailed description can be found in [70].

Table A.1: Overview of nominal signal and background MC samples corresponding to version 28 ntuples

Process	Sample ID	Generator	σ[pb]	k-factor	N-generated
tZq	412063	MadGraphPy8Ev-A14-tllq-NLO	0.0300	1.00	mc16a: 4.99 M
					mc16d: 6.23 M
					mc16d: 6.23 M
					mc16e: 8.26 M
$t\bar{t}$	410472	PowPy8Ev–A14–ttbar–hdamp258p75–dil	77.0	1.14	mc16a: 79.83 M
					mc16d: 44.88 M *
					mc16e: 99.25 M
tW	410648	PowPy8Ev–A14–Wt–t–dil	4.00	0.94	mc16a: 1.00 M
					mc16d: 1.25 M
					mc16e: 1.66 M
	410649	PowPy8Ev–A14–Wt–tbar–dil	3.99	0.94	mc16a: 1.00 M
					mc16d: 1.25 M
					mc16e: 1.65 M
$t\bar{t}H$	346343	PowPy8Ev–A14–ttH125–allhad	0.0534	1.00	mc16a: 4.98 M
					mc16d: 6.49 M
					mc16e: 8.25 M
	346344	PowPy8Ev–A14–ttH125–sl	0.223	1.00	mc16a: 4.99 M
					mc16d: 6.50 M
					mc16e: 8.26 M
	346345	PowPy8Ev–A14–ttH125–dilep	0.231	1.00	mc16a: 4.99 M
					mc16d: 6.49 M
					mc16e: 8.28 M
	410155	aMcAtNloPy8Ev–A14–ttW	0.548	1.10	mc16a: 7.50 M
					mc16d: 7.50 M
					mc16e: 12.04 M

Continued on next page

Table A.1 – *Continued from previous page*

Process	Sample ID	Generator	σ[pb]	k-factor	N-generated
	410156	aMcAtNloPy8Ev–A14–ttZnunu	0.155	1.11	mc16a: 1.50 M
					mc16d: 1.50 M
					mc16e: 2.00 M
	410157	aMcAtNloPy8Ev–A14–ttZqq	0.528	1.11	mc16a: 3.00 M
					mc16d: 3.00 M
					mc16e: 3.59 M
	410218	aMcAtNloPy8Ev–A14–ttee	0.0369	1.12	mc16a: 1.41 M
					mc16d: 1.34 M
					mc16e: 2.17 M
	410219	aMcAtNloPy8Ev–A14–ttmumu	0.0369	1.12	mc16a: 1.41 M
					mc16d: 1.34 M
					mc16e: 2.17 M
	410220	aMcAtNloPy8Ev–A14–tttautau	0.0365	1.12	mc16a: 0.94 M
					mc16d: 0.90 M
					mc16e: 0.96 M
tWZ	410408	aMcAtNloPy8Ev–A14–tWZ–Ztoll–DR1	0.0200	1.00	mc16a: 0.10 M
					mc16d: 0.12 M
					mc16e: 0.16 M
Diboson	363356	Sherpa221–ZqqZll	15.6	0.14	mc16a: 5.40 M
					mc16d: 5.40 M
					mc16e: 8.95 M
	363358	Sherpa221–WqqZll	3.44	1.00	mc16a: 5.40 M
					mc16d: 26.91 M
					mc16e: 8.96 M
	364250	Sherpa222–llll	1.25	1.00	mc16a: 17.84 M
					mc16d: 36.00 M
					mc16e: 25.68 M
	364253	Sherpa222–lllv	4.58	1.00	mc16a: 15.54 M
					mc16d: 32.11 M
					mc16e: 26.79 M
	364254	Sherpa222–llvv	12.5	1.00	mc16a: 15.00 M
					mc16d: 29.98 M
					mc16e: 24.89 M
$Z + jets$	364114	Sherpa221–Zee–maxHtPtV0_70–L	1 630	0.98	mc16a: 8.00 M
					mc16d: 10.00 M
					mc16e: 13.27 M
	364115	Sherpa221–Zee–maxHtPtV0_70–C	224	0.98	mc16a: 5.00 M
					mc16d: 6.24 M
					mc16e: 8.31 M
	364116	Sherpa221–Zee–maxHtPtV0_70–B	126	0.98	mc16a: 8.00 M
					mc16d: 9.99 M
					mc16e: 13.28 M

Process	Sample ID	Generator	σ[pb]	*k*-factor	*N*-generated
	364117	Sherpa221–Zee–maxHtPtV70_140–L	76.3	0.98	mc16a: 5.96 M
					mc16d: 7.38 M
					mc16e: 9.95 M
	364118	Sherpa221–Zee–maxHtPtV70_140–C	20.3	0.98	mc16a: 2.00 M
					mc16d: 2.50 M
					mc16e: 3.33 M
	364119	Sherpa221–Zee–maxHtPtV70_140–B	12.6	0.98	mc16a: 5.97 M
					mc16d: 7.49 M
					mc16e: 9.91 M
	364120	Sherpa221–Zee–maxHtPtV140_280–L	25.0	0.98	mc16a: 5.00 M
					mc16d: 6.25 M
					mc16e: 8.36 M
	364121	Sherpa221–Zee–maxHtPtV140_280–C	9.37	0.98	mc16a: 3.00 M
					mc16d: 3.75 M
					mc16e: 4.99 M
	364122	Sherpa221–Zee–maxHtPtV140_280–B	6.08	0.98	mc16a: 12.44 M
					mc16d: 15.66 M
					mc16e: 20.74 M
	364123	Sherpa221–Zee–maxHtPtV280_500–L	4.87	0.98	mc16a: 2.00 M
					mc16d: 2.50 M
					mc16e: 2.78 M
	364124	Sherpa221–Zee–maxHtPtV280_500–C	2.28	0.98	mc16a: 1.00 M
					mc16d: 1.25 M
					mc16e: 1.74 M
	364125	Sherpa221–Zee–maxHtPtV280_500–B	1.49	0.98	mc16a: 2.00 M
					mc16d: 2.50 M
					mc16e: 3.33 M
	364126	Sherpa221–Zee–maxHtPtV500_1000	1.81	0.98	mc16a: 3.00 M
					mc16d: 3.71 M
					mc16e: 4.98 M
	364127	Sherpa221–Zee–maxHtPtV1000_Ecms	0.150	0.98	mc16a: 1.00 M
					mc16d: 1.25 M
					mc16e: 1.67 M
	364100	Sherpa221–Zmumu–maxHtPtV0_70–L	1 630	0.98	mc16a: 7.97 M
					mc16d: 9.91 M
					mc16e: 13.26 M
	364101	Sherpa221–Zmumu–maxHtPtV0_70–C	224	0.98	mc16a: 4.98 M
					mc16d: 6.20 M
					mc16e: 8.28 M
	364102	Sherpa221–Zmumu–maxHtPtV0_70–B	127	0.98	mc16a: 7.98 M
					mc16d: 9.26 M
					mc16e: 13.24 M

Table A.1 – *Continued from previous page*

Process	Sample ID	Generator	σ[pb]	k-factor	N-generated
	364103	Sherpa221–Zmumu–maxHtPtV70_140–L	75.0	0.98	mc16a: 5.98 M mc16d:7.48 M mc16e: 9.94 M
	364104	Sherpa221–Zmumu–maxHtPtV70_140–C	20.4	0.98	mc16a: 2.00 M mc16d:2.49 M mc16e: 3.31 M
	364105	Sherpa221–Zmumu–maxHtPtV70_140–B	12.4	0.98	mc16a: 5.98 M mc16d:7.47 M mc16e: 9.94 M
	364106	Sherpa221–Zmumu–maxHtPtV140_280–L	24.3	0.98	mc16a: 5.00 M mc16d:6.24 M mc16e: 8.29M
	364107	Sherpa221–Zmumu–maxHtPtV140_280–C	9.28	0.98	mc16a: 3.00 M mc16d:3.75 M mc16e: 4.99 M
	364108	Sherpa221–Zmumu–maxHtPtV140_280–B	6.01	0.98	mc16a: 12.46 M mc16d:15.63 M mc16e: 20.74 M
	364109	Sherpa221–Zmumu–maxHtPtV280_500–L	4.77	0.98	mc16a: 2.00 M mc16d: 2.46M mc16e: 3.32M
	364110	Sherpa221–Zmumu–maxHtPtV280_500–C	2.27	0.98	mc16a: 1.00 M mc16d: 1.25M mc16e: 1.67M
	364111	Sherpa221–Zmumu–maxHtPtV280_500–B	1.49	0.98	mc16a: 2.00 M mc16d: 2.50M mc16e: 3.33M
	364112	Sherpa221–Zmumu–maxHtPtV500_1000	1.79	0.98	mc16a: 3.00 M mc16d: 3.75M mc16e: 5.09M
	364113	Sherpa221–Zmumu–maxHtPtV1000_Ecms	0.150	0.98	mc16a: 1.00 M mc16d: 1.25M mc16e: 1.67M
	364128	Sherpa221–Ztautau–maxHtPtV0_70–L	1 630	0.98	mc16a: 7.99 M mc16d: 10.00M mc16e: 13.27M
	364129	Sherpa221–Ztautau–maxHtPtV0_70–C	224	0.98	mc16a: 4.98 M mc16d: 6.14M mc16e: 8.27M
	364130	Sherpa221–Ztautau–maxHtPtV0_70–B	128	0.98	mc16a: 8.00 M mc16d: 9.99M mc16e:13.28M

Continued on next page

Process	Sample ID	Generator	σ[pb]	k-factor	N-generated
	364131	Sherpa221–Ztautau–maxHtPtV70_140–L	76.0	0.98	mc16a: 6.00 M
					mc16d: 7.50M
					mc16e:9.97M
	364132	Sherpa221–Ztautau–maxHtPtV70_140–C	20.2	0.98	mc16a: 2.00 M
					mc16d: 2.50M
					mc16e:3.33M
	364133	Sherpa221–Ztautau–maxHtPtV70_140–B	12.3	0.98	mc16a: 5.97 M
					mc16d: 7.50M
					mc16e: 9.96M
	364134	Sherpa221–Ztautau–maxHtPtV140_280–L	24.8	0.98	mc16a: 4.94 M
					mc16d: 6.23M
					mc16e: 8.30M
	364135	Sherpa221–Ztautau–maxHtPtV140_280–C	9.33	0.98	mc16a: 3.00 M
					mc16d: 3.75M
					mc16e: 4.99M
	364137	Sherpa221–Ztautau–maxHtPtV280_500–L	4.79	0.98	mc16a: 2.00 M
					mc16d: 2.50M
					mc16e: 3.32M
	364138	Sherpa221–Ztautau–maxHtPtV280_500–C	2.28	0.98	mc16a: 1.00 M
					mc16d: 1.23M
					mc16e: 1.67M
	364139	Sherpa221–Ztautau–maxHtPtV280_500–B	1.50	0.98	mc16a: 1.98 M
					mc16d: 2.50M
					mc16e: 3.32M
	364140	Sherpa221–Ztautau–maxHtPtV500_1000	1.81	0.98	mc16a: 3.00 M
					mc16d: 3.75M
					mc16e: 4.96M
	364141	Sherpa221–Ztautau–maxHtPtV1000_Ecms	0.150	0.98	mc16a: 1.00 M
					mc16d: 1.25M
					mc16e: 1.67M

Validation tests on regularised MC sample

Regularisation with $\tau = 1$ and $\tau = 1.5$ is applied on MC sample of $p_T(W)$. The validation tests are presented.

B.1 Unfolded distributions

The unfolded distributions are shown in Figure B.1 and the signal strength values obtained in both cases of τ are given in Table B.1 and Table B.2. Moreover, regularised normalisation factors for the same are shown in Figure B.2 and Figure B.3.

Bins	μ
1	0.99 ± 0.46
2	0.99 ± 0.44
3	1.00 ± 0.52
4	0.99 ± 0.52

Table B.1: POI values ($\tau = 1$)

Bins	μ
1	0.99 ± 0.40
2	1.00 ± 0.37
3	1.00 ± 0.44
4	0.99 ± 0.44

Table B.2: POI values ($\tau = 1.5$)

B.2 Pseudo-experiments

Pseudo-experiments were performed on the regularised MC sample. It is seen that the standard deviation in all bins deviates from one. This is because of the bias in measurement caused by regularisation.
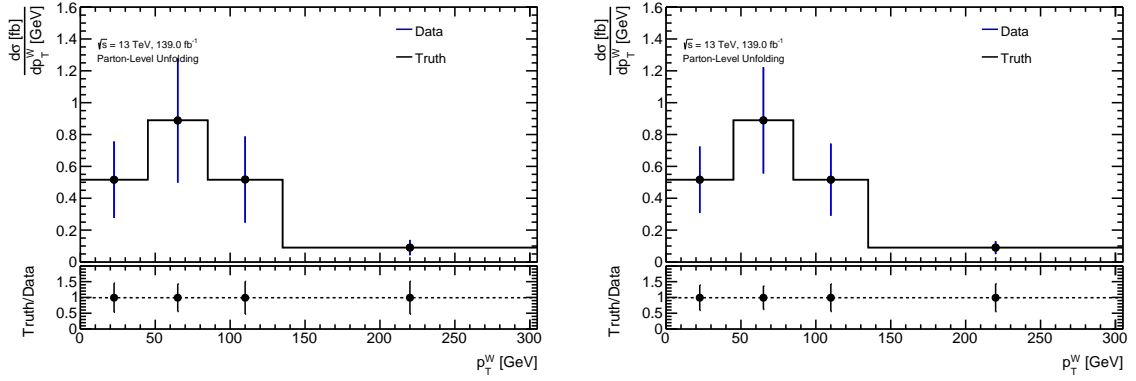
(a) Regularised unfolded MC ($\tau = 1$)   (b) Regularised unfolded MC ($\tau = 1.5$)

Figure B.1: Regularised unfolded distributions for $p_T(W)$
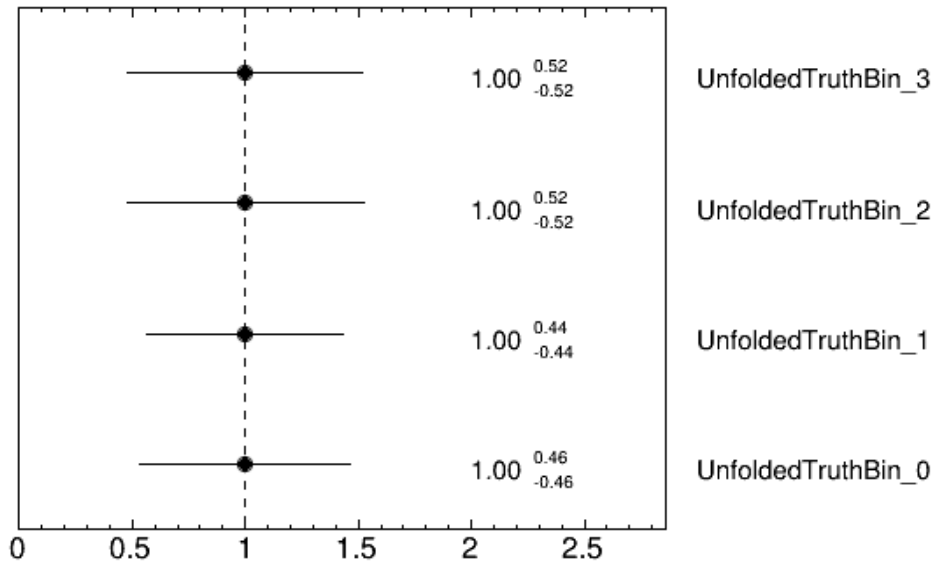
Figure B.2: Normalisation factors in case of ($\tau = 1$)
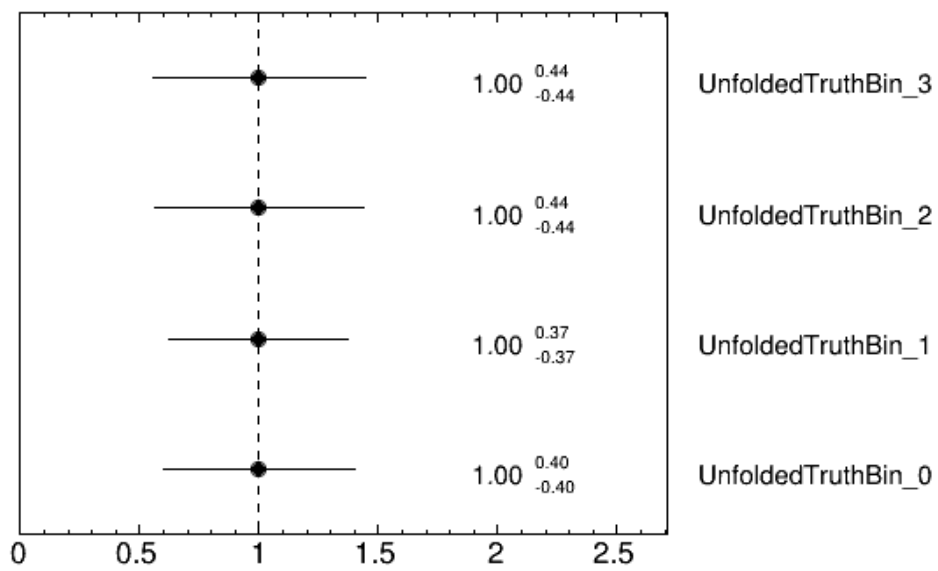
Figure B.3: Normalisation factors in case of $\tau = 1.5$

(a) Toy distribution for bin 1

(b) Toy distribution for bin 2

(c) Toy distribution for bin 3

(d) Toy distribution for bin 4
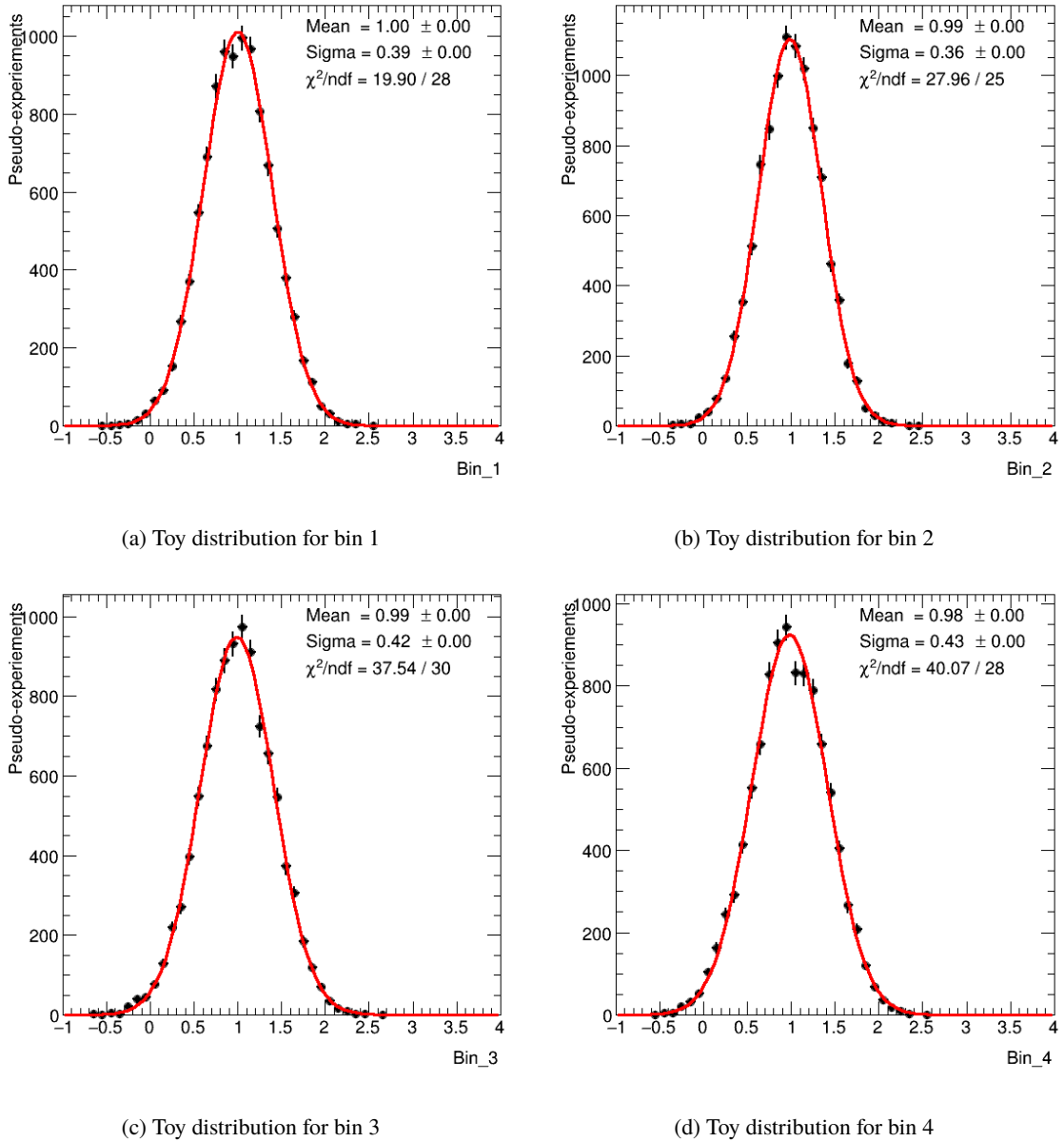
Figure B.4: Toy distributions of all bins in case of $\tau = 1$
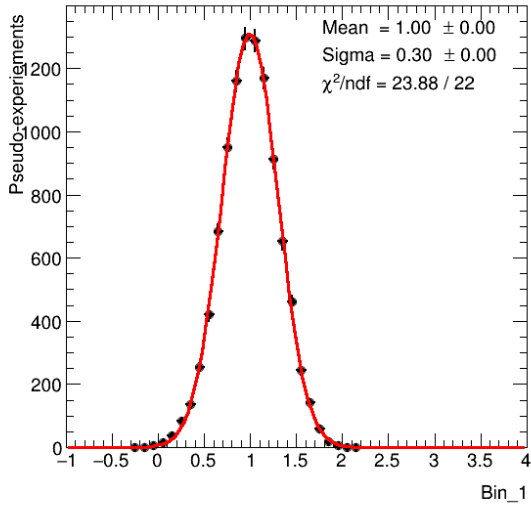
(a) Toy distribution for bin 1
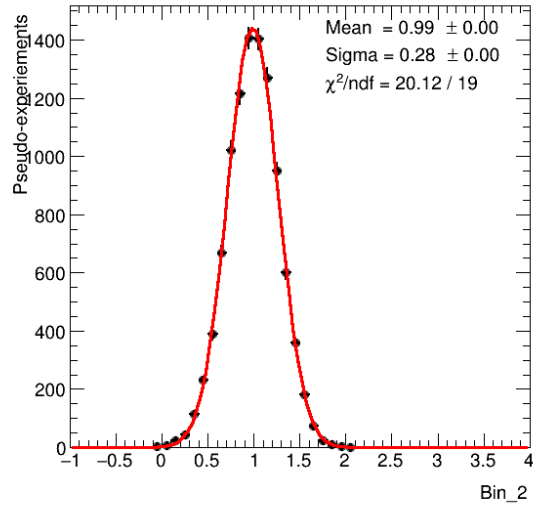
(b) Toy distribution for bin 2
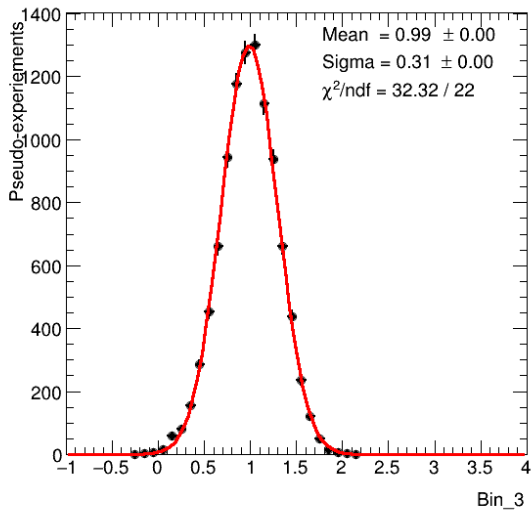
(c) Toy distribution for bin 3
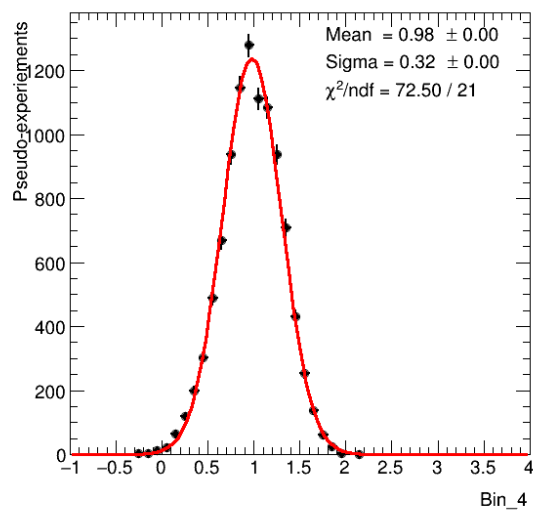
(d) Toy distribution for bin 4

Figure B.5: Toy distributions of all bins in case of $\tau = 1.5$
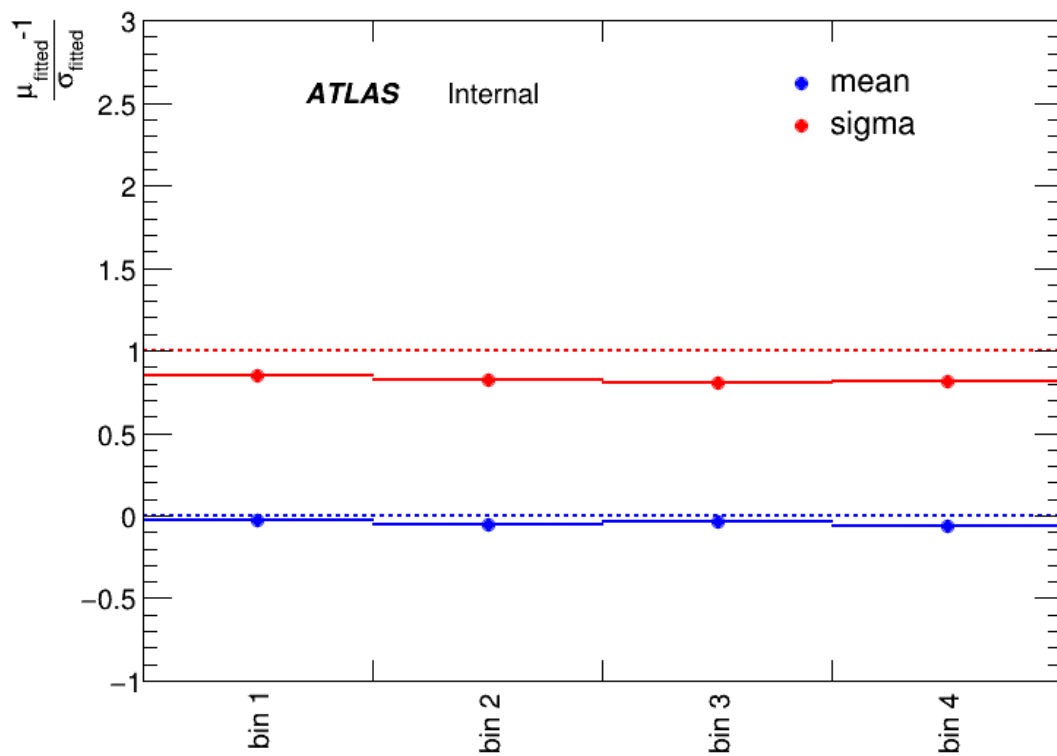
Figure B.6: Mean and standard deviation of distribution of pulls for every bin in case of $\tau = 1$
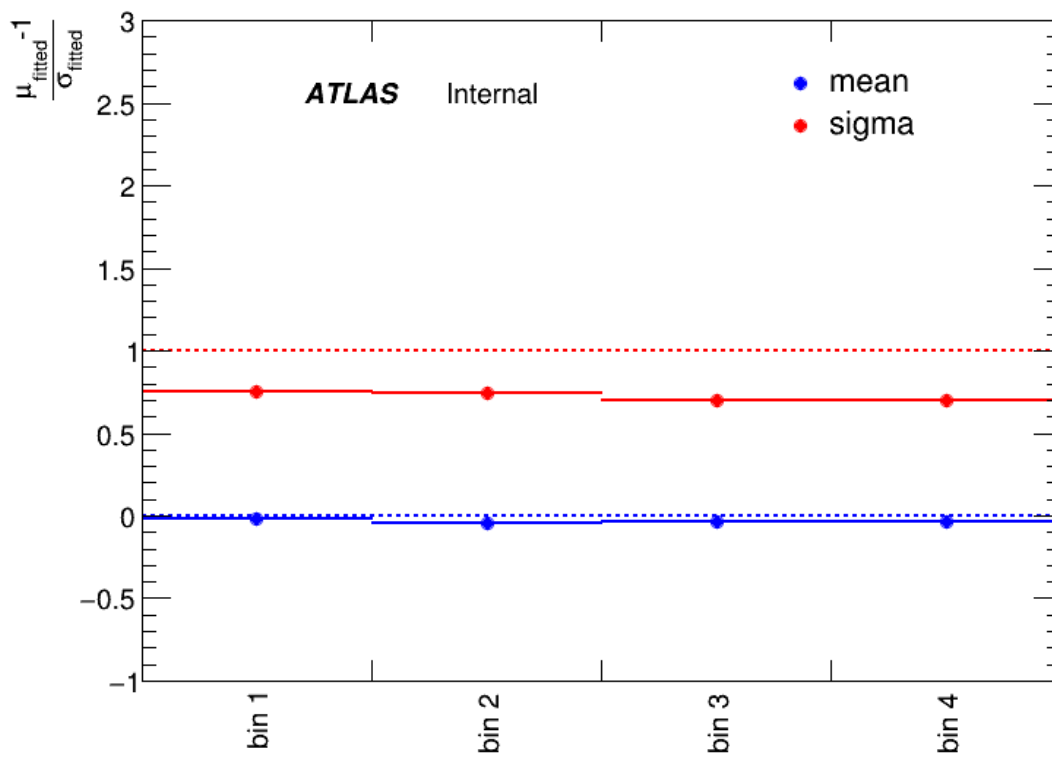
Figure B.7: Mean and standard deviation of distribution of pulls for every bin in case of $\tau = 1.5$

List of Figures

List of Tables

Acknowledgements

I came to Bonn with a dream of exploring particle physics. I am grateful to Prof. Dr. Ian C. Brock who introduced me to the research world of high energy physics. His invaluable guidance helped me take my baby steps into research through this master thesis. I would like to extend my gratitude to Priv. -Doz. Dr. Philip Bechtle for being the second supervisor for my thesis.

I would like to thank Chris Boever for giving a head start to my thesis and regularly checking up on the progress. He solved each and every query I had, not only while he was in Bonn but also when he left Bonn. I am extremely thankful to Anjishnu Bandyopadhyay for all the statistics and `TRExFitter` discussions we had. He was my go-to person for solving any kind of problem. I would like to thank Tanja Holm for supervising me while I was working with `SingleTopAnalysis` package. Thank you Oleh Kivernyk for proofreading my thesis. The next person I am thankful to is, Federico G. Diaz Capriles for correcting my thesis and educating me with salient features of the English language! Thank you Christian Kirfel for arranging coffee-breaks along with interesting discussions and fun board game evenings. I would like to express my gratitude to all the Brock group members including Maxx, Han Na, Richard, Ellinor, Piet and Nicolas for creating a friendly environment at work. My *unfolding* endeavour would be incomplete without the support of the `TRExFitter` community, especially Tomas Dado, Michele Pinamonti and Francesco Spanò, for their dedicated work to develop the framework. Their prompt responses helped me understand the concepts of profile likelihood unfolding much better.

There are many people I would like to thank, who have been an inseparable part of my life. Thank you Ziad for always being there, helping me settle in this new country. He is always just a phone call away when I need a friend so talk to. Thank you Tilak for constantly checking on me while I was writing my thesis and for helping me improve my presentation skills. A special thank you to my sister, Krishna, for always being encouraging, supporting and understanding. I am extremely thankful to my boyfriend Divyanshu, for supporting me emotionally and lifting up my spirits whenever I felt low. Thank you for teaching me how to embrace my failures and learn from them.

Last but certainly not the least, I am grateful to my parents who love me unconditionally and believe in me. I am blessed to have such parents who have constantly supported me in my efforts and have always motivated me to achieve my dreams. I wouldn't have accomplished this, if they weren't there with me at every step. They are indeed the *wind beneath my wings*!